UNIVERSITY OF OKLAHOMA

GRADUATE COLLEGE

A FREE-SPACE OPTICAL COMMUNICATIONS LINK TO AN UNMANNED
AERIAL VEHICLE

A Dissertation

SUBMITTED TO THE GRADUATE FACULTY

In partial fulfillment of requirements for the

Degree of

Doctor of Philosophy

By

ALAN HARRIS
Norman, OK
2005

UMI Number: 3203290

UMI®

**A FREE-SPACE OPTICAL COMMUNICATIONS LINK TO AN UNMANNED
AERIAL VEHICLE**

**A Dissertation APPROVED FOR THE
SCHOOL OF ELECTRICAL AND COMPUTER ENGINEERING**

BY

_____
Dr. James J. Sluss, Jr.

_____
Dr. William O. Ray.

_____
Dr. Hazem H. Refai

_____
Dr. Monte P. Tull

_____
Dr. Pramode K. Verma

Acknowledgements

I would like to thank everyone who has helped me and encouraged me while working on my doctoral work. I am extremely grateful for all the help and guidance provided to me by my committee: Dr. Sluss, Dr. Ray, Dr. Refai, Dr. Tull and Dr. Verma. I would like to give special thanks to Dr. Sluss for all the advice and guidance he has given me throughout my graduate studies. I have learned a great deal from him, and without his support I would not have been able to complete my graduate studies.

Finally, I would like to thank my parents Roy and Beth for their support throughout my studies, without their help, none of this would have been possible.

Table of Contents

List of Illustrations

List of Tables

Alan Harris' Publications

Journal Papers:

Alan Harris, James J. Sluss Jr., Hazem H. Refai and Peter G. Lopresti, "Free-Space Optical Wavelength Diversity Scheme for Fog Mitigation in a Ground-to-UAV Communications Link", under review for SPIE Optical Engineering

Conference Papers with Proceedings:

Alan Harris, James J. Sluss, Jr., Hazem H. Refai and Peter G. LoPresti, "Atmospheric turbulence effects on a wavelength diversified ground-to-UAV FSO link," Accepted for Publication at SPIE Photonics West, San Jose, CA, January 2006.

Alan Harris, James J. Sluss, Jr., Hazem H. Refai and Peter G. LoPresti, "Alignment and Tracking of a Free-Space Optical Communication Link to a UAV," Accepted for presentation at IEEE 24th Digital Avionics Systems Conference, Washington, DC, October 2005.

Alan Harris, James J. Sluss Jr., Hazem H. Refai and Peter G. LoPresti, "Analysis of beam steering tolerances and divergence for various long range FSO communication

links," SPIE Defense and Security Symposium, Orlando, FL, March 2005, Vol. 5819, pp. 455-463.

Alan Harris, James J. Sluss Jr., Hazem H. Refai and Peter G. LoPresti, "Comparison of active beam steering elements and analysis of platform vibrations for various long-range FSO links," SPIE Defense and Security Symposium, Orlando, FL, March 2005, Vol. 5819, pp. 474-485.

Alan Harris and Weldon Wilson, "Nonlinear Models of World Population Growth," Conference on Applied Mathematics, Edmond, OK, May 1999.

<u>**Conference Papers with an Abstract:**</u>

Alan Harris and James J. Sluss, Jr., "A simple load cell using a fiber Bragg grating," 86th Optical Society of America Annual Meeting, Orlando, FL, October 2002, MK15 p 53.

Abstract

Free-space optics (FSO) is an optical communications technology in which information is transmitted through the atmosphere on modulated optical beams. At the time of the development of FSO, it was envisioned to be a possible solution for provision of connectivity between customer premises and the optical backbone of today's telecommunications infrastructure. Due to limitations in the performance of FSO technology under adverse weather conditions, it is unable to provide sufficiently reliable connectivity for permanent telecommunications and networking applications. This dissertation investigates the deployment of FSO communications links to provide a temporary high-bandwidth communication line between a ground station and an unmanned aerial vehicle (UAV). The deployment of FSO links for ground-to-UAV communications is analyzed from the standpoint of feasibility based on beam steering tolerances and beam divergences, along with platform vibration analysis and active beam steering element comparisons. A mathematical model of a ground-to-UAV communication link is developed. Furthermore, an experimental analysis of a mechanical gimbal's accuracy and repeatability is performed. A wavelength diversity scheme in the presence of atmospheric turbulence is proposed to improve the alignment process. Finally, a wavelength diversity scheme is discussed which allows for transmission through radiation fog.

Chapter 1

Introduction

Free-space optics (FSO) is a communications technology in which information is transmitted through the atmosphere on either modulated laser beams or modulated light emitting diode (LED) beams [1]. FSO technology was originally developed in order to bridge the "last mile" gap between the optical backbone and customer premises that exists in many of today's communications networks. Although FSO equipment was developed in order to provide telecommunications class services, actual installations of FSO equipment have not been able to provide the 99.999% reliability needed for carrier grade services [2]. For this reason, FSO is now being investigated as a possible high-bandwidth solution for the provision of temporary high-speed communications links in a variety of applications.

Unmanned aerial vehicles (UAVs), such as the United States Airforce Predator UAV are currently equipped with both UHF and VHF radio relay links, as well as a C-band line-of-sight data link with a 150 nautical mile range and UHF and Ku-band satellite data links [3]. Based on the increasing need for UAVs to have the in-flight capability to deliver large amounts of data to a military command post in a short amount of time, using FSO technology to establish a temporary high-bandwidth communications link to a UAV is seen as a viable solution to this need. This dissertation investigates the feasibility of using FSO technology to establish a communications link to a UAV.

FSO technology has several advantages for deployment in ground-to-UAV applications:

- FSO technology does not require Federal Communications Commission (FCC) licensing [1].

- FSO equipment has been demonstrated to be a viable transport medium for transmitting existing RF signals in analog format [4].

- Communication links employing FSO technology are highly immune to electromagnetic interference [1].

- FSO transmitters and receivers are highly invulnerable to interference from other optical radiation sources [5,6].

- Once established, FSO links are extremely immune to interference and interception [7].

- Optical transmission of data requires far smaller transmitter and receiver aperture sizes than corresponding millimeter wave technology [8].

- FSO equipment is highly portable – for a ground-to-UAV application FSO ground units can easily be mobilized and deployed.

- Gimbal equipment is currently available with the accuracy to align and track ground-to-UAV FSO links [9].

- Wavelength diversity schemes can be incorporated into FSO communications in order to improve link acquisition and performance in the presence of atmospheric turbulence [10].

- Wavelength diversity schemes can reduce the impact of atmospheric weather conditions on FSO communications links [11,12].

The objectives of the research for this dissertation were as follows:

- Perform a feasibility study in order to accurately ascertain the useful range of FSO deployment. Because this dissertation is the starting point of the development of a ground-to-UAV FSO communications link, the useful range of FSO equipment must first be defined. Characterizations of steering tolerances for link deployment along with geometric divergence calculations are necessary in order to define the useful range of FSO equipment.

- A comparison of active beam steering elements in order to verify the ability of active optical components to offset platform vibrations present at the remote FSO transceiver. Along with this comparison, a simulation of the effects of vibration on beam motion for various length FSO communications links in order to further verify the useful range of FSO technology.

- An experimental classification of a mechanical gimbal's accuracy and repeatability in order to verify that a ground-to-UAV FSO communications link can be aligned and tracked. Along with the gimbal analysis, a simulation

of the effects of atmospheric turbulence on a ground-to-UAV FSO link were performed to determine the beam steering tolerances of the gimbal more accurately.

- A simulation study of the effects of atmospheric turbulence on a wavelength diversified ground-to-UAV FSO communications link. This simulation led to the proposal of a wavelength diversity scheme for improved alignment and tracking and turbulence offset for a ground-to-UAV link.

- A detailed simulation of the effects of different weather conditions on a diversified ground-to-UAV FSO communications link. This section will provide a detailed study of the use of wavelength diversity as a method to offset the effects of weather on a ground-to-UAV link.

This study made use of analytical, simulation and experimental techniques in order to investigate ground-to-UAV FSO communications links. These investigations have led to the following contributions of this dissertation:

- A detailed analysis of the feasibility of FSO communications links for use in various long-range applications [13]. This was the first study reported on the useful range of FSO technology based on divergence of laser beams.

- An analysis of the effects of vibration on an FSO communications link, along with a comparison of active beam steering elements [14].

- An experimental analysis of a gimbal system for use in ground-to-UAV FSO communications links along with an analysis of atmospheric effects on a ground-to-UAV FSO link [9].

- Proposal of a wavelength diversity scheme in the presence of atmospheric turbulence for ground-to-UAV FSO link acquisition [10].

- Proposal of a wavelength diversity scheme for weather mitigation for ground-to-UAV FSO links [12].

The organization of the remaining text of this dissertation is as follows: Chapter 2 reviews the fundamental theory of FSO operation. This chapter includes a detailed analysis of external factors affecting FSO link performance and a discussion of available technology for active beam tracking. Chapter 3 contains an analytical study along with simulation results in order to determine the feasible range of FSO technology, along with a mathematical model of a ground-to-UAV FSO communications link. An experimental classification of a mechanical gimbal along with atmospheric turbulence effects on FSO alignment is presented in Chapter 4. An FSO wavelength diversity scheme in the presence of atmospheric turbulence is presented in Chapter 5. Chapter 6 discusses a wavelength diversity scheme in the presence of different atmospheric weather conditions. The final chapter contains concluding remarks for the information presented in this dissertation, along with suggestions for future research in this field.

Chapter 2

FSO Communications for Ground-to-UAV

Applications

2.1 Introduction

Free-space optics (FSO) is a technology that has undergone a rapid development over the last several years. In the telecommunications industry, there has been a rapid evolution from a copper based network infrastructure to an optical fiber based infrastructure. Optical fiber based networks allow telecommunications vendors to provide reliable high-bandwidth services to their clientele. However, during the development of these optical networks, a gap in the optical network, commonly referred to as the "last mile bottleneck" was created. In this "last mile bottleneck" more traditional copper based networks are still used to provide connectivity between the customer premises and the optical network backbone.

FSO systems were developed as one possible solution in order to bridge this so-called "last-mile bottleneck" problem [1]. FSO was originally seen as an extremely attractive option for this problem because like fiber, it is an optical technology that is able to provide the high bandwidth required on today's networks. A further advantage for the use of FSO systems for the provision of optical connectivity to the

end user is based on the fact that in the United States, an estimated 95 percent of buildings are within 1.5 *km* of a fiber-optic network infrastructure [15]. Installation of a fiber based solution to connect the end-user to the optical network can cost between $100,000 and $200,000 per kilometer in metropolitan areas where as much as 85 percent of the cost is attributed to trenching and installation costs [15].

As FSO technology was first being developed, several different applications were envisioned as possible areas in which to implement FSO systems. These areas included [15]:

- Metro network extensions
- Last-mile access
- Enterprise connectivity
- Fiber backup
- Backhaul
- Service acceleration

Due to the high bandwidth and ease of installation associated with FSO systems, researchers are currently investigating alternate uses for FSO systems. Lasers have already been demonstrated as a viable communications medium for inter-satellite communications [16-24] and are being investigated for use in deep-space communications links [25-29]. The high bandwidth of an FSO communications link

makes it an extremely attractive option for use in systems in which a temporary link needs to be established in order to transmit a large amount of data.

The remainder of this chapter is organized as follows: In Section 2.2, the fundamentals of an FSO communications system will be discussed. This discussion includes an overview of FSO operation, the components of an FSO system and sources of loss in FSO links. Section 2.3 contains a discussion on the optical properties of the atmosphere. The impact of weather on FSO links is described in Section 2.4. Mechanical gimbals as a method for active FSO alignment and tracking are introduced in Section 2.5. In Section 2.6, active beam steering elements are discussed. Section 2.7 is devoted to FSO link acquisition. Section 2.8 contains an overview of current ground-to-UAV communications methods. A summary of this chapter is given in Section 2.9.

2.2   Fundamentals of FSO Communications Systems

This section introduces the fundamentals of FSO systems. This review of fundamentals is intended to give the reader a basic knowledge of what FSO systems are and how they operate as well as factors that influence the performance of FSO communications links.

2.2.1 Overview of FSO Operation

Free-space optical systems are optical communications systems that operate as a fiber-less optical communications link. FSO systems are generally designed to operate in the infrared (IR) spectral range [1,15]. FSO systems are point-to-point communications links that consist of an optical transmitter on one end of the link and an optical receiver on the other end of the link. FSO technology is a line-of-sight technology, which means that a clear unobstructed path is needed between the transmitter and the receiver. Commercially available FSO systems are designed in order to facilitate transmission of the signal bi-directionally between the transmitter and the receiver.

Commercial FSO systems in use today operate around 850 and 1550 nm, which corresponds to frequencies around 200 THz. This is a very important fact because the Federal Communications Commission (FCC) does not regulate frequency use above 300 GHz [1].

2.2.2 Components of an FSO System

FSO systems are a point-to-point communications link consisting of an optical transmitter and receiver. Figure 2.1 shows a schematic view of a basic FSO system. As shown in the figure, in its most basic form, the FSO transmitter consists of a light

source (laser or LED), and optical components in order to control various parameters of the laser such as divergence. At the receiving end, incoming light passes through a lens where it is focused onto a photodetector.
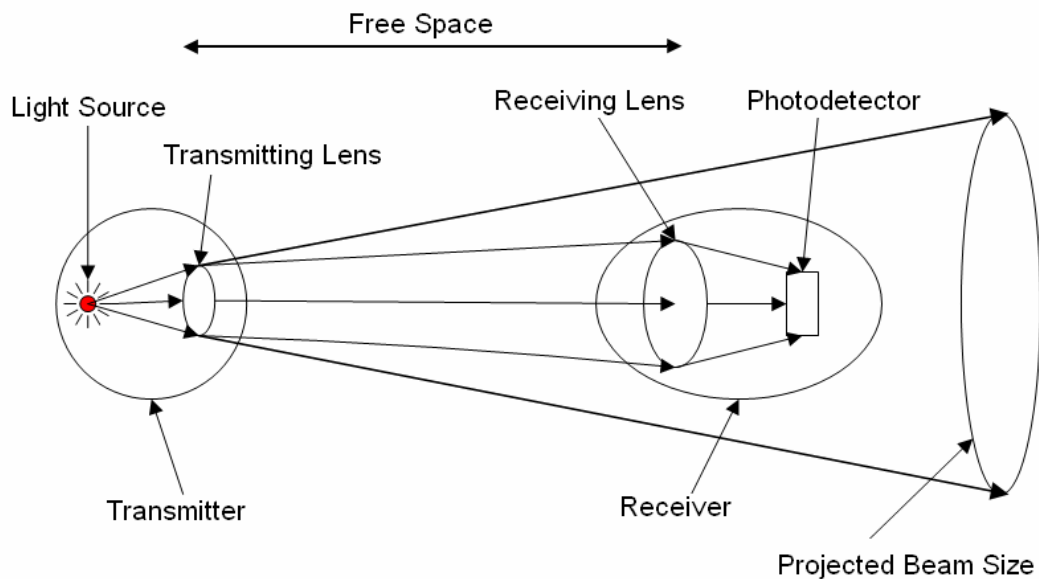
Figure 1.1 Schematic of a Free-Space Optical Transmission System [1].

2.2.3 FSO Transmitters and Receivers

Figure 2.2 below shows a simplified view of a single-beam FSO transceiver developed by LightPointe [15]. This simplified view will be used to discuss the basics of both FSO transmitters and receivers.
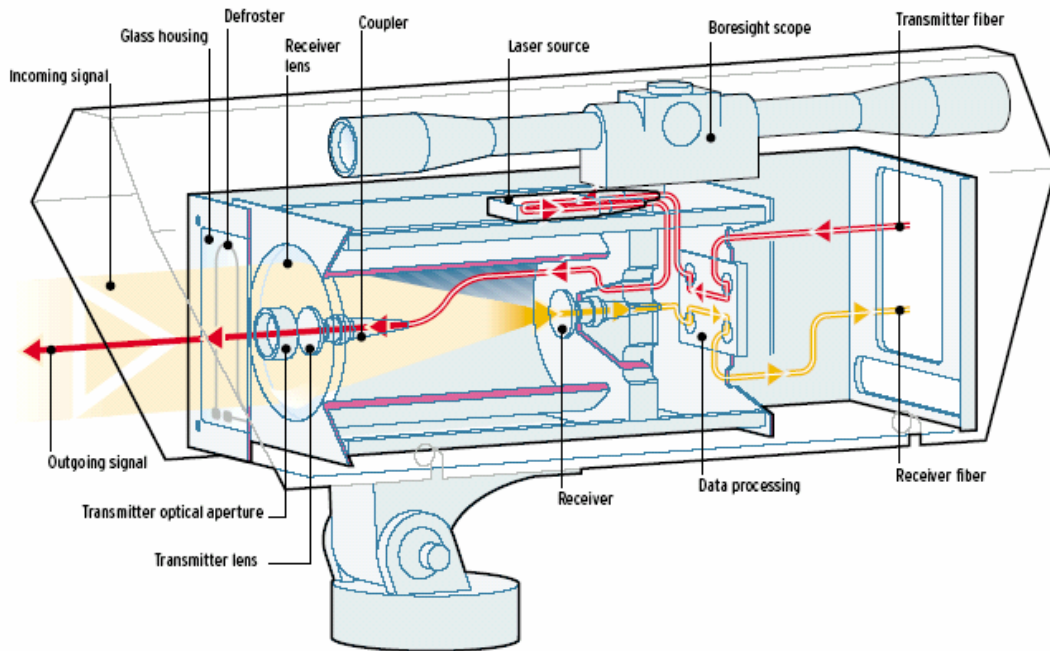
Figure 2.2 Simplified drawing of a single-beam LightPointe transceiver [15].

2.2.3.1 Transmitters

Modern FSO systems make use of a variety of light sources for the transmission of data. Depending on the distance of the FSO link to be established, either a light-emitting diode (LED) or a laser light source is used in the FSO transmitter. Furthermore, in currently developed FSO systems erbium doped fiber amplifiers may be used to amplify the optical power of the transmitter. After light is emitted by the LED or laser source, it passes through a series of lenses in the transmitter that are used to control the amount of divergence present in the laser beam.   More complicated FSO transmitters may also include some type of active optical element

11

such as a steerable mirror to allow for adjustment to the FSO unit's alignment or to provide some form of active tracking of the FSO link.

FSO transmitters employ in-plane laser dides for direct modulation using either Fabry-Perot resonator cavities or distributed feedback (DFB) lasers.   Figure 2.3 shows the structure of a Fabry-Perot resonator cavity for a laser diode.
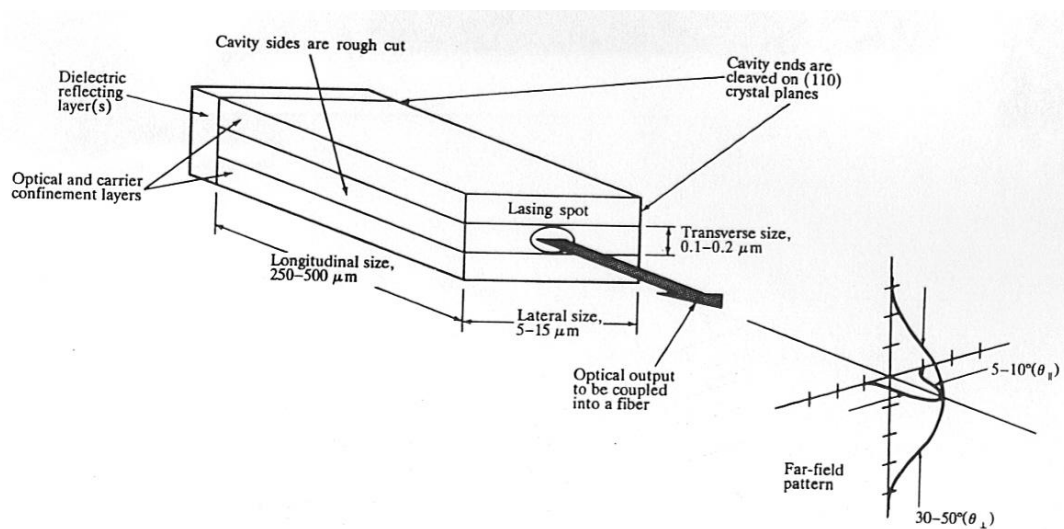
Figure 2.3 Fabry-Perot resonator for a laser diode [35].

In a laser diode Fabry-Perot resonator, a pair of flat partially reflecting mirrors face each other and enclose the cavity. These mirrors provide a strong optical feedback in the longitudinal direction which converts the device into an ocsilator with a gain mechanism that compensates for optical losses in the cavity [35].

Figure 2.4 shows the structure of a DFB laser. In DFB lasers, cleaved facets are not required for optical feedback.
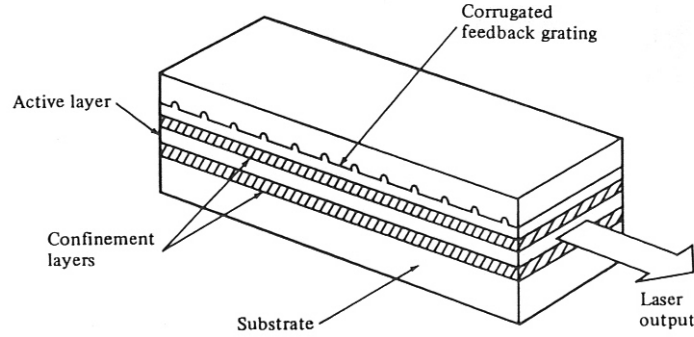
Figure 2.4 Structure of a distributed-feedback (DFB) laser [35].

Lasing is achieved in DFB lasers from Bragg reflectors or periodic variations of the refractive indices which are incorporated into the multilayered structure along the length of the diode [35]. Partially reflected waves in the Bragg reflector construct a reflected wave when the Bragg condition is met, which is given by

$$q(\lambda_B / 2\eta) = \Lambda,$$

(2.1)

where λ_B is the Bragg wavelength, given by

$$\lambda_B = \frac{2n_e\Lambda}{k},$$

(2.2)

with n_e being the effective refractive indes of the mode, k is the order of the mode, Λ is the period of the corrugations and q is an integer. In the DFB laser, the grating for the wavelength selector is formed over the entire active region and the longitudinal modes are spaced symmetrically around λ_B at wavelengths given by

$$\lambda = \lambda_B \pm \frac{\lambda_B^2}{2n_e L_e}\left(m + \frac{1}{2}\right),\qquad(2.3)$$

where m is the mode integer and L_e is the effective grating length [35].

2.2.3.2   Receivers

The receiving end of the FSO unit also consists of a series of lenses that focus the incoming light signal onto a light detector. However, in simple FSO systems for short range applications, both the transmitting portion and receiving portion may in fact be directly linked to an optical fiber. In this case, the signal remains in the optical domain at the receiving end and the purpose of the lenses in the receiver are to focus the light in order to couple it into the fiber. In systems in which the received optical signal is converted back into an electrical signal, the receiving lenses will focus the light onto a photodiode, where it is converted into an electrical signal.

Commonly, FSO receivers use *pin* (*p*-intrinsic-*n*-type) photodiodes in their configuration, for which a schematic depiction is shown in Figure 2.5.
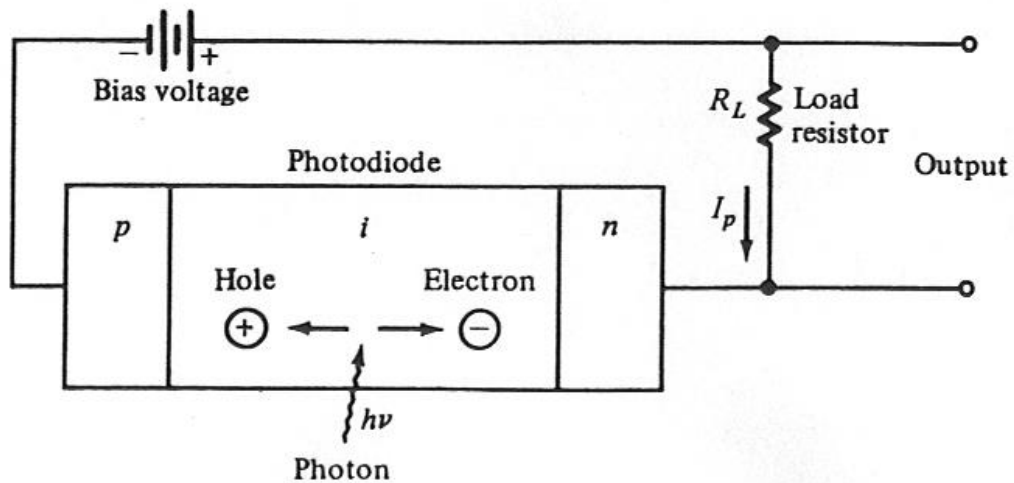
Figure 2.5 Schematic representation of a *pin* photodiode circuit with an applied reverse bias [35].

Pin photodiodes consist of *p* and *n* layers separated by a very lightly *n*-doped instinsic (*i*) layer. A voltage with a sufficiently large reverse bias is applied across the device, depleting the intrinsic layer of carriers. If a photon with an energy greater or equal to the bandgap energy strikes the diode, the photon generates a free electron-hole pair. This gives rise to a high electric field in the depletion region, which in turn generates a current to flow in the external circuit [35]. This current is known as the photocurrent.

2.2.4 Link Margin Analysis

As is the case when designing a fiber optic transmission system, a link margin analysis is required for the design of FSO links. In general, engineers will know the minimum power level that the FSO transceiver is able to detect and needs to ensure that sufficient power is transmitted in order to meet this requirement. However, unlike in a fiber-based system, the amount of loss that is present in an FSO system varies depending on weather conditions (for example if dense fog is present transmission is virtually impossible). In FSO links, four different sources of signal degradation need to be considered: optical loss, geometric loss, pointing loss, and atmospheric loss.

2.2.4.1 Optical Loss

Optical loss in FSO links is the loss in the link due to imperfections in lenses and other optical components in the transmitter and receiver (such as couplers) [1]. Optical loss is a loss that is inherent in the system, and other than minimizing the number of couplers and purchasing high quality lenses, little can be done to overcome optical losses in the system.

2.2.4.2   Geometric Loss

Geometric loss refers to the losses that occur due to the divergence of the optical beam [1].   Divergence is one method that is used to simplify the alignment and tracking required to deploy FSO links.   Because of the divergence present in the link, a large portion of the light beam is not in fact collected by the receiving optics.   The amount of geometric loss present in a link can by calculated based on the areas of both the transmitting and receiving optics, the divergence in the system and the separation of the transmitter and receiver.   If the transmitter and receiver lenses are measured in centimeters, the distance between the transmitter and receiver is measured in kilometers and the divergence is in milliradians, then the geometric loss in the system is given by:

$$\frac{A_R}{A_B} = \left[\frac{D_R}{D_T + 100 \times d \times \theta} \right]^2, \tag{2.4}$$

where A_R is the area of the receiver and A_B is the area of the beam.

2.2.4.3   Pointing Loss

Pointing loss is the loss in the system due to inaccurate alignment of the system.   For a fixed, manually aligned link, this loss would be due simply to an inaccurate initial

17

alignment of the system. For active alignment links, the pointing loss may occur due to residual steady-state errors [1]. Pointing losses in fixed systems are normally only prevalent if the link is longer than 3 km.

2.2.4.4 Atmospheric Loss

Atmospheric losses occur due to the atmosphere causing signal degradation and attenuation through various mechanisms. The atmosphere degrades and attenuates the FSO signal through absorption, scattering (mainly Mie scattering) and scintillation [1]. Section 2.3 will give a more detailed description of atmospheric effects that are present in an FSO communications link.

2.3 Optical Properties of the Atmosphere

Atmospheric factors such as rain, snow, sleet, fog, haze and pollution affect the transmission of electromagnetic radiation through the atmosphere, which is especially true for laser beams. There are three atmospheric processes that affect optical wave propagation, namely absorption, scattering, and turbulence (also known as refractive index fluctuations) [30]. Absoption and scattering occur due to the gases that constitiute the atmosphere and other particles present in the atmosphere. Absorption and scattering cause attenuation of the laser beam. Turbulence present in the

atmosphere causes irradiance fluctuations, beam broadening and loss of spatial coherence of the optical wave.

The earth's atmosphere is divided into four primary layers which are based mainly on temperature variations. Figure 2.6 shows these layers and the boundaries inbetween the layers.
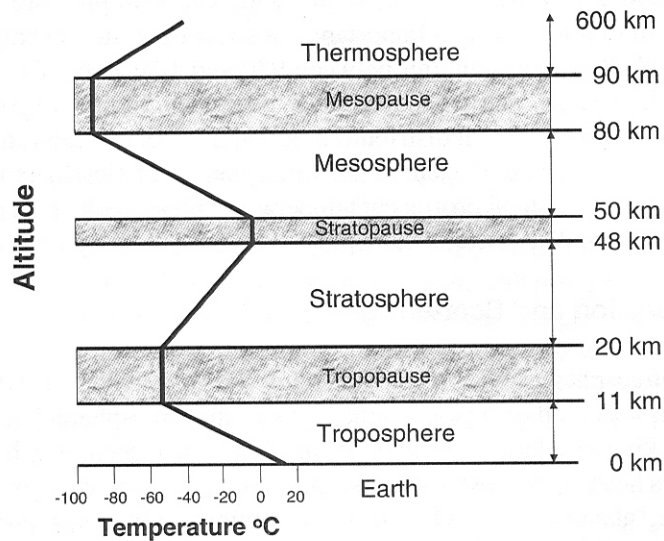
Figure 2.6 Diagram depicting various atmospheric layers and air temperatures [30].

The troposhphere, which extends from the earth's surface to approximately 11 *km* is the most dense layer of the atmosphere, and is the layer in which most weather conditions occur. The troposhere is the layer of the atmosphere in which the work presented in this dissertation will be focused.

2.3.1 Absorption and Scattering

Absorption in the earth's atmosphere occurs when photons are absorbed by gaseous molecules where they are converted into kinetic energy [30]. This means that the atmosphere is heated through the process of absorption. The process of absorption is highly wavelength dependent [1]. Figure 2.7 shows a typical atmospheric transmittance for a horizontal 1 *km* path for a range of wavelengths from 0 to 15 *μm*. This figure shows the wavelength dependence of absorption.
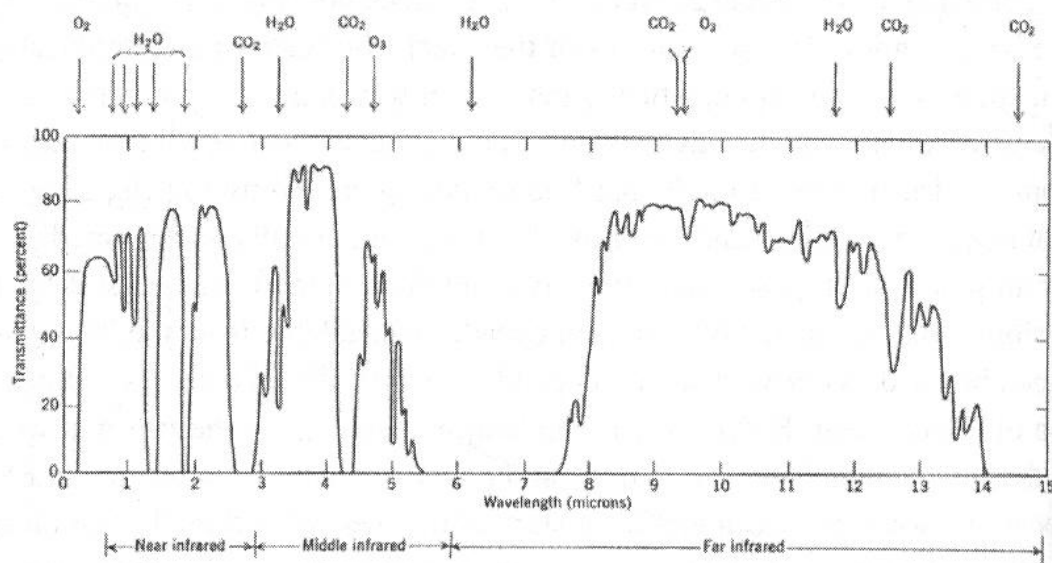
Figure 2.7 Typical atmospheric transmittance for a horizontal 1 *km* path [31].

The imaginary part of the index of refraction, *k*, is related to the absorption coefficient, *α*, by [1]:

$$\alpha = \frac{4\pi k}{\lambda} = \sigma_a N_a, \tag{2.5}$$

where σ_a is the absorption cross section and N_a is the concentration of the absorbing particles.

In a similar fashion to absorption, light scattering is also a strongly wavelength dependent phenomon that occurs in the atmosphere. Scattering is understood to be a redirection or redistribution of light that leads to a significant reduction in the intensity of the light at the receiver end of an FSO communications link [32]. Several different types of scattering occur, depending on the particle size which the light wave encounters. Two of these scattering regimes are Rayleigh and Mie scattering.

Rayleigh scattering occurs due to particles such as air molecules and haze, which are small in comparison to the wavelength of the incident light. Rayleigh developed a classic formula for scattering which is given by [1]

$$\sigma_s = \frac{f e^4 \lambda_0^4}{6 \rho \varepsilon_0^2 m^2 c^4} \frac{1}{\lambda^4}, \tag{2.6}$$

where f is the oscillator strength, e is the charge on an electron, λ_0 is the wavelength corresponding to the natural frequency, $\omega_0 = 2\pi c/\lambda_0$, ε_0 is the dielectric constant, c is the speed of light, and m is the mass of the oscillating entity. Based on the λ^{-4}

dependence it can be seen that shorter wavelengths will be scattered more readily than longer wavelengths. For this reason, Rayleigh scattering is generally neglected for FSO communications systems that operate in the near infrared range.

Mie scattering occurs for particles that are of a similar size to the wavelength of the light incident on the particle. This dependence implies that near infrared wavelengths are affected by fog, haze and pollution aerosols [1]. An emperical formula for Mie scattering is given by [32]

$$\gamma = \frac{3.91}{V}\left(\frac{\lambda}{550}\right)^{-\delta},$$ (2.7)

where $\delta = 0.585(V)^{1/3}$ for $V < 6\ km$, $\delta = 1.6$ for $V > 50\ km$, $\delta = 1.3$ for $6\ km < V < 50\ km$. V corresponds to the visibility and λ is the transmission wavelength.

Often times, absorption and scattering are grouped together under the term extinction, which is defined as the amount of radiance passing through the atmosphere. The atmospheric transmittance of light that has propagated a length L is related to extinction through Beer's law, which is expressed as [32,33]:

$$\tau = e^{-\alpha(\lambda)L},$$ (2.8)

where $\alpha(\lambda)$ is the extinction coefficient.

2.3.2 Optical Turbulence

In hot, dry climates, atmospheric turbulence affects optical transmission. As the atmosphere is heated, small temperature variations develop. These temperature variations cause refractive index variations in the atmosphere. Turbulent air flow can be represented by a series of eddies of various sizes, extending from large scale which is called the outer scale, L_0, to small scale which is called the inner scale, l_0. Under the influence of inertial forces, large eddies can break up into smaller ones, which forms an inertial range in the atmospere [30]. This inertial range is shown in Figure 2.8.
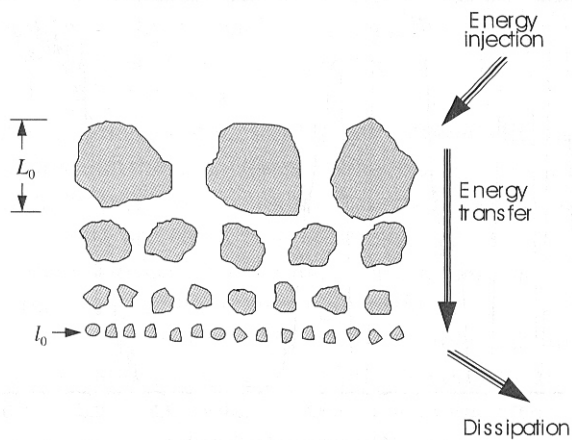
Figure 2.8 Kolmogorov cascade theory of turbulences [30].

Atmospheric turbulence is characterized by three parameters. These parameters are the inner and outer scale and the structure parameter of the refractive index fluctuation, C_n^2, which is a measure of the strength of the optical turbulence [30].

Atmospheric turbulence affects FSO transmission in three different ways, namely beam wander, scintillation and beam spreading. Beam wander occurs in the presence of large cells of turbulence compared to the beam diameter [1]. The radial beam variance, σ_r, as a function of wavelength and distance is given by [1]

$$\sigma_r = 1.83 C_n^2 \lambda^{-1/6} L^{17/6}. \tag{2.9}$$

From Equation (2.9) it is observed that shorter wavelengths are more susceptible to beam wander.

Scintillation affects FSO transmission the most of the three turbulence effects. Random interference due to scintillation with the wave front can cause peaks and dips which cause receiver saturation or signal loss in FSO communications links. Scintillation effects for small fluctuations have been shown to follow a log-normal distribution which is characterized by the variance, σ_i, and is defined by [1]

$$\sigma_i = 1.23 C_n^2 k^{7/6} L^{11/6}, \tag{2.10}$$

where $k = 2\pi/\lambda$. For large fluctuations, the varians is given by [34]

$$\sigma^2_{high} = 1.0 = 0.86(\sigma^2)^{-2/5}.$$ (2.11)

This relationship shows that shorter wavelengths will experience a smaller variance.

The final effect due to turbulence is beam spreading. The beam size is characterized by the effective radius, a_t, which is the distance from the center to the beam to where the relative mean intensity has decreased by $1/e$ [1]. The effective beam radius is given by [1]

$$a_t = 2.01(\lambda^{-1/5}C_n^{6/5}z^{8/5}).$$ (2.12)

It is noted that the wavelength dependence of beam spreading is not strong. Chapter 5 of this dissertation will discuss atmospheric turbulence in more detail.

2.4   Impact of Weather on FSO Communications

Different weather phenomena affect the useful range of FSO communications equipment. In this section, a description of the effect of these weather phenomena is discussed. Table 2.1 shows the international visibility codes for weather conditions

and precipitation, along with the achievable FSO link distance in these weather conditions.

Rain has a distance reducing effect on FSO communications links, but the effect is less significant than that of fog. It is noted that the effects of rain are far more significant on RF wireless links in the 10 *GHz* range than of FSO links. This is due to a closer match between RF wavelengths and raindrop radii. Snow present in the atmosphere causes a beam attenuation somewhere in between the effects of light rain and moderate fog. Fog is the weather condition that causes the largest amount of signal degredation in FSO links. Fog is composed of small water droplets that have radii that are comparable to FSO wavelengths. This causes scattering to become prevalent when fog is present in the atmosphere [1]. Chapter 6 of this dissertation will contain an in depth analysis of FSO performance in the presence of different weather phenomena.

Weather Condition	Precipitation		Amount (mm/hr)	Visibility	dB Loss/km	Deployment Ranges (m)
Dense fog				0 m 50 m	-271.65	122 m
Thick fog				200 m	-59.57	490 m
Moderate fog	Snow			500 m	-20.99	1087 m
Light fog	Snow	Cloudburst	100	770 m 1 km	-12.65 -9.26	1565 m 1493 m
Thin fog	Snow	Heavy rain	25	1.9 km 2 km	-4.22 -3.96	3238 m 3369 m
Haze	Snow	Medium rain	12.5	2.8 km 4 km	-2.58 -1.62	4331 m 5566 m
Light haze	Snow	Light rain	2.5	5.9 km 10 km	-0.96 -0.44	7146 m 9670 m
Clear	Snow	Drizzle	0.25	18.1 km 20 km	-0.24 -0.22	11468 m 11743 m
Very clear				23 km 50 km	-0.19 -0.06	12112 m 13771 m

Table 2.1 International visibility codes for weather conditions and precipitation.

2.5 Gimbal Systems

A gimbal is a mechanical device used to change the direction in which a mounted device such as a camera or FSO transmitter is aligned. Gimbals are often used to mount security cameras in order to allow security personnel to scan a larger area with a single movable camera. Typically gimbals are able to move both vertically as well as horizontally. The internal control mechanism in gimbals is normally either servo-based or based on a series of stepper motors.

New developments in gimbal design have been demonstrated that have led to the production of next generation gimbals suitable for active FSO alignment [36,37]. One such next generation gimbal is the Omni-Wrist III which was developed under Air Force funding and is a gimbal that emulates the kinematics of a human wrist [38]. Figure 2.9 shows a photograph of the Omni-Wrist III gimbal. The Omni-Wrist III gimbal has the following performance characteristics: This next generation gimbal has 70 arc seconds average repeatability with over 180 degrees of azimuth and declination.

Figure 2.9 Omni-Wrist III Sensor Mount [38].

The Omni-Wrist III sensor has already been used to develop a hybrid laser-beam steering system for laser communications [39]. While a next generation gimbal such as the Omni-Wrist III is able to provide an excellent range of motion, a gimbal-based alignment system cannot provide the wide bandwidth necessary to offset vibrations present on the FSO mounting platform. Figure 2.10 illustrates how a gimbal alone cannot provide sufficient bandwidth for an FSO system. As shown in the figure, a gimbal does have a large range of motion, but does not provide a large bandwidth. On the other hand, active optical components, such as a Bragg cell, provide a large bandwidth, but do not have a large range of motion. For these reasons, a hybrid tracking system for FSO communications links have been proposed by several researchers in order to incorporate the best features of both gimbals and Bragg cells or other active optical elements.
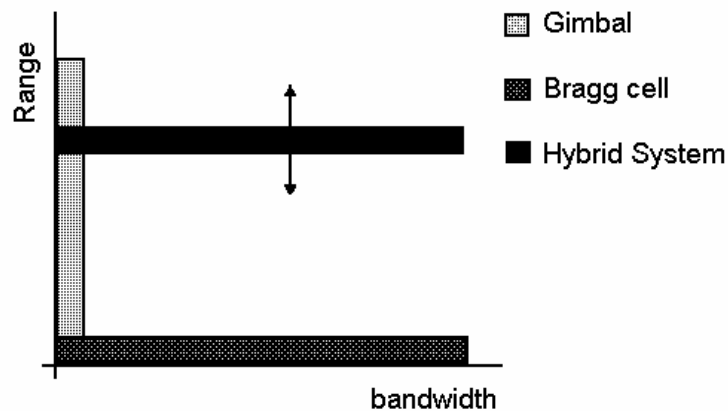
Figure 2.10 A plot showing range versus bandwidth for different FSO beam steering configurations [39].

Because of the need for hybrid steering systems, particularly for FSO communications links between moving platforms, Section 2.5 will discuss several different active beam steering elements as possible solutions for the design of a hybrid FSO beam steering system.

2.6   Active Beam Steering Elements

A significant amount of research has been performed on the use of active optical elements for laser beam steering and tracking [39-46]. While a gimbal is generally a good enough tracking device to follow even a mobile platform, other factors also affect the tracking of an FSO link.   One of the main problems facing FSO communications to moving platforms is the requirement to offset the vibration present in the FSO mounting platform. Active optical components are generally used to offset this vibration. Several different types of active optical elements need to be considered for the active tracking of FSO links. Some possibilities are listed below:

- MEMS based tracking
- Fast Steering Mirrors (FSM)
- Acousto- or electro-optic modulators

MEMS devices were developed by Texas Instruments and consist of an array of 1024 × 768 micro-mechanical mirrors. Each mirror in the array can be individually deflected around a diagonal axis to ±12°.

FSM's use linear actuators to drive a mirror through a range of motion with an extremely fine resolution. Modern FSM's can provide 3-D movement with resolutions as fine as 1 μrad. These mirrors have rapid accelerations in the order of 1000 rad/s^2. Figure 2.11 shows a photograph of an FSM.

Figure 2.11 Fast Steering Mirror from Ball Aerospace [47].

Acousto-optic deflectors are solid state devices that make use of an acoustic wave to change the angular direction of a laser beam. These devices are further advantageous due to their ability to simultaneously modulate the laser beam. Figure 2.12 shows a schematic view of an acousto-optic Bragg deflector. The device steers the incident light beam by changing the frequency of an acoustic wave that passes through the

31

device. This change in frequency causes an index of refraction change in the device, and the light beam is deflected a certain amount which is given by

$$\Theta_D = \frac{\lambda f}{n \upsilon} - 2\Theta_B,$$
(2.13)

where Θ_B is the Bragg angle, λ is the wavelength, f is the acoustic frequency, n is the refractive index and υ is the acoustic velocity.
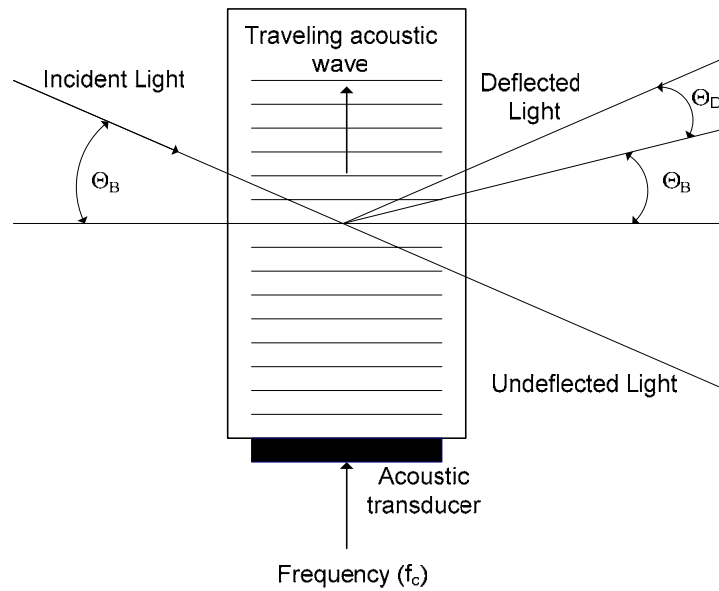
Figure 2.12 Bragg cell operation [39].

Each of the different methods of performing active optical tracking has different advantages and disadvantages. For example, while an acousto-optical tracking system has an extremely rapid response time; it is also limited in the amount of

optical power that the acousto-optic cell can reflect without being permanently damaged.

2.7   Acquisition of FSO Communications Links

The first step in developing an acquisition and tracking system for an FSO link is to properly understand the concept of acquisition in FSO links. This section will introduce acquisition techniques that have been reported in research literature.

The process of acquisition in FSO links refers to the process whereby a link is established between the transmitter and the receiver. For traditional terrestrial FSO links, the acquisition process is a manual process during which the FSO transmitter and receiver are manually aligned using a telescopic sight and other optical testing equipment. The process of manually aligning FSO units is considered to be a quick process, but the actual time to install the FSO equipment is on the order of hours. While a couple of hours might be considered a "fast installation" for a permanent optical link, to establish an FSO link to a mobile platform, some kind of active link acquisition is needed.

2.7.1 Signal Acquisition based on a GPS System

To develop an automated acquisition system for an FSO link, it is essential for the acquisition system to have a starting point from which to begin a seek algorithm. Research has been performed into using a Global Positioning System (GPS) based alignment system for FSO systems [48,49]. These systems use GPS coordinates for the initial alignment and then use either received signal strength or a CCD camera to perform the fine alignment. A GPS-based system needs a fine alignment protocol due to the inherent normal distribution error associated with GPS systems.

2.7.2 Acquisition in Short-range FSO Links

Beam pointing and acquisition issues in free-space laser communications for satellite based systems have been investigated by many researchers [17, 21-24]. However, all of these works consider long-range links that utilize narrow beamwidths and generally make use of slow, bulky beam-scanning devices such as gimbaled telescopes. The acquisition process for short-range (1 – 10 km) FSO links between moving parties when covertness is the overriding system performance requirement has also previously been investigated [50].

Beam acquisition requires the use of different search algorithms. Chapter 5 of this dissertation will discuss the use of a raster scan for FSO link acquisition. Raster

scans are sequential scans in which the FSO transmitter moves from one search point to the next as shown in Figure 2.13.
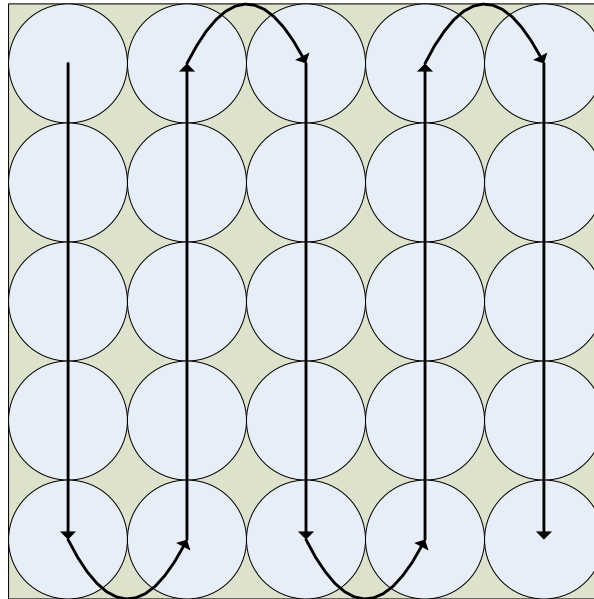
Figure 2.13 Raster scan algorithm.

The time during which link acquisition takes place in an FSO link is the time during which the link is most susceptible to interception. For this reason, a large focus must be given to minimization of link acquisition times.

2.8   Current UAV Communications Methods

At present, UAVs such as the Predator developed by the U.S. Air Force [3] use UHF and VHF radio relay links for communication, a C-band line-of-sight data link with a

150 nautical mile range as well as UHF and Ku-band satellite links. The use of millimeter technology requires the use of far larger telescope apertures [8], which is shown in Figure 2.14.
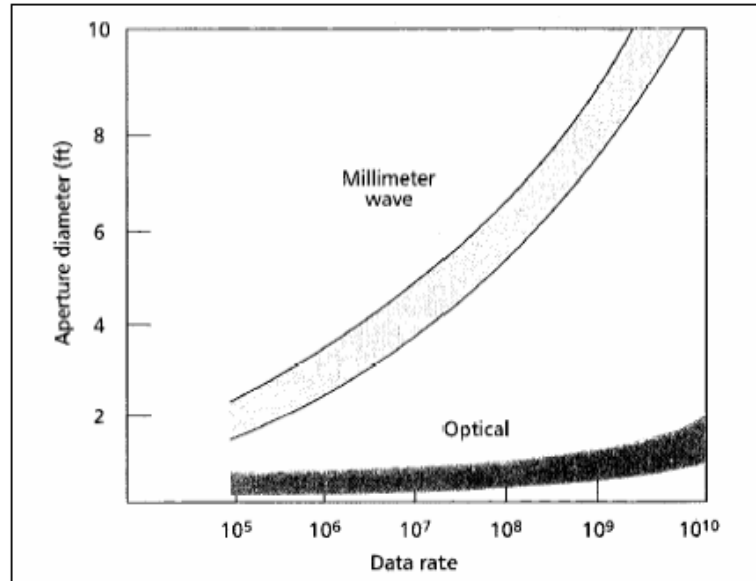
Figure 2.14 Telescope aperture vs. data rate for millimeter and optical waves [8].

2.9 Summary

FSO systems consist of an optical transmitter and receiver in which data is transmitted through the atmosphere. The technology is similar to that of the fiber optic industry. The use of FSO introduces several types of signal loss that are not present in fiber optic based communications.

Active alignment and tracking of FSO communications links requires the use of a hybrid system containing both a mechanical gimbal and some for of active beam steering element. A search algorithm is necessary in order to perform the alignment protocols.

Chapter 3

Theoretical Analysis of FSO Communications

Links

3.1   Introduction

In this chapter, a theoretical analysis of beam steering tolerances and divergences for FSO communications links will be discussed [13]. Furthermore, a study in which different active beam steering elements are compared will be presented, along with an analysis to show the importance of using active beam steering elements to offset the platform vibrations present in FSO communications links [14]. Finally, a mathematical model of a ground-to-UAV FSO communications link will be presented.

The remainder of this chapter is organized as follows: Section 3.2 contains the beam steering tolerance analysis. The active beam steering element comparison will be presented in Section 3.3, along with a platform vibration analysis. In Section 3.4, a mathematical model of a ground-to-UAV FSO communications link is described. Concluding remarks will be made in Section 3.5.

3.2   FSO Beam Steering and Divergence Analysis

In order to determine the range over which FSO communications links are theoretically feasible, an analysis of the beam steering capabilities of a mechanical gimbal along with calculations of the amount of divergence expected in the FSO communications links is required.   As was discussed in Section 2.2.4.2, geometric loss is a major limiting factor in FSO communications links.   In this section, an analytical analysis of a gimbal's beam steering tolerances along with divergence and geometric loss calculations for various length FSO communications ranging from terrestrial links to deep-space communications links will be presented.

3.2.1 Link Configuration

Figure 3.1 shows the basic FSO link configuration that was used for the divergence, geometric loss and beam steering tolerances presented in this chapter.   A simple point-to-point link configuration, with a variable transmitter-receiver separation is considered.   Several assumptions with regard to available FSO equipment were used in order to perform this analysis.   The assumptions used in this analysis were:

1. The transmitting equipment required to launch the light is available and is of sufficient power to transmit the light the required distance.

2. A clear, unobstructed line-of-sight path between the transmitter and receiver is always present.

3. The amount of beam divergence due to the transmitting equipment can be controlled to limit geometric loss in the communications link.

4. Vibrations present in the mounting platforms are negligible or can be assumed to have been off-set through the use of active optical methods.
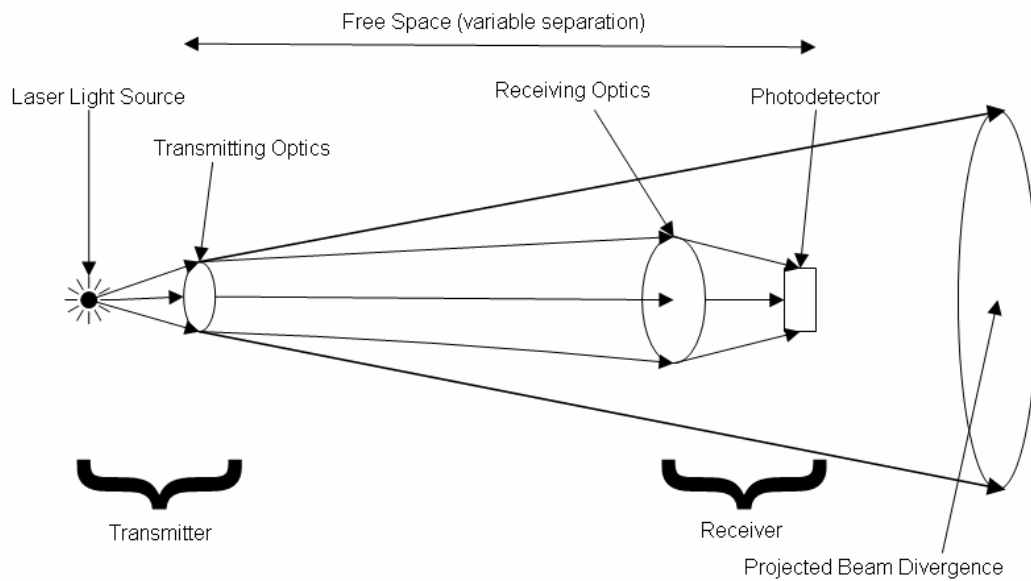
Figure 3.1 FSO link configuration for divergence calculations.

As shown in Figure 3.1, the separation distance under consideration for calculation is a variable distance. In this section, various distances of interest will be considered. Under consideration for this investigation are the following scenarios:

1. A terrestrial 4 km FSO communications link.

2. A 13 km FSO communications link between a ground station and a commercial airliner.

3. An FSO communications link between a ground station and a satellite in Earth-orbit at 20,200 km.

4. An Earth-Moon FSO communications link of 384,000 km.

5. An Earth-Mars FSO communications link at both the closest and furthest points of orbital separation.

6. A deep-space FSO communications link between Earth and the end of the Solar System.

The amount of divergence present in an FSO link is an important factor due to a couple of reasons. First, the amount of divergence present in the link directly affects the amount of optical power that is lost in the link due to geometric losses, as was discussed in Chapter 2. Second, when attempting to perform any automatic alignment process using mechanical means, such as a gimbal, the minimum step size of the gimbal may prove to be too large in magnitude to allow for a complete scan of the alignment search area. Figure 3.2 shows how divergence affects beam steering tolerances when using a gimbal-based alignment system.
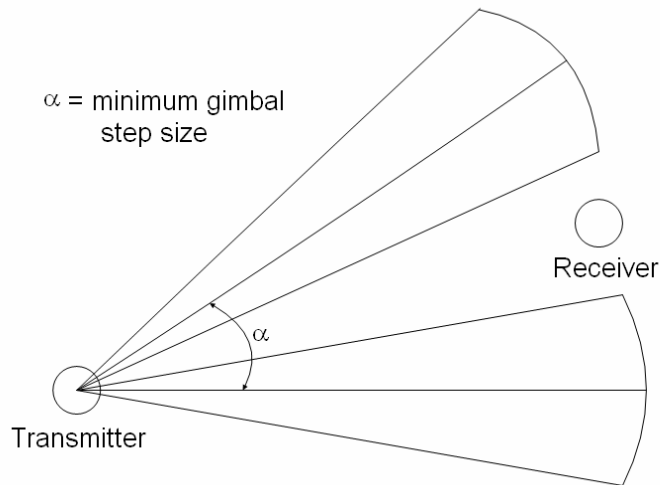
Figure 3.2 For long-range FSO links the gimbal step size may be too large to accurately

steer the laser beam.

The analytical calculations performed in the chapter are based on the specifications of the Sagebrush Technology Model-20 Pan and Tilt gimbal [52], which is a servo-based gimbal that provides a positional resolution of 0.004°. Divergence calculations are based on average divergences for commercially available FSO equipment and calculated divergences for long-range applications. A detailed experimental analysis of the Model-20 Pan and Tilt gimbal will be presented in Chapter 4 of this dissertation.

Following the beam steering tolerance, divergence and geometric loss calculations presented, a section devoted to the analysis of an FSO link between a ground terminal and an aircraft in flight will be discussed.

3.2.2 Beam steering and divergence calculation results

In this section, the calculated results for the beam steering tolerances and divergences are reported based on the link configuration described in Section 3.2.1. The results shown are for beam steering tolerances based on mechanical gimbal alignment with no active optical steering component.

3.2.2.1 Gimbal-based beam steering tolerances

The beam steering tolerances for the FSO communications links described in Section 3.2.1 are discussed in this section. Figure 3.3 shows a plot comparing the center-to-center distances of consecutive beam profiles attainable between consecutive gimbal movements based on the minimum step size of 0.004°. The data in this plot does not take beam divergences into account, only the beam steering ability of the gimbal. Beam divergence will be discussed in more detail in the next section of this dissertation.
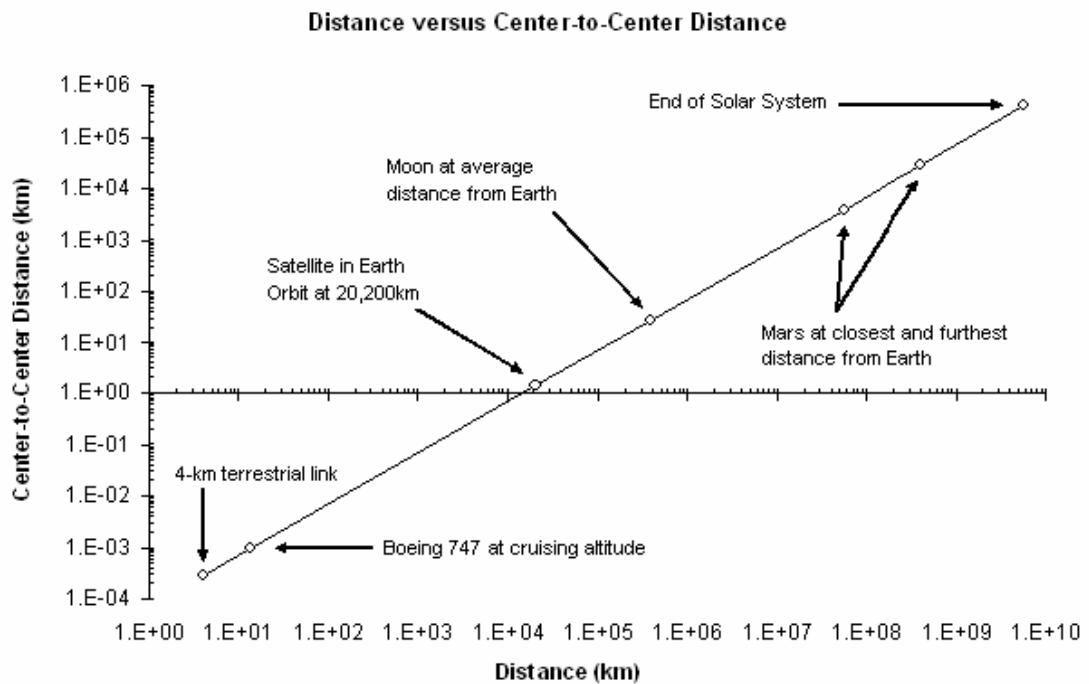
Figure 3.3 Steering tolerances achievable using Sagebrush Technology Model-20

Pan and Tilt Gimbal.

From Figure 3.3, it can be seen that while a mechanical gimbal is able to provide beam steering tolerances on the order of meters for terrestrial links and long range Earth-Air FSO communications links, for deep space communications the steering tolerances can exceed the order of 10^5km. Based on these beam steering tolerance calculations it can be concluded that for FSO communications links longer than approximately 20,000 km a mechanical gimbal-based alignment system cannot provide a sufficiently fine steering tolerance to perform an initial alignment procedure or to actively track the FSO communications link.

3.2.2.2 *Beam divergence calculations*

The beam divergence present in an FSO communications link is one method that can be used to offset limitations in the system due to beam steering tolerances. The geometrically calculated beam divergence data is discussed in this section. A beam divergence of 0.1°, which is a magnitude of divergence that is common to many commercial FSO systems, was used to calculate the data for the first data set. Following the standard beam divergence calculations, further divergence calculations were performed for a divergence limited FSO communications link. The divergence limited system is necessary for both ultra-long and deep space FSO links due to the large amount of geometric loss beam divergence introduces to these links. Figure 3.4 shows a plot of beam divergence for various distances of interest.

Based on the divergence calculations performed it is observed that for deep space FSO links, a severely divergence-limited FSO link is required. A comparison of Figure 3.3 and Figure 3.4 shows that based solely on a comparison of beam steering tolerances and divergence in links in which a divergence-limited FSO beam is required, a mechanical gimbal alignment system is unable to provide sufficient steering tolerance to perform link acquisition or tracking.
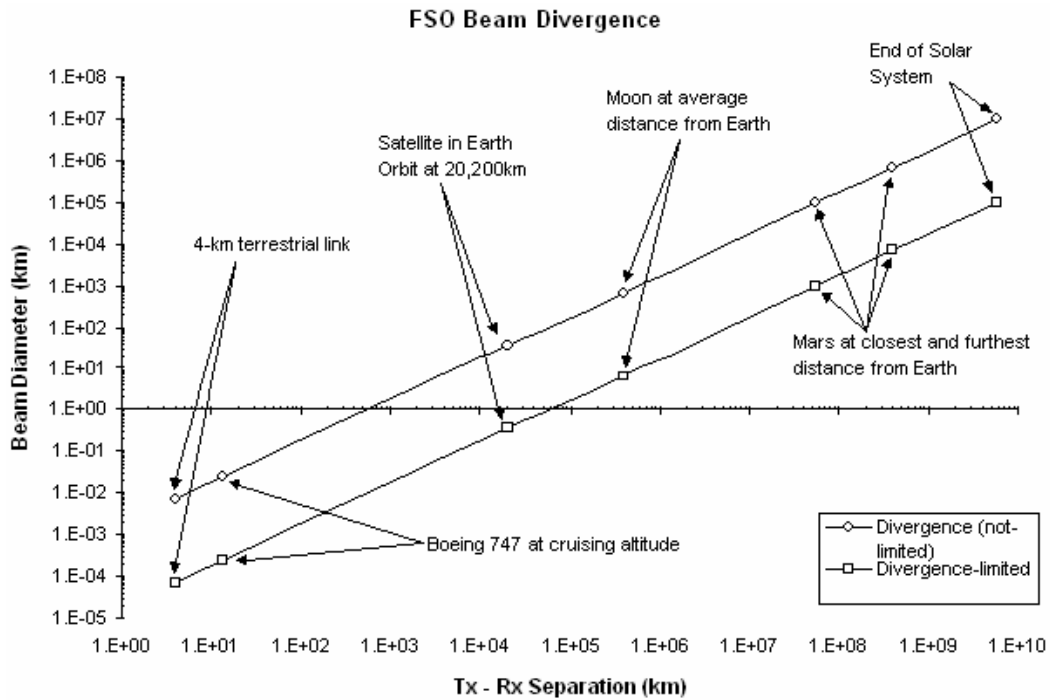
Figure 3.4 FSO beam divergence for various distances of interest showing calculations for both divergence-limited and non-divergence-limited situations.

3.2.2.3 *Geometric loss calculations*

Geometric loss is a major factor in limiting the performance of FSO communications links. In this section, calculated geometric losses based on different FSO transmitter and receiver configurations are presented. Three separate geometric loss calculations were performed for the six FSO links discussed in Section 3.2.1:

1. An FSO communications link using a common terrestrial beam divergence of 0.1° with small receiver and transmitter apertures.

2.   An FSO communications link using a divergence limited laser beam and small receiver and transmitter apertures.

3.   An FSO communications link using a divergence limited laser beam and large receiver and transmitter apertures, such as a large terrestrial telescope receiver, or an array of smaller telescopic receivers.

Figure 3.5 shows a plot of geometric loss for the different FSO links.
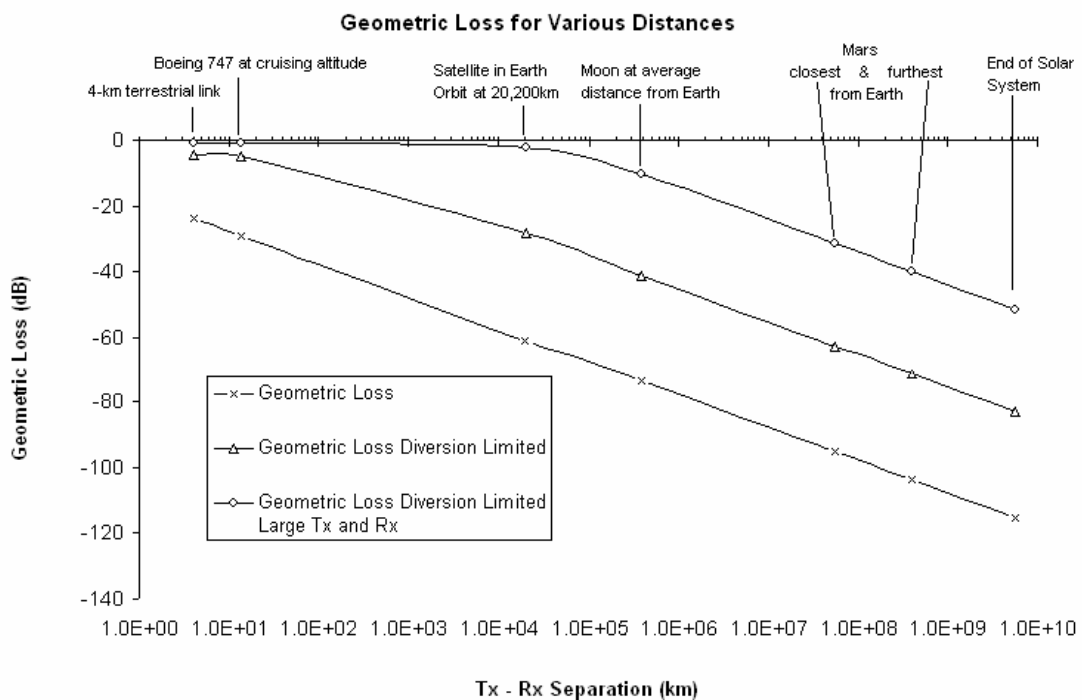
Figure 3.5 Geometric loss calculations for various distances of interest.

Using a threshold of 60 *dB* for a link to perform adequately, it can be seen that for a standard FSO system, the geometric loss becomes a system limiting factor for links longer than a ground-to-satellite link. A 60 *dB* link margin is larger than is generally used for terrestrial FSO applications, but for deep space communications, devices such as photon counting detectors and optical wavelength filters can be employed in order to increase the receiver sensitivity. For the divergence limited system, geometric loss becomes a limiting factor for links longer than an Earth-to-Mars link when Mars and Earth are at their closest orbital positions to each other. A divergence limited link with large a large terrestrial telescopic receiver and a larger transmitter size limit geometric loss from becoming an overriding parameter for links up to an Earth-end of the Solar System link.

A comparison of the beam steering tolerances, divergence and geometric loss calculations leads to the following conclusions:

1. For FSO communications links longer than and Earth-to-Satellite range, standard FSO equipment will be unable to overcome geometric losses present in the link.

2. Divergence limited FSO links become limited by geometric losses at distances exceeding Earth-to-Mars links.

3. By limiting divergence and employing large scale (i.e., telescopic or array-based receivers) FSO is a suitable communications method for deep-space communications systems.

4. For FSO links in which a divergence limited system is required (i.e., links exceeding Earth-to-Satellite distances) beam steering tolerances are a limiting factor. For these links, an active optical beam steering system would be required to augment a mechanical gimbal-based alignment system, as well as a method to offset platform vibrations present in the communications system.

3.2.2.1 Divergence and geometric loss for a ground-to-air FSO link

In this section, a more detailed summary of the effects of divergence and geometric losses on a ground-to-air FSO communications link is presented, as this will be the focus of the remaining chapters of this dissertation. The data presented in this section is based on an FSO communications link between a stationary ground terminal and an unmanned aerial vehicle (UAV). Figure 3.6 shows the configuration of the ground-to-UAV FSO link.
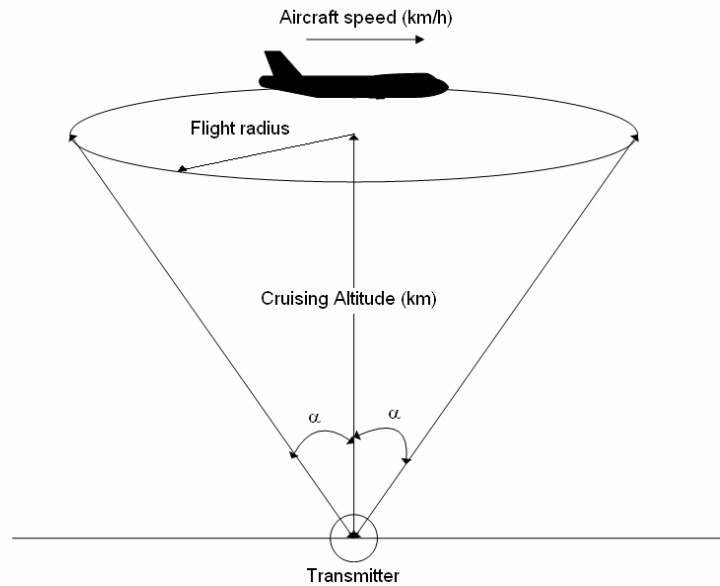
Figure 3.6 Configuration for ground-to-UAV FSO link.

The calculated data for the ground-to-UAV FSO link is based on a UAV flying in a pre-determined circular flight path above a stationary ground station. Calculations were performed in order to determine both the beam diameter expected at the receiver mounted on the UAV and the geometric losses expected for the FSO communications link. The data was calculated for a flight radius of both 4 km and 8 km at an altitude of 4 km above the ground. The resultant beam diameters for the FSO links were found to be 9.9 m and 15.6 m, respectively, which was again based on geometrical divergence calculations. Expected geometric losses of 25.3 dB and 27.3 dB were calculated for the two flight paths, respectively.

Based on the calculated data for beam divergence and geometric loss, it is not expected that either element would prove to be a limiting factor in establishing a ground-to-UAV FSO communications link. The data obtained in this preliminary analytical study will serve as the foundation for the remainder of the work presented in this dissertation.

3.2.3 *Summary of beam steering tolerance and divergence results*

In this section of this dissertation and analytical analysis of beam steering tolerances, beam divergence and geometric loss for various long to ultra-long FSO communications links as well as the expected beam divergence and geometric loss for a ground-to-UAV FSO link, has been presented.

Based on the analytical results, it can be seen that FSO systems are suitable for a large range of communications applications, depending upon the specific transmitter and receiver configurations. When considering beam steering tolerances, beam divergence and geometric losses present in an FSO link, it was found that none of these parameters would prove to be the limiting factor for FSO links up to an Earth-to-satellite link. For longer links, active optical steering is necessary to supplement the mechanical gimbal-based alignment and tracking system.

3.3   Comparison of Active Beam Steering Elements

Following the calculation of the feasibility of various length FSO communications links based on beam steering tolerances, divergences and geometric loss, a study to compare the suitability of different active beam steering elements has been performed.   As part of this study, a computer simulation of the effects of platform vibration for FSO links is presented.

3.3.1 FSO Link Configuration

This section describes the FSO link configuration for the calculations performed in this analysis, as well as the active beam steering elements that will be compared. Figure 3.7 shows the basic FSO link configuration that was used for a comparison of active beam steering elements.   The link consists of a transmitter and receiver pair. The transmitter contains an active beam steering element which can control the direction of the FSO laser beam. The receiver does not contain any active steering element because for this analysis, only a unidirectional flow of data from the transmitter to the receiver is considered. For all links, the transmitter is placed on the remote platform and the receiver is placed at the ground station.
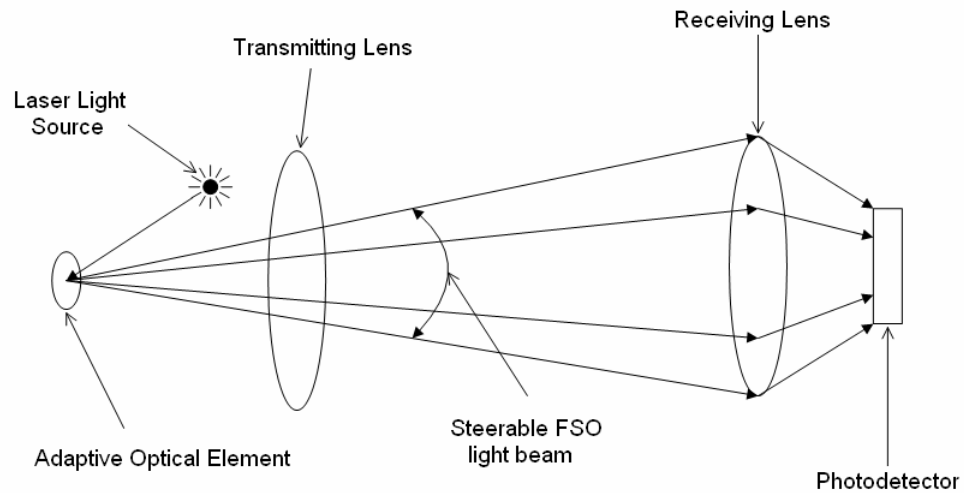
Figure 3.7 FSO link with active beam steering element.

The analysis performed in this study considers six different FSO communications link scenarios. Each scenario considers a different separation distance between the transmitter and the receiver in the FSO communications link. The following scenarios are considered in this study:

1. A 4 *km* FSO communications link between a ground station and a UAV.

2. A 13 *km* FSO communications link between a ground station and a commercial airliner.

3. An FSO communications link between a ground station and a satellite in Earth-orbit at 20,200 *km*.

4. An Earth-Moon FSO communications link of 384,000 *km*.

5. An Earth-Mars FSO communications link at the closest point of orbital separation.

6. A deep-space FSO communications link between Earth and the end of the Solar System.

The beam steering elements considered for construction of a hybrid FSO alignment system are a MEMS-based array of mirrors, an acousto-optic Bragg cell, and a Fast Steering Mirror (FSM).

3.3.2 Results

In this section, the calculated results for the active beam steering components are reported. First, a comparison of the three types of beam steering elements is presented in Section 3.3.2.1. Sec. 3.3.2.2 discusses the simulated effects of mounting platform vibration for the FSO links described in Section 3.3.1. Finally, in Section 3.3.2.3, a simulation run showing the effects of vibration offset using an active beam steering element in a ground-to-UAV FSO communications link is described.

3.3.2.1 Comparison of active beam steering elements

The first beam steering element under consideration was a MEMS-based array of micro mirrors. The MEMS device considered is the DMD 0.7XGA 12° DDR [53]

from Texas Instruments. The DMD 0.7XGA 12° DDR consists of an array of 1024×768 micro-mechanical mirrors. Each mirror in the array can be individually deflected around a diagonal axis to ±12°.

The second beam steering element considered was a FSM. FSM's use linear actuators to drive a 45 mm aperture mirror through a range of ±1° of motion with a resolution of 1 μrad.

The final beam steering element under consideration is an acousto-optic Bragg cell deflector. Acousto-optic deflectors are solid state devices that make use of an acoustic wave to change the angular direction of a laser beam. These devices are further advantageous due to their ability to simultaneously modulate the laser beam. The beam steering comparison here uses an AA.DTS.X-400 acousto-optic deflector / shifter from Quanta-tech [54]. This particular device was chosen due to a large operating wavelength range for single wavelength operation.

Table 3.1 below shows a comparison of the three beam steering elements:

Parameter	MEMS Array	Fast Steering Mirror	Acousto-optic Deflector
Aperture Size	1024×768 mirrors	45 mm	7.5 mm × 7.5 mm
Reflectivity/ Transmission	85%	> 95%	> 95%
Range of beam steering	±12°	±1°	41 – 49 mrad
Resolution	12°	1 μrad	400 dots
Scanning Speed/ Acceleration	9800 patterns/sec	1000 rad/sec^2	10.3μs access time

Table 3.1 Comparison of relevant parameters of beam steering elements.

From the data in Table 3.1, it is possible to eliminate the use of a MEMS device to directly steer the FSO beam due to the limited resolution of the device (it is an on/off device). A comparison of the data for a FSM and an acousto-optic deflector shows that both devices are suitable for active beam steering in FSO applications. FSMs are, however, advantageous over acousto-optic deflectors for several reasons:

1. Larger aperture size.
2. Provides both horizontal and vertical beam steering capabilities with a single device.
3. Greater range of operating wavelengths.

Acousto-optic modulators are able to provide a larger range of beam steering and are further advantageous due to the absence of any mechanical components. They are disadvantageous due to a wavelength dependence on beam steering range and

resolution. The one dimensional beam steering associated with an acousto-optic deflector also means that a pair of acousto-optic deflectors will be required in the FSO transmitter. Also, due to the solid state nature of acousto-optic deflectors, an inherent power threshold exists that if exceeded, will result in the breakdown of the device. Based on this information, the simulation results presented in Section 3.3.2.3 will be performed using a FSM system.

3.3.2.2 Effects of mounting platform vibration on FSO communications links

Vibrations present on FSO mounting platforms mean that some form of active link tracking system is necessary to overcome errors in the beam alignment caused by these vibrations. In this section, simulated results obtained using MATLAB® software are discussed. Simulations were run in order to determine the effects of both vertical and horizontal vibrations at the mounting platform on beam motion at the ground station of the links described in Section 3.3.1.

For both the ground-to-UAV link and the ground-to-commercial aircraft link, a vertical vibration consisting of a sinusoidal vibration combined with a cosinal vibration and a horizontal vibration consisting of a lower frequency sinusoidal vibration combined with a lower frequency cosinal vibration were simulated. While these vibrations do not accurately describe platform motion of the test platforms, little

information relating to platform motion could be located during the literature review process. Figure 3.8 shows a plot of the effects of vibration of a ground-to-UAV FSO link that is 4 *km* in length. The plot shows both the simulated vibrations (in the horizontal and vertical directions) at the UAV and the effect of these vibrations on beam motion at the ground station. The amplitude of the vibrations is of an arbitrary value because the simulation is designed to show the relationship between a vibration at the remote platform and at the ground station. The data on the plot is presented as a function of the angle of alignment between the ground station and the UAV.
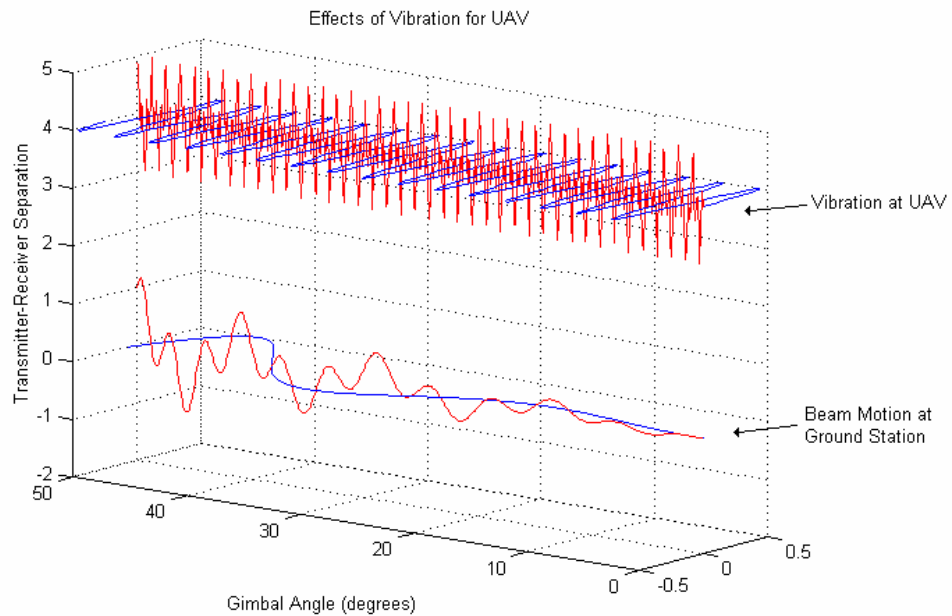
Figure 3.8 Effects of vibration on a ground-to-UAV FSO link.

58

From the figure, it is observed that the amount of beam motion at the ground station increases as the angle of alignment between the ground station and the UAV increases. This is expected and is a result of an increase in transmitter-receiver separation due to the change in alignment angle. Furthermore, it is evident that the vertical vibrations of the UAV have a greater effect on beam motion that the horizontal vibrations of the UAV. It should also be noted that although the effects of vertical vibrations are shown as a vertical misalignment at the receiver, a vertical alignment error at the ground station will also translate into a horizontal misalignment. The smaller amount of beam motion due to the horizontal vibrations of the UAV is due to the lower frequency of the simulated horizontal vibrations. The resultant beam motion at the ground station does, however, show that an active beam steering element will be necessary in order to track a ground-to-UAV FSO communications link.

Figure 3.9 shows the corresponding vibration analysis plot for a 13 *km* ground-to-aircraft FSO link. It can be seen that for the same simulated vibrations for the UAV and higher altitude flight, the beam motion and the ground-station increases for the longer link.
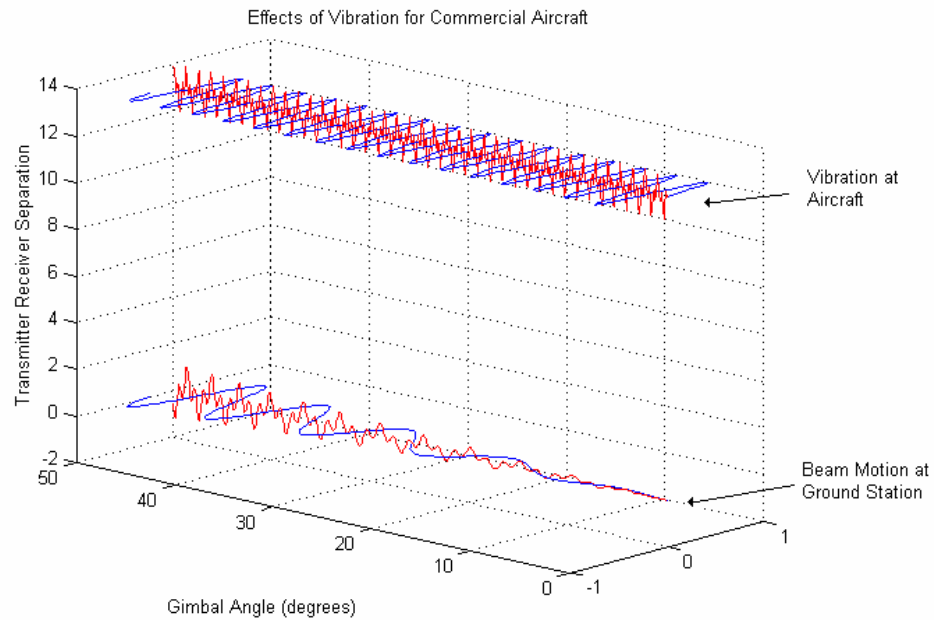
Figure 3.9 Effects of vibration on a ground-to-commercial aircraft FSO link.

Similar to the 4 *km* UAV link, the beam motion present at the ground station of the 13 km ground-to-aircraft FSO link also shows that the motion due to the vertical vibrations causes a greater amount of beam motion than the horizontal vibrations. It is also observed that the increased transmitter-receiver separation has resulted in more erratic beam motion at the ground station terminal. The increased FSO link length has, however, caused the horizontal beam motion at the ground station to become more evident.

For the remaining links described in Section 3.3.1, the vibrations present on the mounting platforms are simulated as sinusoidal vibrations in both the horizontal and

60

vertical directions. This simplification was implemented due to the lack of atmospheric effects for the space-mounted FSO communications platforms.

Figure 3.10 shows a plot of the effects of vibration on beam motion for an Earth-to-satellite FSO link at the ground station of the link. The plot shows the effects in both the horizontal and vertical directions. The plot shows data for (a) a 0° to 50° alignment range and (b) a close-up view of the data for the 40° to 50° alignment angle in order to clearly depict the extent to which a sinusoidal platform vibration causes alignment errors at the ground station.

From the plot it can be seen that an increase in alignment angle causes an increase in beam motion at the ground station terminal of the FSO link. It can also be seen that the sinusoidal vibration does not result in a corresponding sinusoidal beam motion at the receiving end. It is noted from this simulation run that for ultra-long Earth-to-space FSO communications links, platform vibration becomes a major limiting factor in the performance of the link.
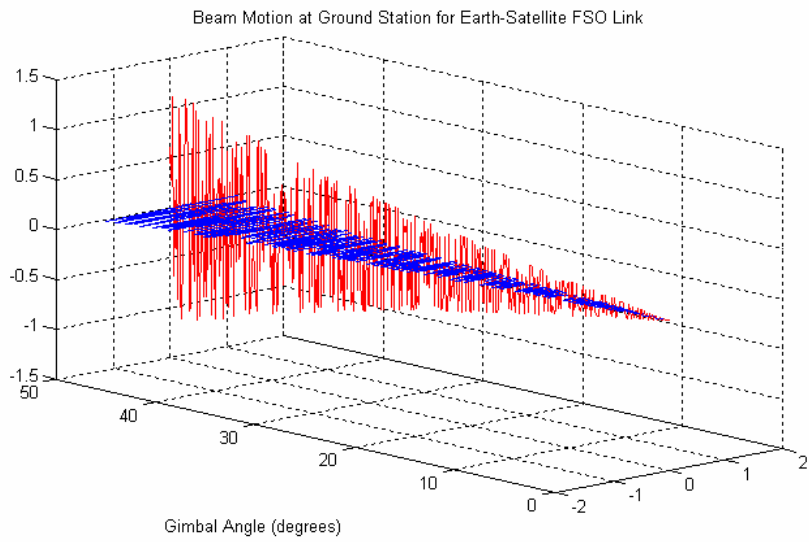
(a)
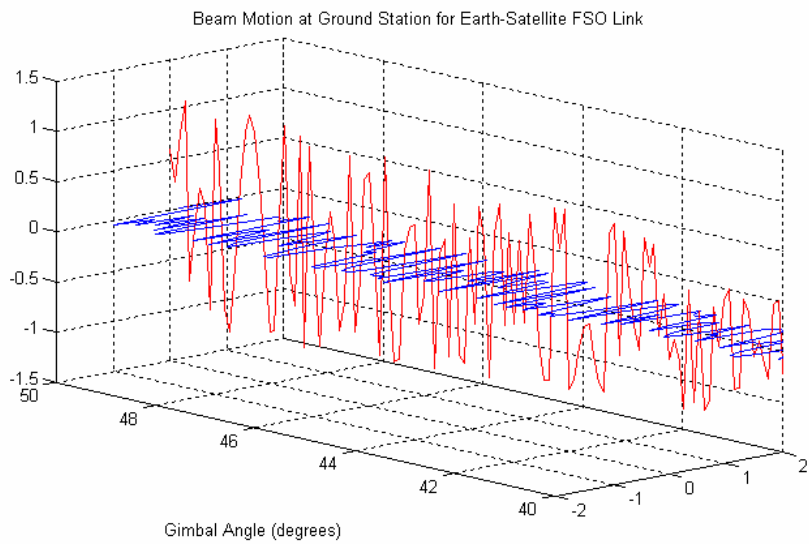
(b)

Figure 3.10 (a) Effects of vibration for an Earth-to-Satellite FSO link and (b) effects of vibration between 40°and 50°.

62

Because both the horizontal and vertical components were simulated using the same sinusoidal vibration, the beam motion present in the system due to these vibrations is the same in both the horizontal and vertical directions. Based on the earlier comparison of active beam steering elements, either an acousto-optic deflector or a FSM-based beam steering mechanism needs to be used to augment a gimbaled alignment system for ultra-long FSO communications links.

Figure 3.11 shows the corresponding results of the vibration simulation for an Earth-to-Moon length FSO communications link. As is expected, the increased transmitter-receiver separation has resulted in an increase in beam motion at the ground station of this communications link.

(a)

Beam Motion at Ground Station for Earth-Moon FSO Link

Gimbal Angle (Degrees)
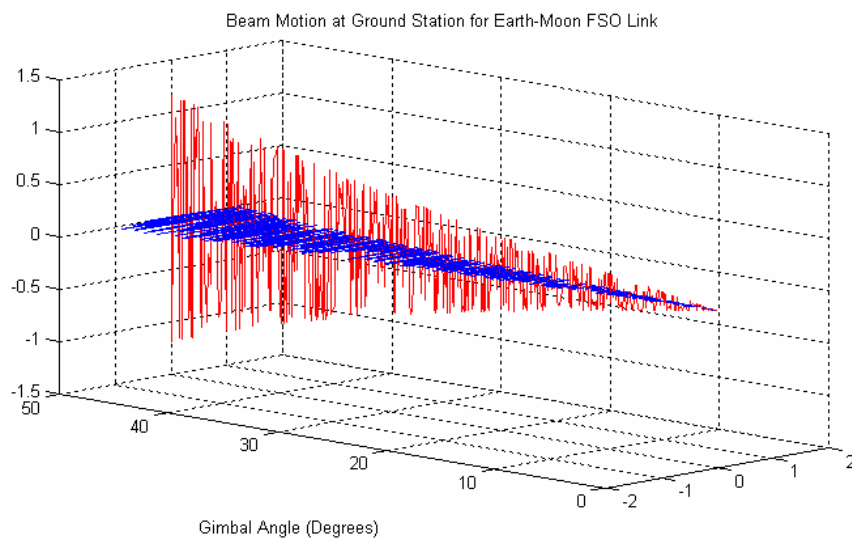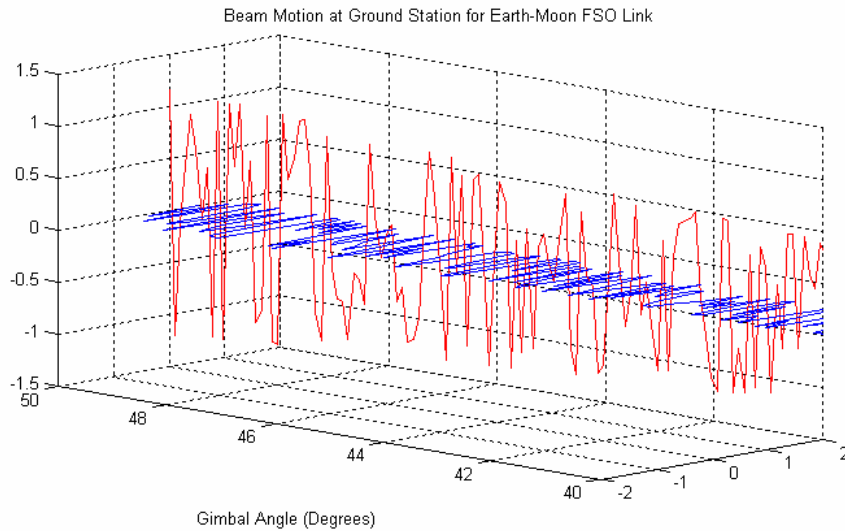
(b)

Figure 3.11 (a) Effects of vibration for an Earth-to-Moon FSO link and (b) effects of

vibration between 40°and 50°.

The effects of vibration for an Earth-to-Mars FSO communications link at the closest

point of orbital separation between the planets is shown in Figure 3.12. The effect of

the platform vibrations on the beam motion at the ground station has further

increased, corresponding to the increased FSO link length. A further complication in

offsetting the effects of vibration is the time delay between light leaving the

transmitter and arriving at the receiver of an ultra-long Earth-to-Mars FSO link. The

effects of vibration combined with the time delay now present in the system means

that a predictive algorithm as well as an active beam steering element is necessary to

offset vibration present in an Earth-to-Mars FSO link.
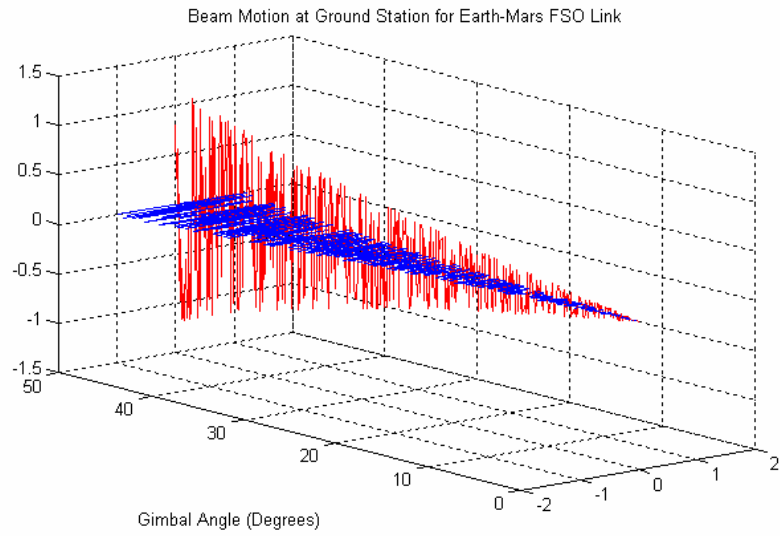
(a)
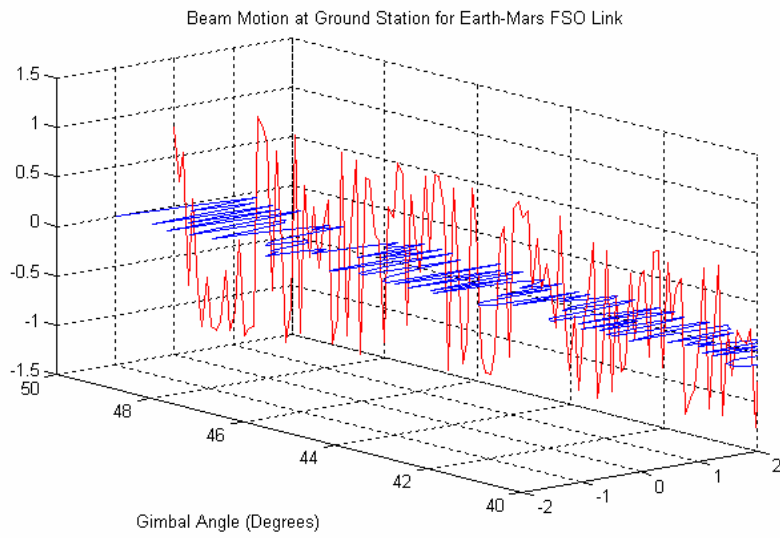
(b)

Figure 3.12 (a) Effects of vibration for an Earth-to-Mars FSO link and (b) effects of vibration between 40°and 50°.

65

Figure 3.13 shows the effects of vibration for an Earth-to-end of Solar System FSO link. This deep-space link between the Earth and the end of the Solar System again shows increased effects of platform vibrations. For deep-space links, it may be necessary to implement vibration control at the remote mounting platform in order to decrease the effects of vibration prior to using an active beam steering element to compensate for the vibrations, in conjunction with a predictive algorithm to allow for the time difference between signal transmission and signal reception.

(a)

66
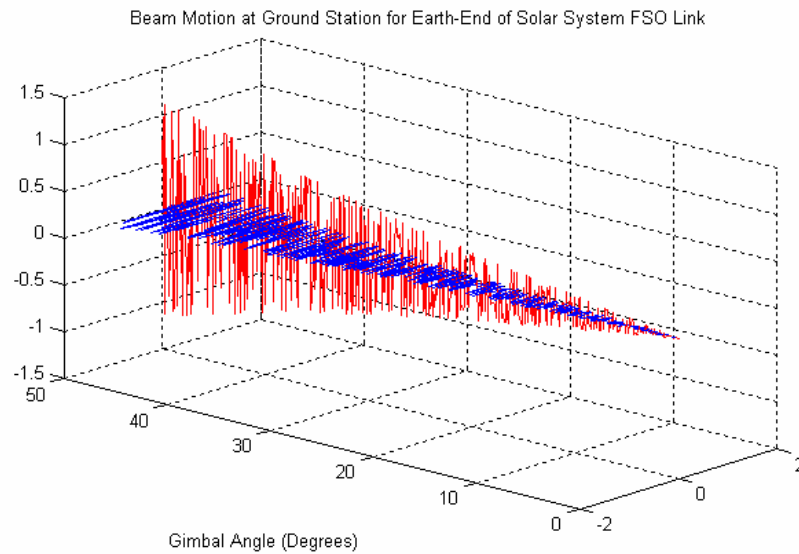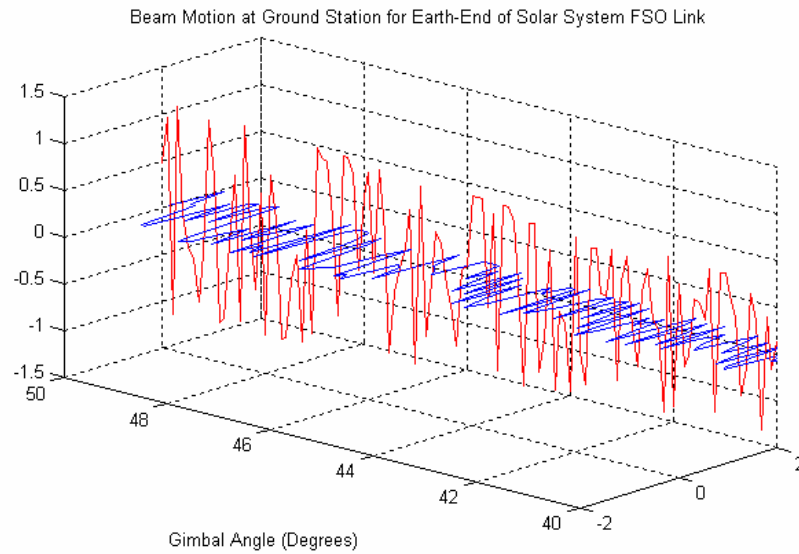
(b)

Figure 3.13 (a) Effects of vibration for an Earth-to-end of Solar System FSO link and

(b) effects of vibration between 40°and 50°.

From the data presented in this section, it can be seen that for all FSO communications links between moving platforms, vibration is a limiting factor in the link performance. For links that are sufficiently long so as to introduce a significant time delay between the transmitter and the receiver, both active beam steering and a predictive algorithm are required in order to compensate for beam motion at the ground station.

67

3.3.3 Simulated effects of vibration offset for ground-to-UAV FSO links

In this section, simulated data showing the ability of a FSM to offset the effects of vibration for a ground-to-UAV FSO communications link is presented. The simulation is based on the inclusion of a time delay between the sensing of a UAV vibration and the adjustment of the FSM for the UAV vibration. Figure 3.14 (a) shows a plot effects of vibration of the UAV on beam motion at the ground station without an a FSM, and Figure 3.14 (b) shows the decreased effects of vibration for a 4 km ground-to-UAV FSO link after the inclusion of a FSM.

(a)

Beam Motion with FSM Vibration Offset
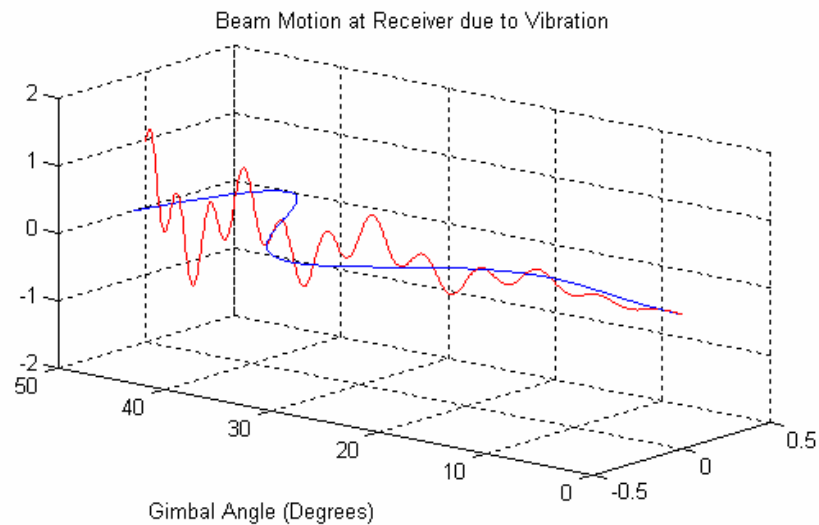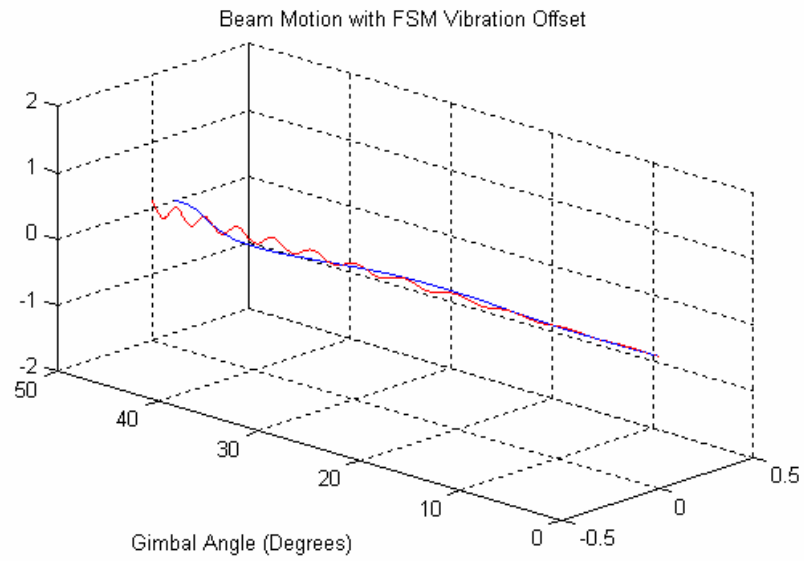
(b)

Figure 3.14 Simulation results showing vibration offset using FSM for ground-to-UAV

FSO link.

As can be seen in the figure, the use of a FSM is able to reduce the effects of platform vibration on the beam motion at the ground station, but because there will always be an inherent time delay between the sensing of a platform vibration and beam alignment adjustment by the FSM, the effects of vibration cannot be completely eliminated.

3.3.4 *Summary of Active Steering Element Comparison and Vibration Analysis*

In this section, a comparison of different active beam steering elements along with a simulation of the effects of mounting platform vibrations of various long to ultra-long FSO communications has been presented. Furthermore, a simulation showing how a FSM can reduce the effects on beam motion due to platform motion has been demonstrated.

Based on the comparison of beam steering elements and the simulated data presented in this section, it can be seen that mounting platform motion greatly affects beam motion at the ground station of an FSO link. Both acousto-optic beam deflectors and FSMs are well-suited for active beam steering in FSO communications links. For FSO links in which the transmitter-receiver separation is large enough to introduce a time delay, both an active steering mechanism and a predictive algorithm will be required in order to offset the effects of vibration.

3.4 Mathematical Model of a Ground-to-UAV FSO Link

In this section, a mathematical model of a ground-to-UAV link will be described. Figure 3.15 shows a schematic view of a ground-to-UAV FSO communications that will be used to create a model of the communications link.
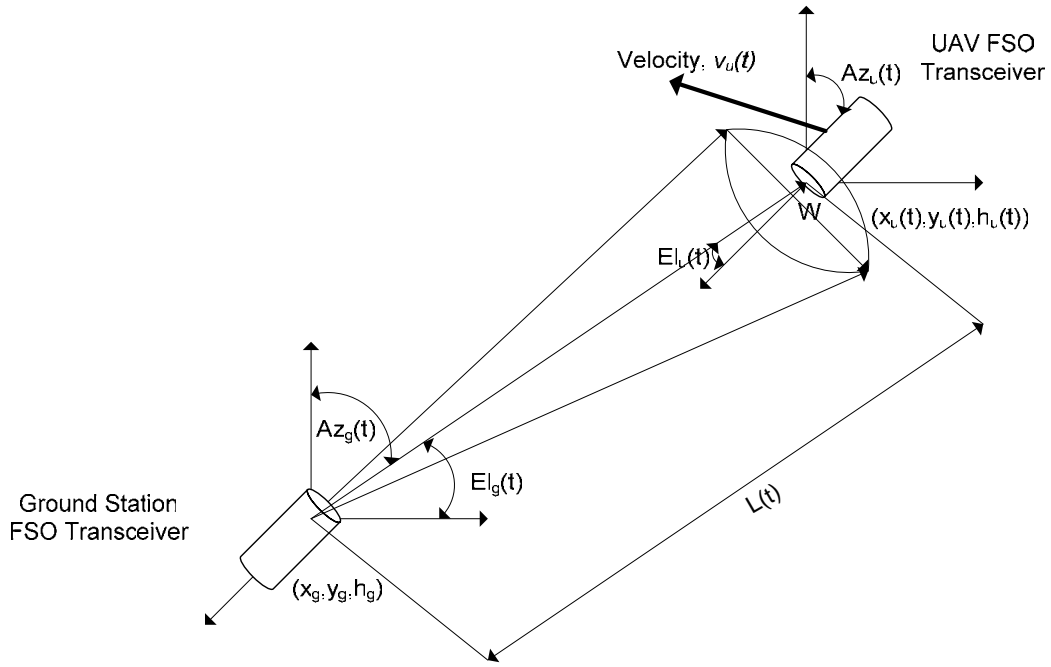
Figure 3.15 Ground-to-UAV FSO link for mathematical model.

On the figure, the following parameters are defined. The separation between the ground station and the UAV is of length, $L(t)$, where $L(t)$ is measured in *km*. The ground station transceiver is located at (x_g, y_g, h_g), where x_g, y_g and h_g are the coordinates of the ground station position and altitude. Similarly, the UAV is located at $(x_u(t), y_u(t), h_u(t))$, where $x_u(t)$, $y_u(t)$ and $h_u(t)$ are the coordinates of the UAV position and altitude. The UAV is on fixed flight path, with its instantaneous velocity given by $v_u(t)$. The ground station is a stationary platform, with no motion present. In the receiver plane of the UAV, the spot size of the FSO laser beam is given by $W(t)$. The ground station gimbal has an elevation, $El_g(t)$ and an azimuth, $Az_g(t)$. Similarly, the UAV gimbal has and elevation, $El_u(t)$ and azimuth, $Az_u(t)$.

Based on the definitions provided above, the first parameter that can be calculated is the path length, $L(t)$. The instantaneous value of $L(t)$ at any given moment is given by:

$$L(t) = \sqrt{(x_u(t) - x_g)^2 + (y_u(t) - y_g)^2 + (h_u(t) - h_g)^2} \ . \qquad (3.1)$$

However, the values of $x_u(t)$, $y_u(t)$ and $h_u(t)$ are continually changing as the UAV follows its flight path. From the velocity of the UAV, it therefore follows that the position of the UAV is given by:

$$
\begin{aligned}
x_u(t) &= x_u(0) + v_{xu}(t) + \frac{1}{2} a_{xu}(t) t^2, \\
y_u(t) &= y_u(0) + v_{yu}(t) + \frac{1}{2} a_{yu}(t) t, \, and \\
h_u(t) &= h_u(0) + v_{hu}(t) + \frac{1}{2} a_{hu}(t) t
\end{aligned}
\qquad (3.2)
$$

where $x_u(0)$, $y_u(0)$ and $h_u(0)$ are the initial position of the UAV, $v_{xu}(t)$, $v_{yu}(t)$ and $v_{hu}(t)$ are the x, y and h components of the UAV velocity, respectively. Similarly, $a_{xu}(t)$, $a_{yu}(t)$ and $a_{hu}(t)$ are the x, y and h components of the UAV acceleration, respectively. Substituting Equation (3.2) into Equation (3.1) gives the resultant instantaneous transmitter receiver separation of the ground station and the UAV as

$$L(t) = \sqrt{\left(x_u(0) + v_{xu}(t) + \frac{1}{2}a_{xu}(t)t^2 - x_g\right)^2 + \left(y_u(0) + v_{yu}(t) + \frac{1}{2}a_{yu}(t)t^2 - y_g\right)^2 + \left(h_u(0) + v_{hu}(t) + \frac{1}{2}a_{hu}(t)t^2 - h_g\right)^2}$$

(3.3)

Assuming that the UAV is programmed to fly at a fixed velocity, the acceleration in each direction would be zero, so Equation (3.3) simplifies to

$$L(t) = \sqrt{\left(x_u(0) + v_{xu}(t) - x_g\right)^2 + \left(y_u(0) + v_{yu}(t) - y_g\right)^2 + \left(h_u(0) + v_{hu}(t) - h_g\right)^2} \qquad (3.4)$$

Equation (3.4) now defines the transmitter-receiver separation of the FSO link as a function of time. This value will later be use to model the divergence present in the FSO link. The next value calculated is the elevation as viewed from the ground station to the UAV, $El_g(t)$.

$$El_g(t) = \tan^{-1}\left(\frac{h_u(t) - h_g}{\sqrt{\left(x_u(t) - x_g\right)^2 + \left(y_u(t) - y_g\right)^2}}\right). \qquad (3.5)$$

Once again, substituting in the values from Equation (3.2) with zero acceleration gives

$$El_g(t) = \tan^{-1}\left(\frac{h_u(0) + v_{hu}(t) - h_g}{\sqrt{\left(x_u(0) + v_{xu}(t) - x_g\right)^2 + \left(y_u(0) + v_{yu} - y_g\right)^2}}\right). \qquad (3.6)$$

Using the same logic, the azimuth from the ground station to the UAV is calculated to be

$$Az_g(t) = \tan^{-1}\left(\frac{y_u(0)+v_{yu}(t)-y_g(t)}{x_u(0)+v_{xu}(t)-x_t(t)}\right). \tag{3.7}$$

Similarly the elevation and azimuth from the UAV to the ground station can be calculated to be

$$El_u(t) = 180° - \tan^{-1}\left(\frac{h_u(0)+v_{hu}(t)-h_g}{\sqrt{\left(x_u(0)+v_{xu}(t)-x_g\right)^2+\left(y_u(0)+v_{yu}-y_g\right)^2}}\right), \tag{3.8}$$

and

$$Az_u(t) = 180° - \tan^{-1}\left(\frac{y_u(0)+v_{yu}(t)-y_g(t)}{x_u(0)+v_{xu}(t)-x_t(t)}\right), \tag{3.9}$$

respectively. The final parameter to be calculated in this mathematical model is the beam divergence at the receiver plane of the UAV. In order to calculate the effective spot size of the FSO laser beam at the receiver plane of the UAV, consider the propagation of a lowest order transverse electromagnetic Gaussian-beam wave. This is expressed as

74

$$U_0(\vec{r},0) = A_0 e^{\left(-\frac{r^2}{W_0^2} - i\frac{kr^2}{2F_0}\right)}, \tag{3.10}$$

where A_0 is the amplitude of the wave, r is the distance from the center line in the transverse direction, $i^2 = -1$, W_0 is the effective beam radius, F_0 is the parabolic radius of curvature of the phase distribution and k is the optical wave number. Setting

$$\alpha_0 = \frac{2}{kW_0^2} + i\frac{1}{F_0}, \tag{3.11}$$

Equation (3.10) becomes

$$U_0(\vec{r},L) = A_0 e^{\left(-\frac{1}{2}\alpha_0 kr^2\right)}. \tag{3.12}$$

The optical field of the Gaussian-beam wave at a distance L is given by the Huygens-Fresnel integral [55,56]

$$U_0(\vec{r},L) = -2ik \int\int_{-\infty}^{\infty} G(\vec{s},\vec{r};L)U_0(\vec{s},0)d^2s, \tag{3.13}$$

where $U_0(\vec{s},0)$ is the optical field at the ground station transmitter plane and $G(\vec{s},\vec{r};L)$ is Green's function which is defined by

$$G(\vec{s},\vec{r};L) = \frac{1}{4\pi L} e^{\left[ikL + \frac{ik}{2L}|\vec{s}-\vec{r}|\right]}.$$ (3.14)

Substituting Equation (3.12) into Equation (3.13) and evaluating the integrals, a Gaussian-beam wave with complex amplitude $A_0/(1+i\alpha_0 L)$ is obtained:

$$U_0(\vec{r},L) = \frac{A_0}{1+i\alpha_0 L} e^{\left[ikL - \frac{1}{2}\left(\frac{\alpha_0 kr^2}{1+i\alpha_0 L}\right)\right]},$$ (3.15)

where $1+i\alpha_0 L$ is referred to as the propagation parameter [56]. In order to express Equation (3.15) in terms of beam radius, the following notation is defined:

$$\begin{aligned} \Theta_0 &= \mathrm{Re}(1+i\alpha_0 L) = 1 - \frac{L}{F_0} \\ \Lambda_0 &= \mathrm{Im}(1+i\alpha_0 L) = \frac{2L}{kW_0^2} \end{aligned}.$$ (3.16)

The parameter Θ_0 describes the amplitude change in the wave due to focusing and Λ_0 describes the corresponding change due to diffraction. Substituting this notation, Equation (3.15) becomes

$$U_0(\vec{r}, L) = \frac{A_0}{\Theta_0 + i\Lambda_0} e^{\left(ikL - \frac{r^2}{W^2} - i\frac{kr^2}{2F}\right)} \tag{3.17}$$

$$= \frac{A_0 e^{-r^2/W^2}}{\left(\Theta_0^2 + \Lambda_0^2\right)^{1/2}} e^{\left(ikL - i\tan^{-1}\frac{\Lambda_0}{\Theta_0} - i\frac{kr^2}{2F}\right)},$$

where the term $A_0/\left(\Theta_0^2 + \Lambda_0^2\right)^{1/2}$ represents the amplitude changes due to both focusing

and diffraction an $\tan^{-1}(\Lambda_0/\Theta_0)$ is the longitudinal phase shift. Performing a statistical

analysis of a Gaussian-beam wave does not require the algebraic complexity of the

beam parameters defined in Equation (3.16) [30]. It is therefore possible to use the

transformation $1/(\Lambda_0/\Theta_0) = \Theta - i\Lambda$ where

$$\Theta = \frac{\Theta_0}{\Theta_0^2 + \Lambda_0^2}, \Lambda = \frac{\Lambda_0}{\Theta_0^2 + \Lambda_0^2}, \tag{3.18}$$

where Θ and Λ are the receiver beam parameters. The beam radius, W and the phase

front curvature F at the receiver have been shown to be [56]

$$\Theta = 1 + \frac{L}{F}, \Lambda = \frac{2L}{kW^2} . \tag{3.19}$$

Using these values, the beam radius at the receiver plane of the UAV can be

expressed as

$$W = W_0\left(\Theta_0^2 + \Lambda_0^2\right)^{\frac{1}{2}} = \frac{W_0}{\left(\Theta^2 + \Lambda^2\right)^{\frac{1}{2}}}. \tag{3.20}$$

Using the value for $L(t)$ from Equation (3.1), the beam radius in the receiver plane of the UAV as the gimbals rotate can be expressed as

$$W(t) = W_0\left[\left(1 - \frac{\sqrt{\left(x_u(t) - x_g\right)^2 + \left(y_u(t) - y_g\right)^2 + \left(h_u(t) - h_g\right)^2}}{F_0}\right) + \left(\frac{2\left(\sqrt{\left(x_u(t) - x_g\right)^2 + \left(y_u(t) - y_g\right)^2 + \left(h_u(t) - h_g\right)^2}\right)}{kW_0}\right)\right]^{\frac{1}{2}}$$

$$\tag{3.21}$$

Finally, the Gaussian-beam wave at the receiver can be expressed as

$$U_0\left(\vec{r}, L\right) = A_0\left(\Theta - i\Lambda\right)e^{\left(ikL - \frac{r^2}{W^2} - i\frac{kr^2}{2F}\right)}. \tag{3.22}$$

A substitution of Equations (3.1), (3.19) and (3.21) into Equation (3.22) would give a time varying Gaussian-beam equation in the receiver plane of the UAV as the gimbals rotate and track each other.

3.5 Summary

This chapter has introduced a feasibility study used to determine the suitability of FSO technology in order to provide a high-bandwidth communications channel between different remote mobile platforms and a ground station. Furthermore, a mathematical model of important parameters between the ground station and UAV has been described.

This preliminary study has shown that FSO technology is a possible solution for the provision of communications links between objects with transmitter-receiver separations ranging from terrestrial links to deep-space communications links. While the provision of a communications channel to such a multitude of different applications is of great interest, such a study is beyond the scope of this dissertation. For this reason, the remainder of this dissertation will focus on the use of FSO systems to provide a high-bandwidth communications channel between a ground station and an unmanned aerial vehicle.

Chapter 4

Gimbal Classification and Beam Steering in the

Presence of Atmospheric Turbulence

4.1 Introduction

This chapter experimentally characterizes the capabilities of a mechanical gimbal for use in a ground-to-UAV FSO communications link and uses simulation techniques to assess the beam steering tolerance of the FSO laser beam in the presence of atmospheric turbulence. Both the repeatability and accuracy of the gimbal are measured in order to verify that a ground-to-UAV FSO communications link can be aligned and tracked. Through the use of simulation tools, the amount of divergence in the FSO communications link can be determined. The divergence present will allow for a comparison between the beam size at the UAV and the error present in the FSO link due to gimbal pointing error, which is a vital parameter in order to maintain a continuous connection between the FSO transmitter and receiver.

The remainder of this chapter is organized as follows: Section 4.2 describes the experimental configuration of the gimbal repeatability and accuracy experiment as well as the simulation configuration and input parameters used to determine the beam size at the UAV and the expected scintillation index of the link. Section 4.3 contains

the experimental results obtained along with the simulation results and a geometric loss analysis for the FSO link. A summary of the results is presented in Section 4.4.

4.2   Experimental Setup

This chapter includes both an experimental portion for measuring the accuracy and repeatability of the mechanical gimbal and a simulation portion in order to determine the divergence of the FSO laser beam in the presence of atmospheric turbulence, which is also used to more accurately predict the amount of geometric turbulence expected in a ground-to-UAV FSO communications link. Both the experimental and simulation configurations are described in this section.

4.2.1 Gimbal Experimental Setup

The experimental configuration used to determine the accuracy and repeatability of the mechanical gimbal is illustrated in Figure 4.1 below.
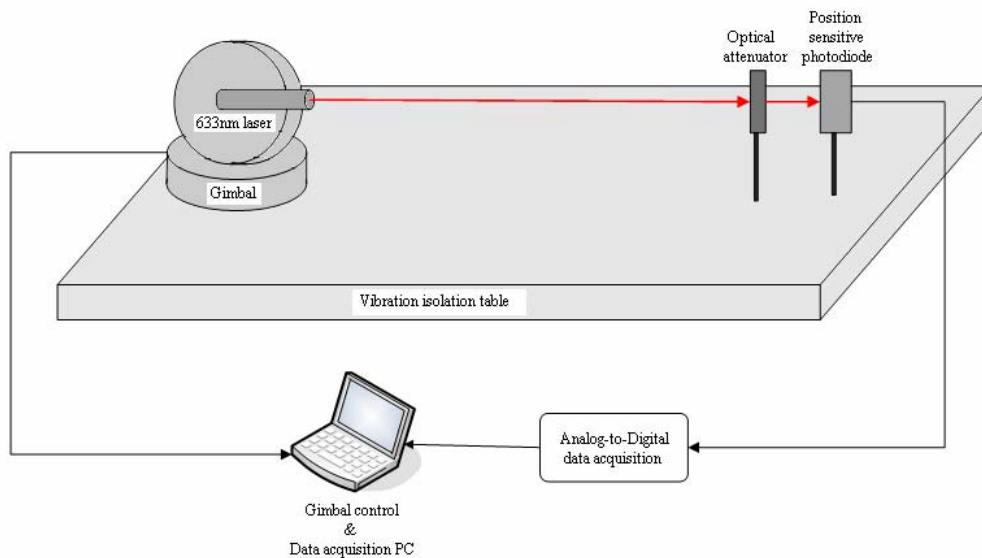
Figure 4.1 Gimbal repeatability and accuracy experimental configuration.

An optical vibration isolation table was used as the base for the gimbal repeatability and accuracy experiments. The optical table allows for the gimbal to be secured to the table and eliminates any gimbal motion that occurs due to torque produced during the experimental trials. A 633 *nm* helium-neon laser was mounted onto a Sagebrush Technology Model-20 Pan and Tilt gimbal using optical mounts.

The Model-20 Pan and Tilt gimbal is a servo-based gimbal with a position resolution of 0.004°. Based on the resolution specified by the gimbal manufacturer, a device with a high resolution is required to measure the gimbal's accuracy. For this reason, a DL-100-7PCBA X, Y duo-lateral position sensing photodiode (PSD) with preamplifier circuitry from Pacific Silicon Sensor Incorporated was used. The DL-100-7PCBA has a 10 *mm* × 10 *mm* active area with a bias resolution greater than 0.25

µm and a bias dependent linearity of ±1% of full scale. The maximum input light intensity supported by the PSD is 1.5 *W/cm²*. The PSD preamplifier circuitry outputs bipolar voltage analogs of the X and Y position of the laser spot centroid as well as the total X and Y currents which are used to externally normalize the outputs in order to eliminate dependence of the PSD on light intensity.

Data from the PSD was acquired using a PMD-16008FS USB-based data acquisition module from Measurement Computing. The PMD-16008FS has eight channels of simultaneous 16-bit analog input, four of which were used for the gimbal repeatability and accuracy experiment. Both the data acquisition software and the gimbal control software were implemented on the same control computer and were programmed in Visual Basic .NET. The data acquisition and gimbal control programs were synchronized to each other using the control computer's internal clock.

The laser mounted on the gimbal was placed a distance of 1.77 *m* from the PSD and an optical attenuator was placed on the light path. The distance selected was the largest achievable separation between the light source and the PSD possible on the optical table. The optical output power of the HeNe laser was measured to be 240.90 *µW* in the plane of the PSD and was reduced to 190.15 *µW* by the optical attenuator in order to assure that the maximum light intensity threshold of the PSD was not exceeded. Ten programmed movements were sent sequentially from the control

computer to the gimbal through the control computer's RS-232 serial port. The laser beam position on the PSD was recorded when the gimbal was aligned to an azimuth and elevation of zero. A total of 14,000 data points were recorded for the gimbal repeatability and accuracy experiments. Figures 4.2 through 4.5 show detailed photographic views of the experimental setup.

Figure 4.2 Gimbal repeatability and accuracy experimental setup viewed from behind the gimbal towards the PSD.

Figure 4.3 Helium-neon laser mounted on Model-20 Pan and Tilt gimbal.

Figure 4.4 Control computer and PMD-16008FS data acquisition device.
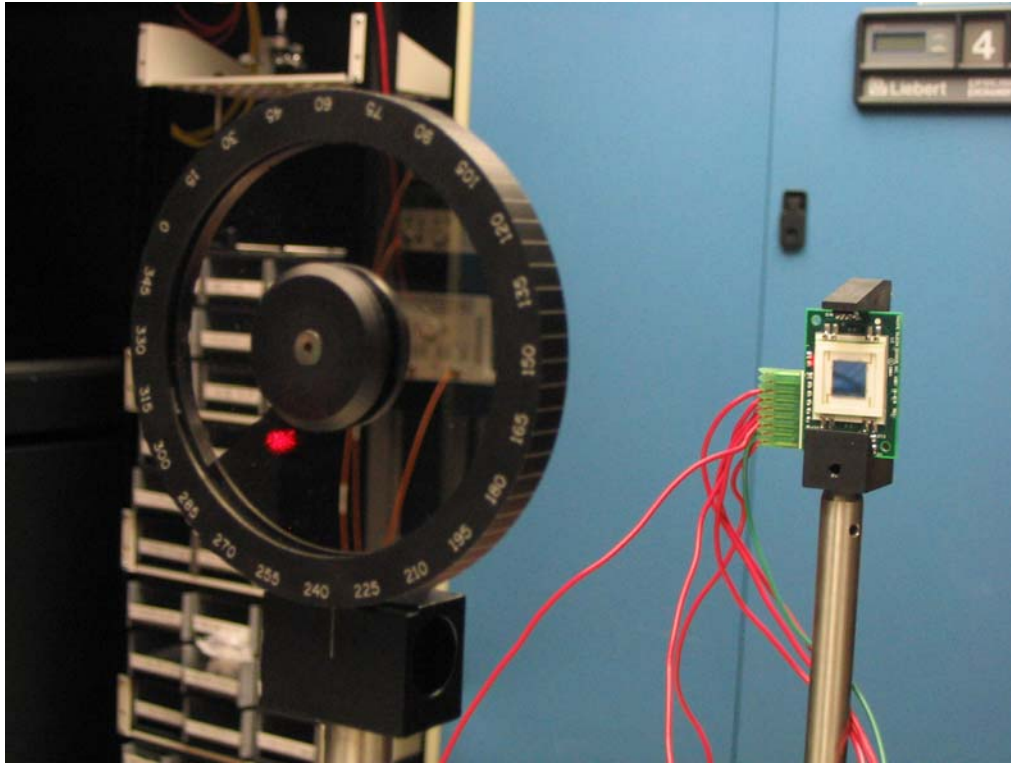
Figure 4.5 Optical attenuator and DL-100-7PCBA PSD.

4.2.2 Simulation Configuration

The simulation was run in order to determine the divergence of the laser beam in the FSO link in the presence of atmospheric turbulence. The simulations were run using Atmospheric Laser Turbulence Model (ALTM) software from ONTAR Corporation. The ALTM software uses experimentally-verified mathematical models to calculate various beam characteristics in the presence of atmospheric turbulence [57]. Figure 4.6 depicts the scenario for which the simulation was configured.
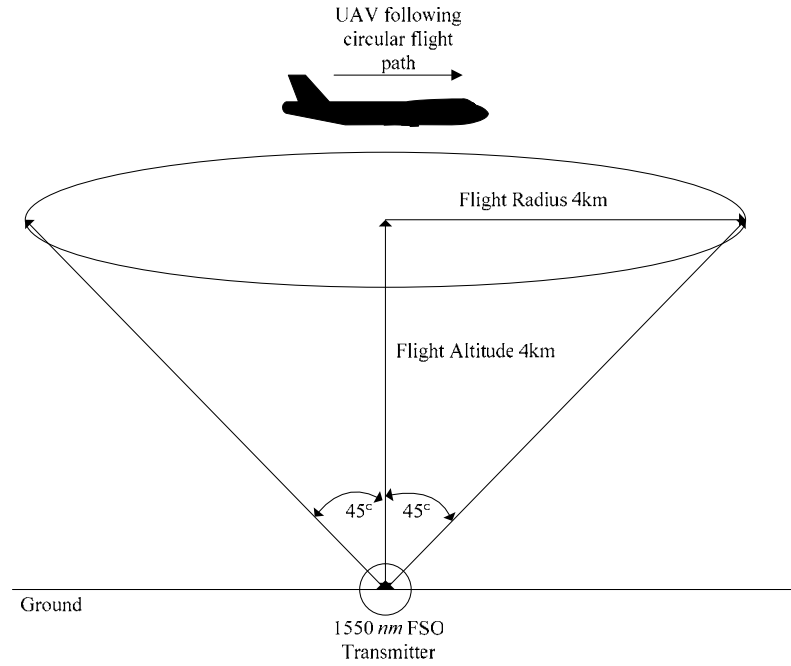
Figure 4.6 Ground-to-UAV FSO link configuration.

This chapter considers a link situation in which the UAV is following a pre-determined circular flight path of radius 4 *km* at an altitude of 4 *km*. This flight configuration results in a gimbal elevation of 45° from horizontal and a transmitter-receiver separation of 5.66 *km*.

The output from the transmitter used in the simulation was a 20 *mW* laser beam with a wavelength of 1550 *nm*. The simulation software requires an input of the transmitter beam profile, $2W_0$, where W_0 is given by [55]:

$$U_0(r,0) = a_0 \exp\left(-r\frac{r^2}{W_0^2} - \frac{ikr^2}{2F_0}\right), \qquad (4.1)$$

87

where $U_0(r,0)$ is the complex amplitude of the wave, a_0 is the amplitude of the wave on the optical axis, F_0 is the radius of curvature of an assumed parabolic distribution of the phase, r is the distance from the beam center line in the transverse direction, k is the optical wave number and α is a complex parameter related to spot size and phase front radius of curvature given by [55]:

$$\alpha = \frac{2}{kW_0^2} + i\frac{1}{F_0} \ .$$ (4.2)

For the results obtained in this simulation, a value of 0.3 *cm* was used for $2W_0$. The simulation software requires an input value for the half-angle divergence in order to calculate the beam spread of the FSO communications link. The half-angle divergence of the beam wave is defined as:

$$div = -\frac{W_0}{F_0} ,$$ (4.3)

where F_0 is the phase front radius of curvature of the beam. The half-angle divergence used to obtain the simulation results presented here was 0.05° (872.66 *μrad*), which was chosen based on divergence figures for commercially developed FSO systems.

The atmospheric parameters used to perform the calculations are also required by the simulation software. The first atmospheric parameters required are the inner scale, l_0, and the outer scale, L_0. The inner and outer scales are present when the atmosphere is conceptualized as eddies created due to local unstable air masses. The inner scale represents the smallest scale of these eddies, on the order of a few millimeters, and the outer scale represents the largest scale in this inertial range, on the order of a meter or so. For the simulation results presented in this investigation, the inner scale was set to 5 *mm* and the outer scale to 1 *m*, which are considered to be typical values for normal turbulence.

The final atmospheric parameter required is the atmospheric structure parameter, C_n^2, which is given by [56]:

$$C_n^2 = \left(79 \times 10^{-6} \frac{P}{T^2} \right)^2 C_T^2,$$ (4.4)

where P is the pressure in millibars, T is the temperature in Kelvin and C_T^2 is the temperature structure constant. The value selected for C_n^2 was 7.5×10^{-15} $m^{-2/3}$ which is approximately the midpoint between "weak turbulence" and "strong turbulence". The configuration of the receiver in the FSO link consisted of a lens with a 30 *cm* aperture and a 20 *cm* focal length. The receiver threshold was set to 30 *dB* below the

89

mean. The noise bandwidth of the atmosphere was 550 *Hz* which is considered to be a typical value.

4.3   Experimental Results

In this section, the experimental results for the gimbal accuracy and repeatability measurements and the atmospheric turbulence simulations are reported. In Section 4.3.1, the experimental results along with their associated distributions are discussed. Section 4.3.2 discusses the beam divergence simulated results associated with the ground-to-UAV FSO link, and the Section 4.3.3 discusses how the amount of beam divergence affects the gimbal's steering tolerances for this application along with the expected geometric losses from the configuration.

4.3.1 Gimbal Repeatability and Error

Gimbal repeatability and accuracy are important factors in the development of a ground-to-UAV FSO communications system. In order to align such an FSO link, the ability of the gimbal to return accurately to a specified azimuth and elevation is required. A detailed analysis of the gimbal's repeatability allows for the error distribution associated with the gimbal performing the link alignment to be included in the alignment and tracking algorithm.

Figure 4.7 shows an X-Y scatter plot of the data recorded for the gimbal repeatability experiment. From the plot, it can be observed that the gimbal repeatability fell in an area approximately 0.5 mm^2. A complete data set for the gimbal repeatability experiment is available in Appendix A.
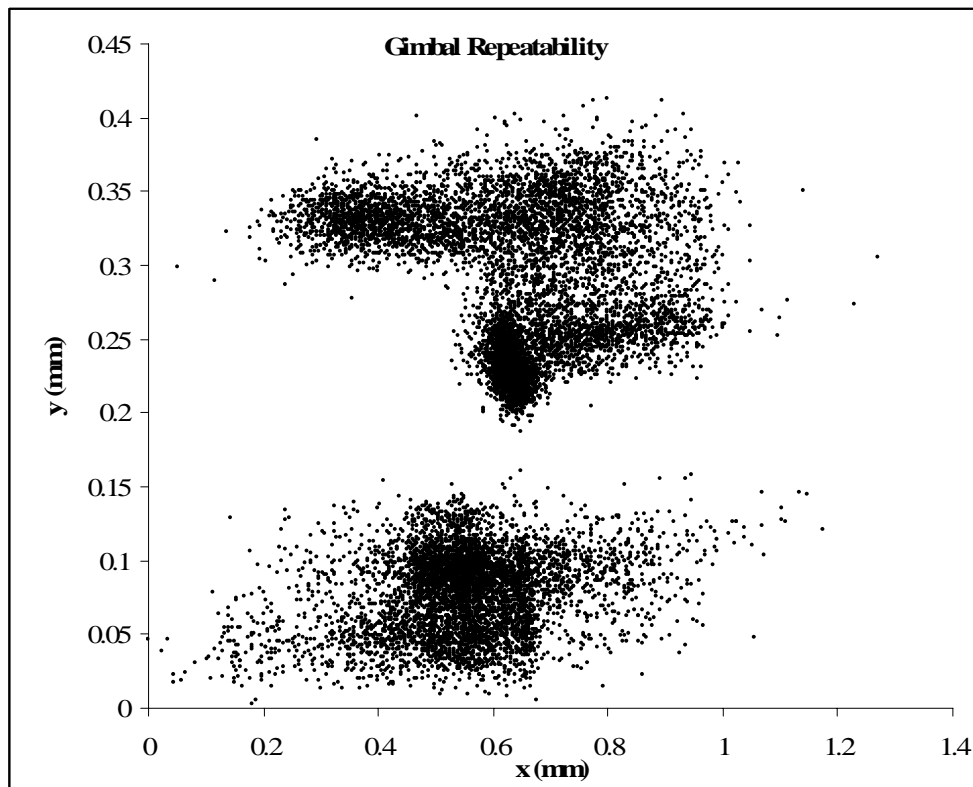
Figure 4.7 X-Y scatter plot of gimbal repeatability data.

Figure 4.8 shows an X-Y scatter plot of the gimbal error for the 14,000 experimental trials. Figure 4.9 shows the corresponding plot for the first 100 data points. Based on the output plot of the raw error analysis data, the gimbal error is concentrated in a

range between 0 *mm* and 0.2 *mm*. A complete data set for the gimbal accuracy experiment is available in Appendix A.
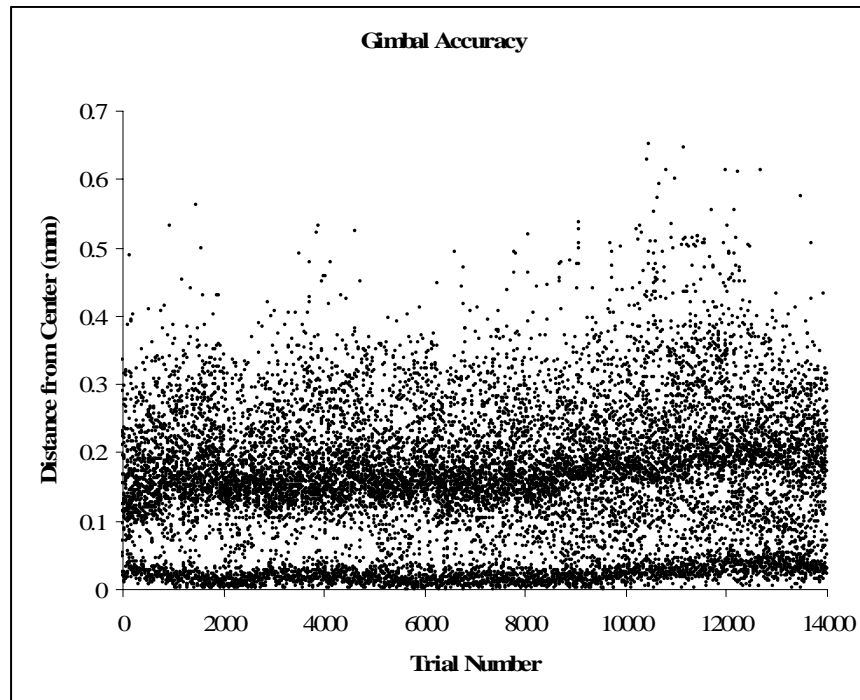
Figure 4.8 X-Y scatter plot of gimbal accuracy data.
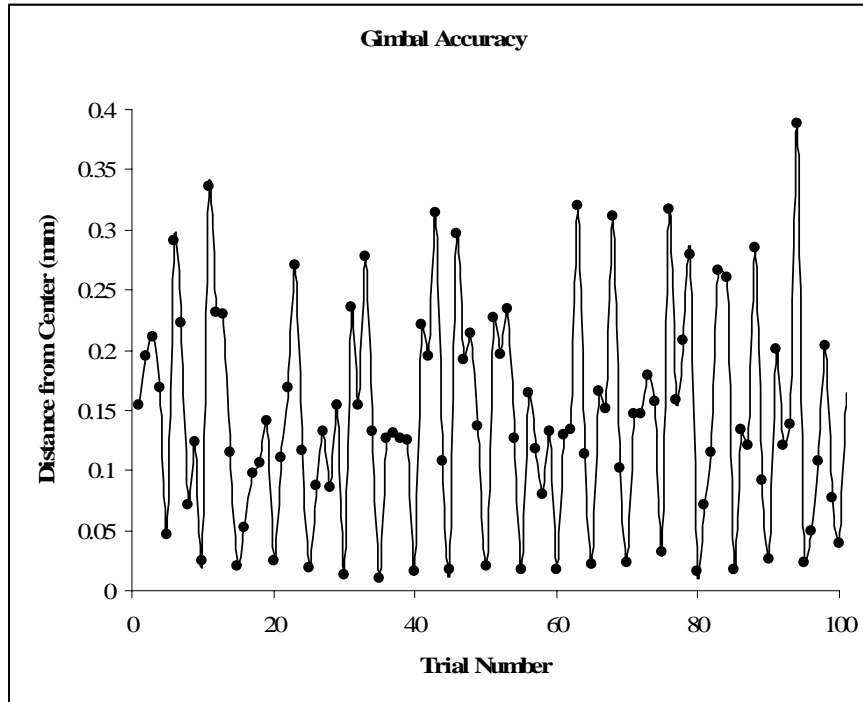
Figure 4.9 X-Y scatter plot of first 100 accuracy data points.

The remainder of this section is used to analyze the distributions associated with the experimental measurements reported. The data was analyzed using a normal distribution in which the probability density function (PDF) is given by:

$$PDF = \frac{1}{\sigma\sqrt{2\pi}}\exp\left(-\frac{(x-\mu)^2}{2\sigma^2}\right), \qquad (4.5)$$

where μ is the mean, σ is the mean and σ^2 is the variance of the experimental data.

93

Figure 4.10 shows the PDF for the azimuth repeatability expected at the UAV measured in meters. The azimuth of the gimbal was found to have a repeatability mean of 1.24 *m* with a standard deviation of 0.2 *m*. Figure 4.11 shows the corresponding PDF translated into an azimuth angle. When viewed as an angle, the azimuth repeatability mean was found to be 0.013° (226.89 *μrad*) with a standard deviation of 0.003° (52.36 *μrad*).
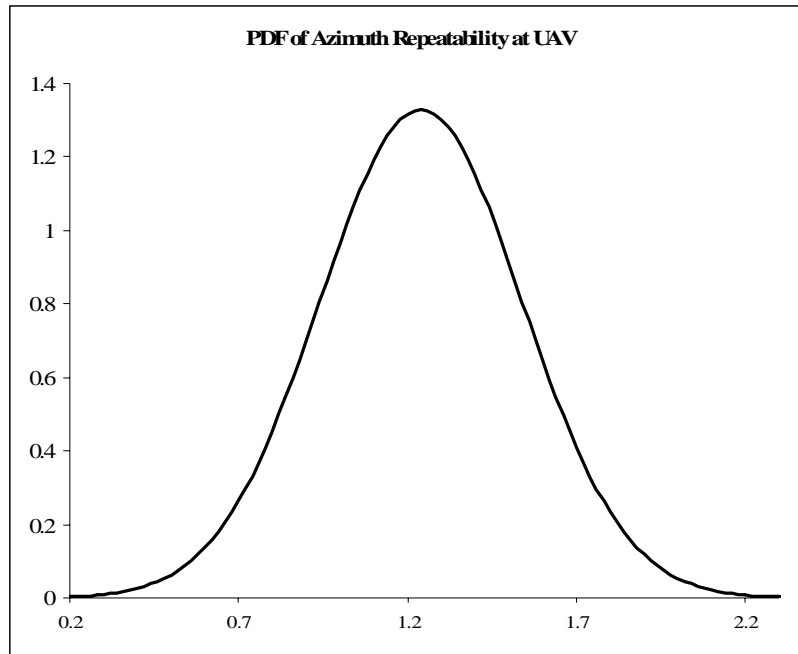
Figure 4.10 Distribution of azimuth repeatability at UAV in meters.
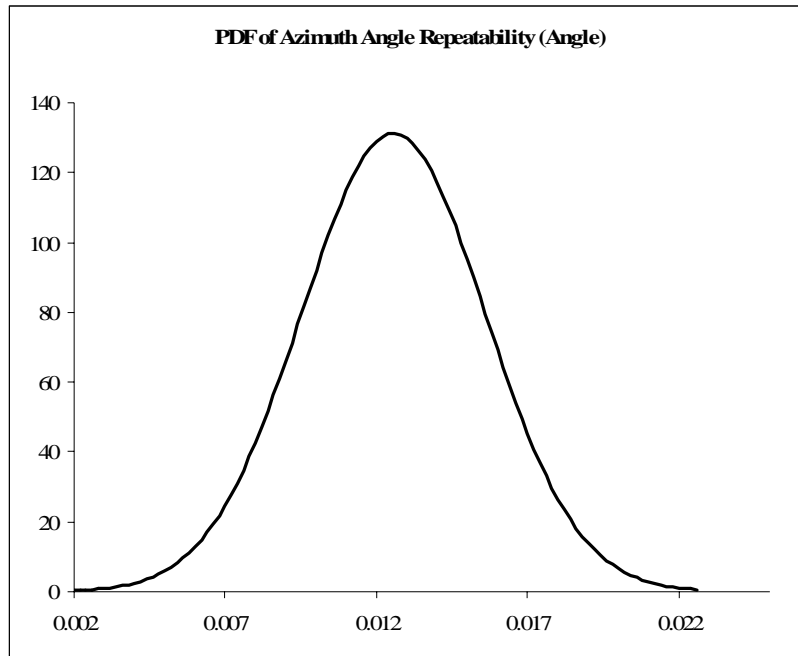
Figure 4.11 Distribution of azimuth repeatability at UAV in degrees.

The PDF for the elevation repeatability of the gimbal at the UAV measured in meters is shown in Figure 4.12. The gimbal elevation repeatability was measured to be 0.41 *m* with a standard deviation of 0.22 *m*. Figure 4.13 shows the corresponding PDF converted into an elevation angle. The gimbal elevation repeatability was measured to have a mean of 0.004° (69.81 *μrad*) with a standard deviation of 0.002° (39.91 *μrad*). The data for the azimuth and elevation repeatability experiments showed that the gimbal repeatability was measured to be 3.25 times more accurate with respect to elevation. However, the difference in accuracy of the elevation and repeatability is not as significant a concern as the overall gimbal accuracy.
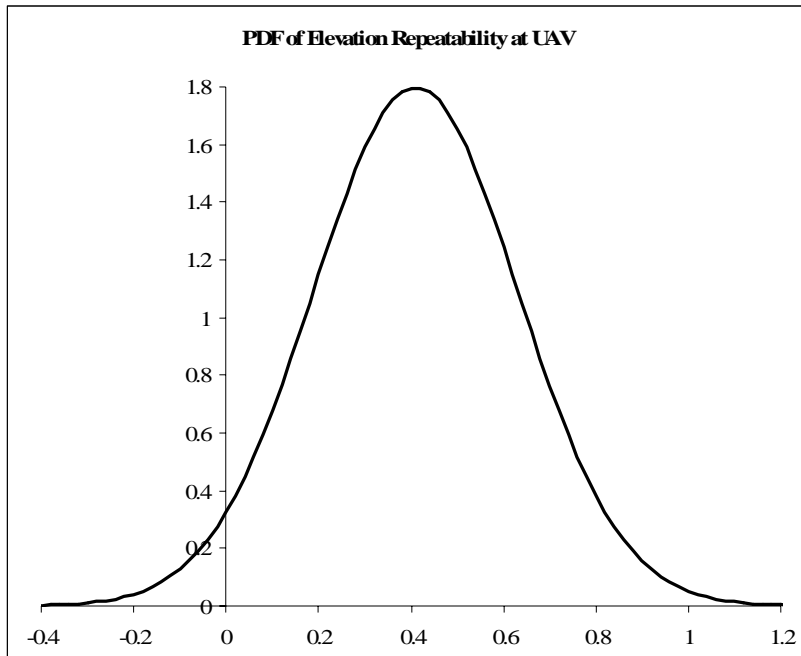
Figure 4.12 Distribution of elevation repeatability at UAV in meters.
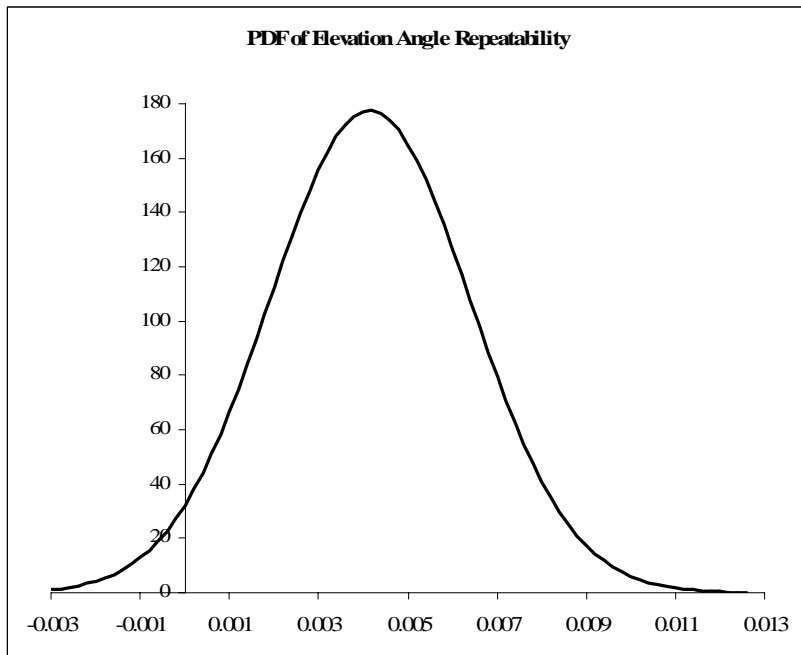
Figure 4.13 Distribution of elevation repeatability at UAV in meters.

An error distribution associated with the ground-to-UAV FSO communications link depicted in Figure 4.6 was calculated from the gimbal accuracy measurements. The gimbal error PDF measured in meters is shown in Figure 4.14. An analysis of the data showed that the gimbal has a mean pointing error of 0.3 *m* with a standard deviation of 0.2 *m*. The corresponding error PDF converted into an error angle (in degrees) is shown in Figure 4.15. An analysis of this error data shows that the gimbal has a mean error of 0.0032° (55.85 *μrad*) with a standard deviation of 0.002° (34.91 *μrad*).
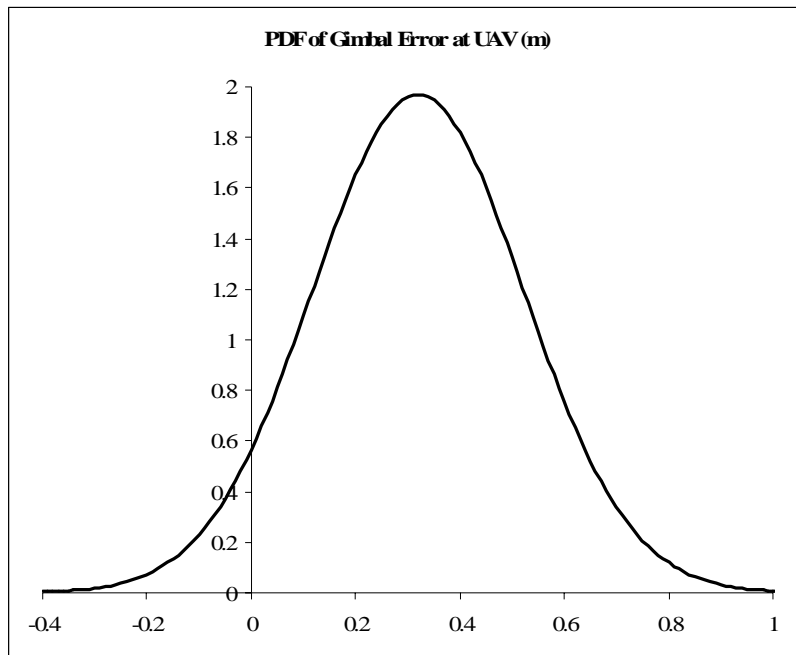
Figure 4.14 Distribution of gimbal error at UAV measured in meters.

PDF of Error at UAV (Degrees)
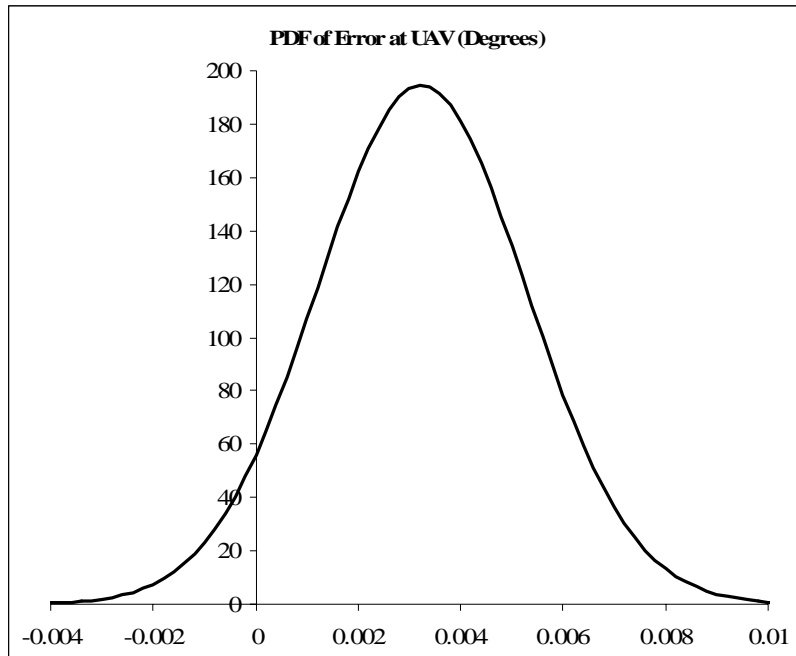
Figure 4.15 Distribution of angular gimbal error measured in degrees.

The experimental analysis of a mechanical gimbal presented in this section has shown that a gimbal pointing error of 0.3 *m* with a standard deviation of 0.2 *m* needs to be accounted for in the FSO link when the UAV has a flight altitude of 4 *km* and a flight radius of 4 *km*. One method of mitigating the pointing error of the gimbal is to use the divergence present in the FSO link to offset the error. Section 4.3.2 provides an analysis of the expected beam profile in the presence of atmospheric turbulence in order to determine if divergence can be used to offset the gimbal pointing error present in the FSO communications link.

4.3.2 Simulation Results

In this section, the simulation results obtained from the atmospheric turbulence model will be discussed. The simulation results presented in this section are based on a modified atmospheric spectrum. The functional form of this spectrum is given by [30]:

$$\Phi_n(\kappa) = 0.033 C_n^2 \left[1 + 1.802 \left(\frac{\kappa}{\kappa_l} \right) - 0.254 \left(\frac{\kappa}{\kappa_l} \right)^{\frac{7}{6}} \right] \frac{\exp - \left(\frac{\kappa^2}{\kappa_l^2} \right)}{\left(\kappa^2 + \kappa_0^2 \right)^{\frac{11}{6}}}, \tag{4.5}$$

where $\kappa_l = \dfrac{3.3}{l_0}$ and $\kappa_0 = \dfrac{1}{L_0}$.

A plot of the normalized mean intensity of the 1550 *nm* FSO laser as a function of radial distance from the optical axis of the laser beam is shown in Figure 4.16. The data in the plot was normalized due to too few significant digits being presented in the simulation data. In the presence of atmospheric turbulence, that laser beam at the UAV has a Gaussian intensity profile with an effective spot size of 10.56 *m*. From this data, it is observed that the effective spot size is approximately 35 times larger than the mean of the gimbal error distribution for the 4 *km* UAV altitude. Based on this result, the divergence is more than sufficient to offset pointing errors due to the gimbal.

99
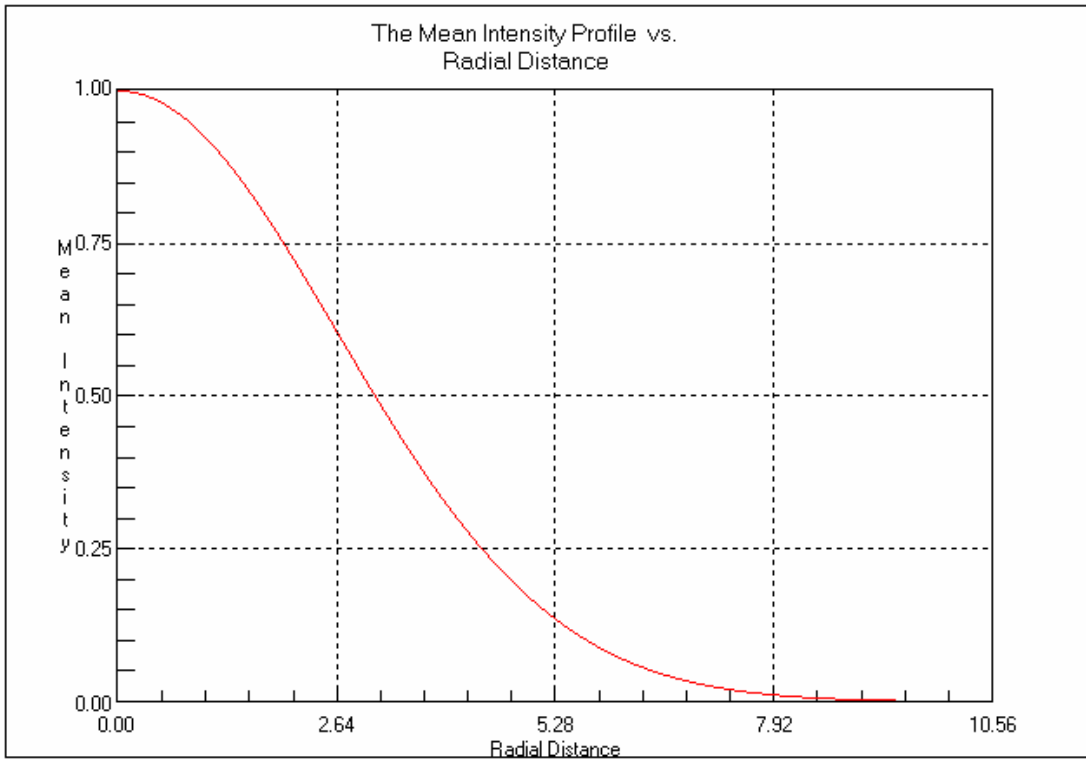
Figure 4.16 Normalized mean intensity profile versus radial distance.

The off-axis scintillation index versus pointing error for the ground-to-UAV FSO link is shown in Figure 4.17. The figure shows the total scintillation index at the receiver plane as a function of radial distance from the optical axis. It is observed that the scintillation index varies from 1.193 at the optical axis to 1.20 at the diffractive beam edge.

100
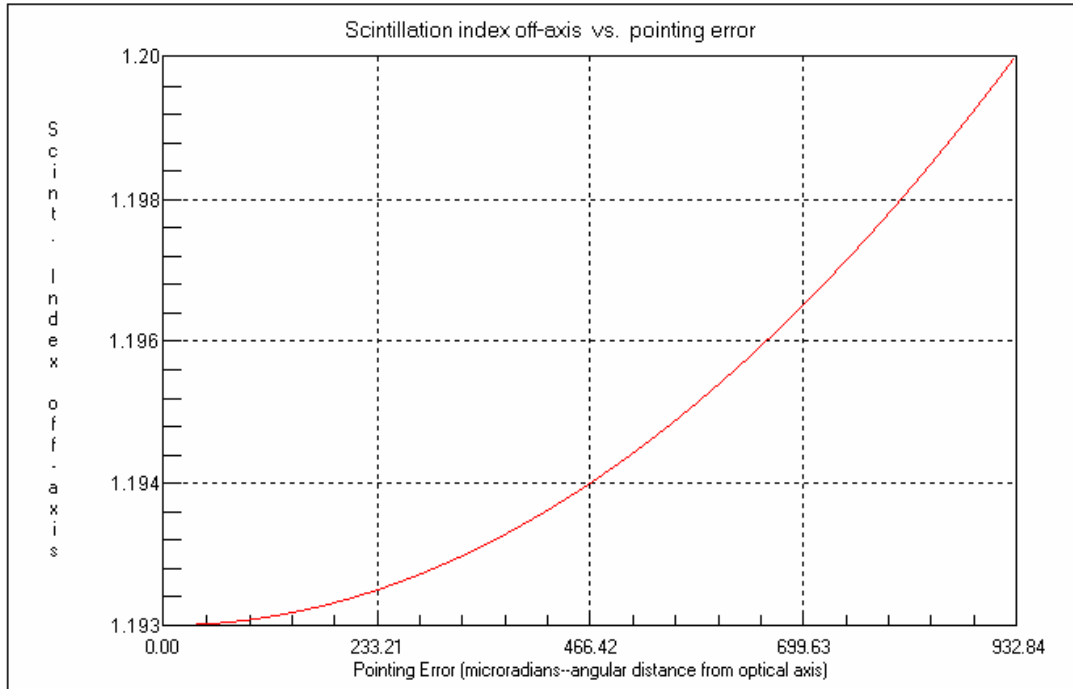
Figure 4.17 Off-Axis scintillation index versus pointing error.

Figure 4.18 shows a plot of the total variance of intensity versus pointing error. The total variance of intensity is defined as the product of the scintillation index and the square of the mean intensity. The data presented in this plot has again been normalized due to limitations on the number of significant decimal places calculated by the simulation software.
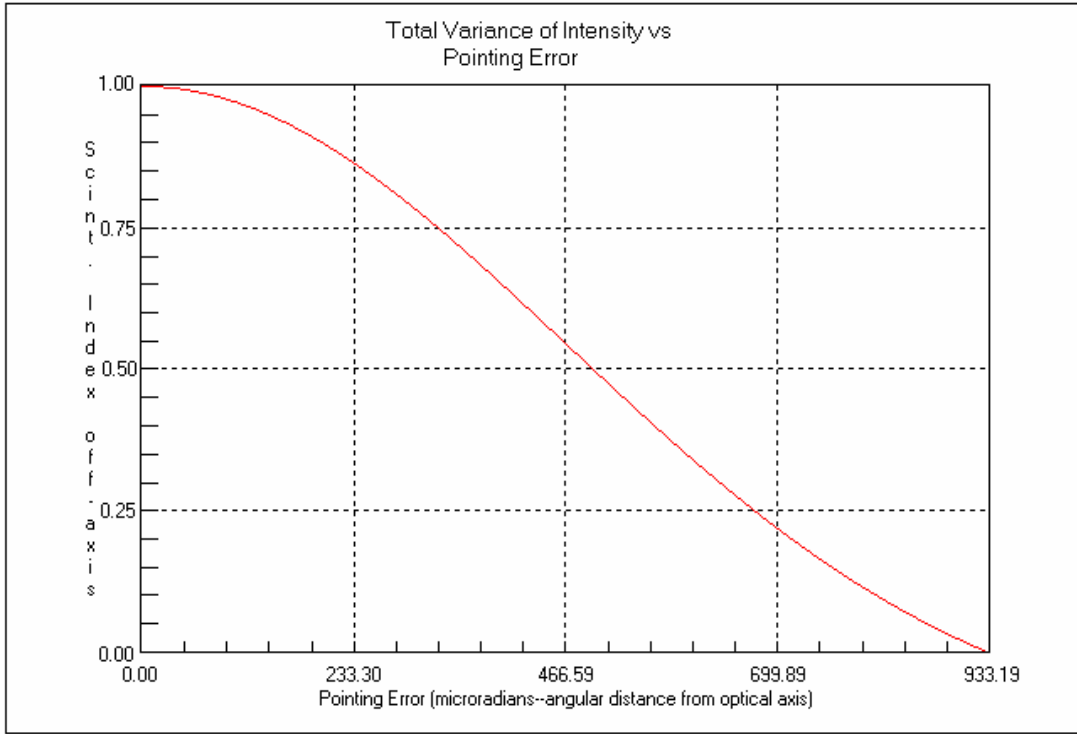
Figure 4.18 Total variance of intensity versus pointing error.

Figure 4.19 shows a plot of the scintillation index as a function of the turbulence parameter σ_l, where [57]:

$$\sigma_1 = \sqrt{1.23 C_n^2 k^{7/6} L^{11/6}}, \qquad (4.6)$$

with $L = 5656.85\ m$ (the propagation path of the FSO link). Based on the receiver configuration described in Section 4.2.2, the probability that the signal level will drop below the threshold of 30 dB was calculated to be 3.69×10^{-29}. The simulation software assumes that the signal-to-noise ratio of the receiver is of sufficient

magnitude that the probability of a fade is due only to atmospheric effects. The corresponding mean fade time, or the amount of time that a fade will remain below the signal threshold was 0.00002 *ms*.
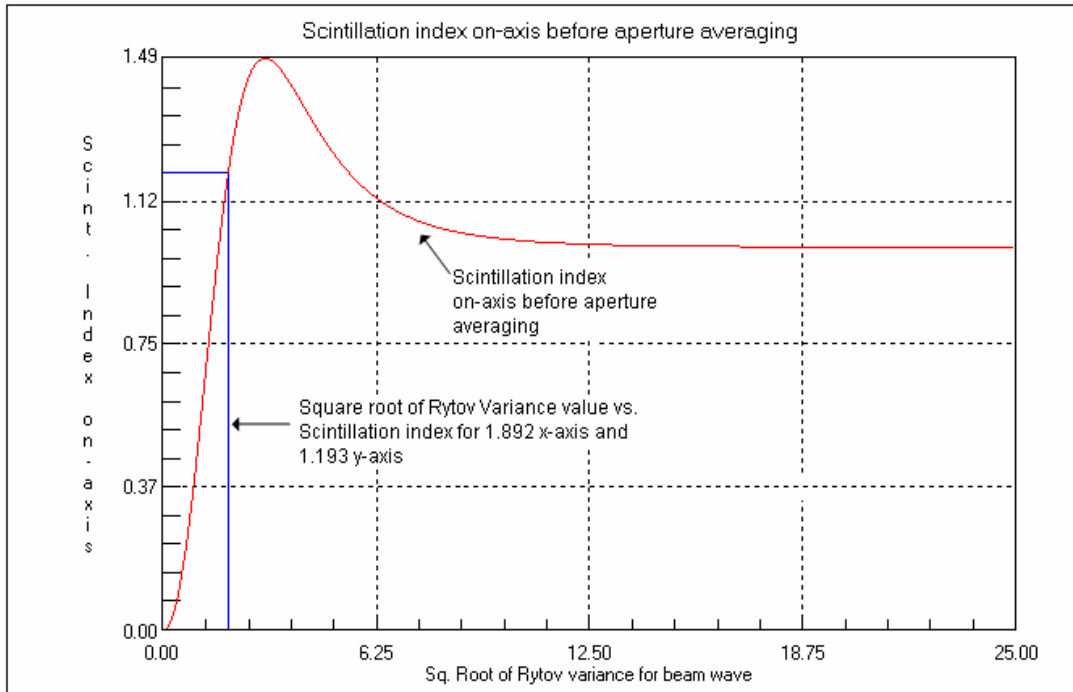
Figure 4.19 Scintillation index as a function of turbulence.

The data obtained from the simulation software is calculated based on the "worst case scenario" of atmospheric turbulence in which the laser beam is propagating through an area of constant atmospheric turbulence. Because the effects of atmospheric turbulence and scintillation decrease with altitude, the expected measured values for these parameters would in fact be lower for the ground-to-UAV FSO communications link.

4.3.3 Gimbaled Beam Steering and Geometric Loss

The following observations can be made based on the experimental measurement of the gimbal repeatability and error and the simulated effects of atmospheric turbulence on the FSO laser beam for a ground-to-UAV communications link:

- In the presence of atmospheric turbulence, a Gaussian beam profile with a spot size of 10.56 *m* is expected.

- The repeatability associated with a mechanical gimbal was experimentally determined to be an elevation of 0.41 *m* and 1.24 *m* azimuth. The corresponding error was determined to be 0.3 *m*.

From these observations it is expected that for a ground-to-UAV FSO communications link operating at 1550 *nm*, the effects of divergence in the presence of atmospheric turbulence will result in a beam profile that can effectively offset both repeatability and accuracy errors associated with a gimbaled alignment and tracking system.

The geometric loss associated with the ground-to-UAV FSO link described in this section was calculated to be -15.5 *dB*. Based on this calculation, the geometric loss

present in such an FSO communications link would not cause the power of the laser to decrease to a level that is undetectable by an FSO receiver.

4.4 Summary

This chapter has reported both experimental and simulation results for the use of a mechanical gimbal for alignment and tracking of a ground-to-UAV FSO link. Based on the experimental results presented, an FSO link used to supplement existing RF technologies could be effectively aligned and tracked using a mechanical gimbal, although further use of an active optical beam steering element will be needed to offset vibrations present in the UAV. The amount of beam divergence present in such an FSO link is sufficient to offset any error introduced into the alignment and tracking algorithm by the gimbal. Furthermore, a very low probability of signal fade is expected for a ground-to-UAV FSO link. Finally, based on the divergence simulation, the geometric loss expected for a ground-to-UAV FSO link would not prove to be a limiting factor in the link performance.

Chapter 5

Wavelength Diversity in the Presence of

Atmospheric Turbulence

5.1   Introduction

A wavelength diversity scheme to improve the performance of a ground-to-UAV FSO communications link in the presence of atmospheric turbulence is presented in this chapter. Chapter 4 introduced the effects that atmospheric turbulence has on the laser beam spot size in the receiver plane of a standard 1.55 μm ground-to-UAV FSO communications link. In this chapter the effect of atmospheric turbulence on three different wavelengths, 1.55 μm, 0.85 μm and 10 μm is analyzed through simulation techniques.   Different optical wavelengths have advantages for use in FSO communications links depending on the amount of atmospheric turbulence and the prevalent atmospheric weather conditions. Because of the difficulty in establishing and maintaining an FSO link between a ground station and a moving UAV, a wavelength diversity scheme is seen as a possible method to minimize the time required to align the FSO communications link. The detailed analysis of the effects of atmospheric turbulence on each of the three wavelengths used in the simulation will lead to a proposed method of using different wavelengths in the same FSO transceiver to assist with the alignment and tracking of a ground-to-UAV FSO communications link.

The remainder of this chapter is organized as follows: In Section 5.2, the proposed FSO link configuration, the simulation configuration and atmospheric turbulence simulation model is discussed. Section 5.3 discusses the simulation results obtained from the simulation software. Section 5.4 will discuss a proposed wavelength diversity scheme for minimizing link acquisition time and concluding remarks will be presented in Section 5.5.

5.2   FSO Link Configuration for Simulation

This section will describe the link configuration for the calculations performed in the simulation. Figure 5.1 shows the schematic overview of the ground-to-UAV FSO communications link. The ground-to-UAV link consists of a transmitter-receiver pair, one of which is mounted on a ground station mechanical gimbal and the other is mounted on a mechanical gimbal on the UAV. The link is configured as a bi-directional FSO communications link.
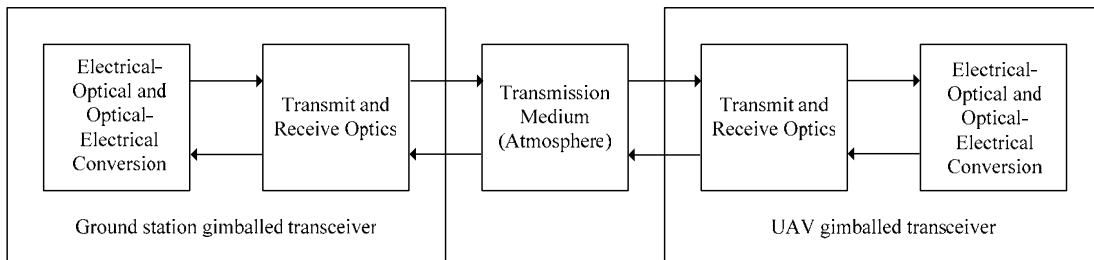
Figure 5.1 Ground-to-UAV bi-directional FSO link configuration.

The simulations performed for this investigation considered a UAV flying in a fixed circular path directly above the ground station and were run using Atmospheric Laser Turbulence Model (ALTM) software from ONTAR Corporation [57] in a similar configuration to that which was described in Section 4.2.2. Figure 5.2 shows a schematic view of this configuration. For the FSO link, the UAV flight radius was again set at 4 *km*, but for the wavelength diversity scheme, the cruising altitude was allowed to be either 4 or 8 *km* which increases the range over which the proposed FSO communications link would be viable. The FSO transmitter is allowed to transmit one of three wavelengths: 0.85 *μm*, 1.55 *μm* or 10 *μm*. The wavelengths were selected based on their performance in various weather conditions, which will be discussed in more detail in Chapter 6.
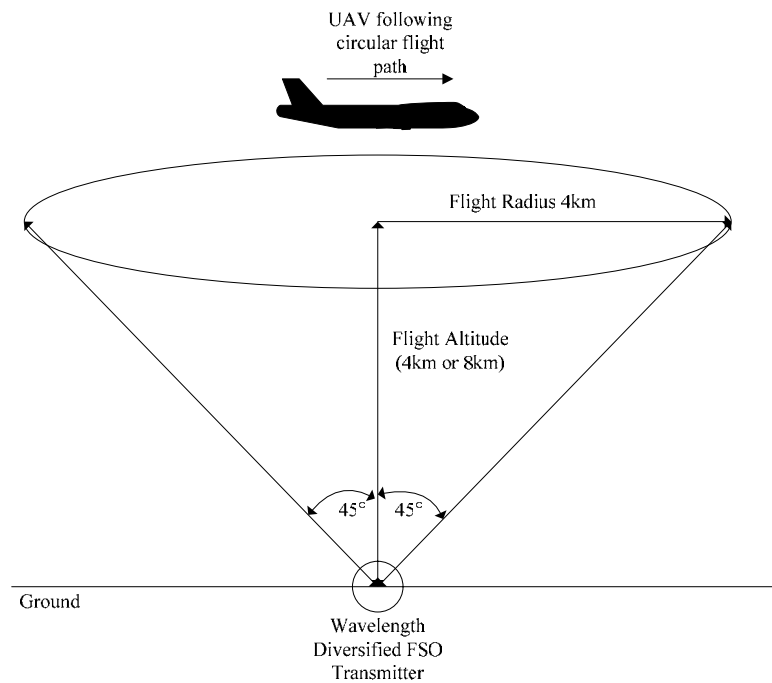
Figure 5.2 Ground-to-UAV FSO link configuration for simulation.

108

The transmitter output power was again set to 20 mW. Although the simulation is now considering a longer link with an 8 km altitude, an output power of 20 mW is still sufficient to achieve transmitter-receiver connectivity. The transmitter input beam profile, $2W_0$, where W_0 is given by [55]:

$$U_0(r,0) = a_0 \exp\left(-r\frac{r^2}{W_0^2} - \frac{ikr^2}{2F_0}\right), \qquad (5.1)$$

where $U_0(r,0)$ is the complex amplitude of the wave, a_0 is the amplitude of the wave on the optical axis, F_0 is the radius of curvature of an assumed parabolic distribution of the phase, r is the distance from the beam center line in the transverse direction, k is the optical wave number and α is a complex parameter related to spot size and phase front radius of curvature given by [55]:

$$\alpha = \frac{2}{kW_0^2} + i\frac{1}{F_0} . \qquad (5.2)$$

The input value of $2W_0$ was selected to be 2.0 cm. The input value for the half-angle divergence for the FSO link was chosen to be 260 μrad. This figure was based on calculations that would ensure a beam profile that is approximately ten times larger than the gimbal error calculated in Chapter 4. The amount of divergence present in the FSO link has been reduced from the amount presented in Chapter 4. This reduction is based on the accuracy measurements of the gimbal that were presented in

109

Chapter 4 and because the divergence presented in Chapter 4 was based on commercially available FSO systems that are good up to approximately 4 *km* transmitter-receiver separation. The inner scale of the atmospheric turbulence was set at 5 *mm* and the outer scale at 1 *m*. The inner scale represents the smallest scale of unstable air eddies and the outer scale represents the largest scale of the unstable air eddies. The values selected for the wavelength diversity simulation are considered to be typical values for normal air turbulence. The final atmospheric parameter required is the atmospheric structure parameter, C_n^2, which is given by [56]:

$$C_n^2 = \left(79 \times 10^{-6} \frac{P}{T^2} \right)^2 C_T^2,$$
(5.3)

where P is the pressure in millibars, T is the temperature in Kelvin and C_T^2 is the temperature structure constant. The value selected for C_n^2 was 7.5×10^{-15} $m^{-2/3}$ which is approximately the midpoint between "weak turbulence" and "strong turbulence". The ALTM software uses a modified atmospheric spectrum with a functional form given by [56]:

$$\Phi_n(\kappa) = 0.033 C_n^2 \left[1 + 1.802 \left(\frac{\kappa}{\kappa_l} \right) - 0.254 \left(\frac{\kappa}{\kappa_l} \right)^{\frac{7}{6}} \right] \frac{\exp\left(-\frac{\kappa^2}{\kappa_l^2}\right)}{\left(\kappa^2 + \kappa_0^2\right)^{\frac{11}{6}}},$$
(5.4)

where $\kappa_l = \dfrac{3.3}{l_0}$ and $\kappa_0 = \dfrac{1}{L_0}$.

The receiver configuration for the wavelength diversity scheme consisted of a lens with a 10 *cm* aperture and a 10 *cm* focal length. The lens aperture and focal length have been reduced from the values presented in Chapter 4 in order to decrease the size of the FSO transceivers which will decrease the effective weight the gimbal has to control. The receiver threshold was set to 30 *dB* below the mean and the noise bandwidth of the atmosphere was set at 550 *Hz*, both of which are considered to be normal values.

5.3 Results

In this section, the simulation results for the ground-to-UAV FSO communications link in the presence of atmospheric turbulence are reported. The results are divided into four sections, each of which contains the data for all three wavelengths and both cruising altitudes for the UAV.

5.3.1 Mean Intensity Profile

The mean intensity profile for the laser beam at the receiver plane provides a measure of the laser's intensity and physical profile. The mean intensity profile of the FSO laser beam at the UAV is important because the beam spot size can be used to offset alignment and tracking errors that are present in the communications link, as was shown in Chapter 4. In order to fully investigate the use of a wavelength diversity scheme to improve link alignment protocols, the mean intensity profile of each of the three wavelengths needs to be determined.

Figure 5.3 shows a plot of the mean intensity profile versus the radial distance from the centroid of the FSO laser beam for a 4 *km* UAV altitude with a 0.85 *μm* wavelength in the presence of atmospheric turbulence. The simulation results show an effective beam spot size of 2.995 *m* for the 4 *km* UAV altitude. This value shows that the beam profile is approximately a factor of ten times greater than the expected gimbal error of 0.3 *m* that was been reported in Section 4.3.
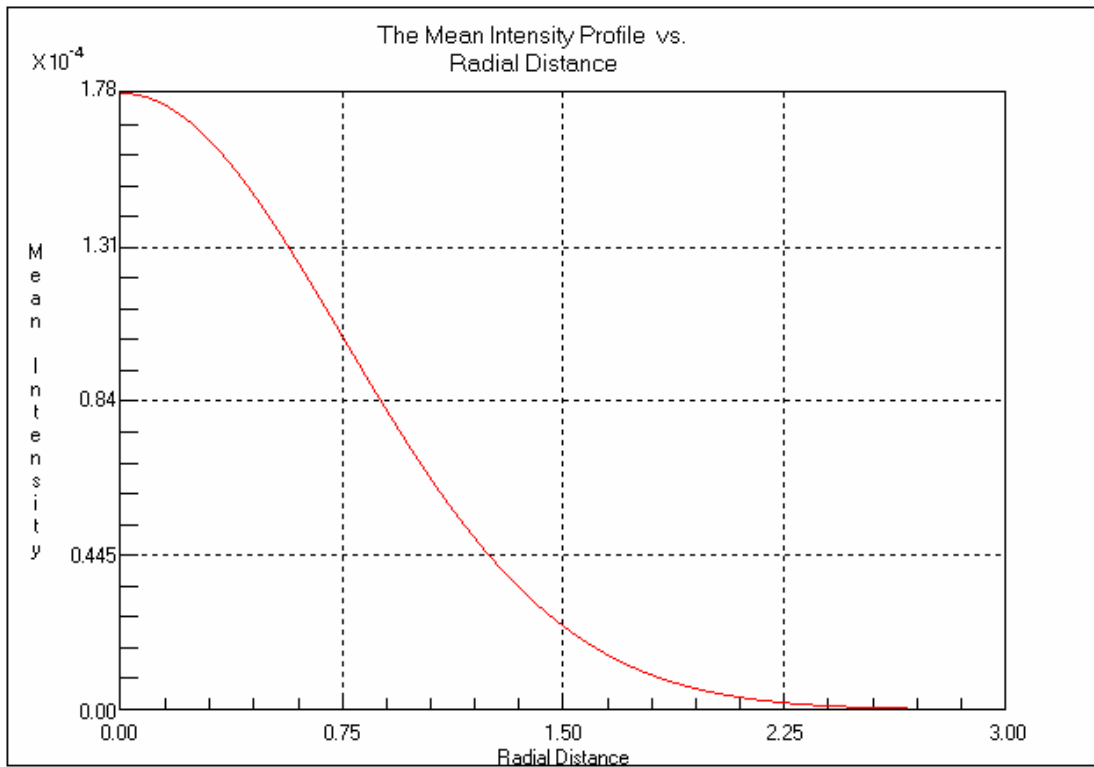
Figure 5.3 Plot of mean intensity profile versus radial distance for a 4 *km* UAV altitude with a 0.85 *μm* FSO wavelength.

Figure 5.4 shows the corresponding mean intensity profile plot for an 8 *km* UAV altitude with a 0.85 *μm* wavelength. For the 8 *km* altitude, the effective beam spot size at the receiver plane of the FSO communications link was calculated to be 4.75 *m*. The gimbal alignment error at a UAV altitude of 8 *km* would be 0.45 *m*, so as was the case for the 4 *km* UAV altitude, the laser beam effective spot size at the receiver is slightly larger than a factor of ten times greater than the gimbal error.
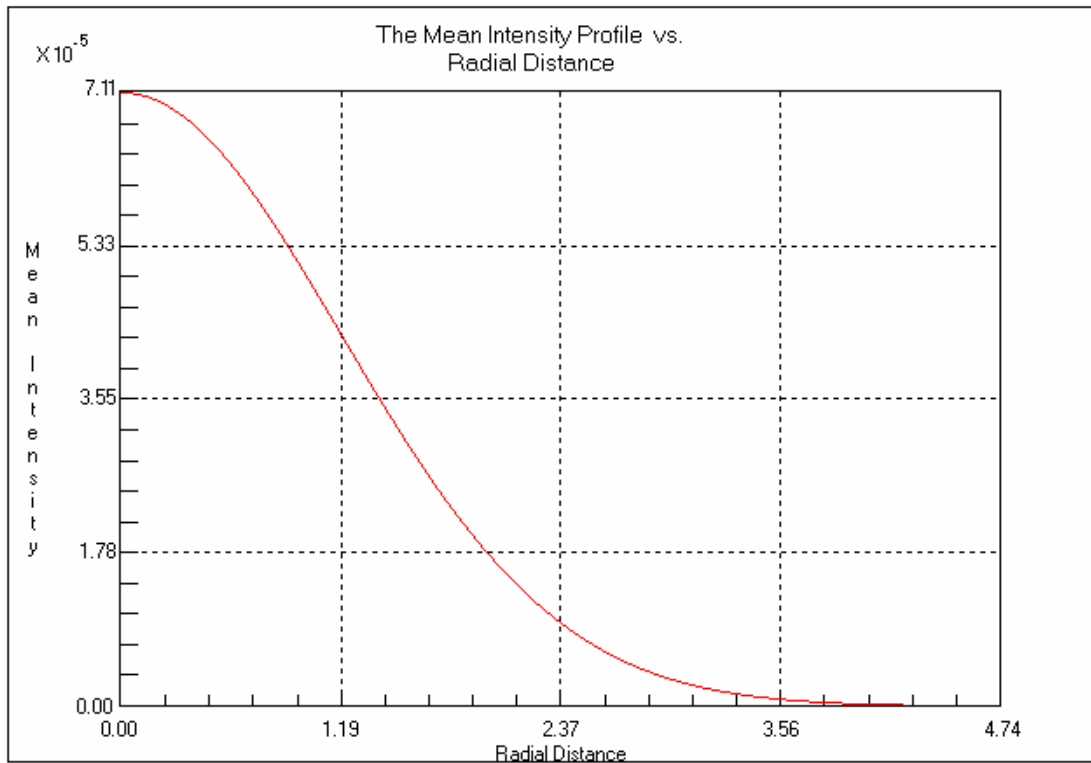
Figure 5.4 Plot of mean intensity profile versus radial distance for an 8 *km* UAV altitude

with a 0.85 *μm* FSO wavelength.

Figure 5.5 shows the corresponding mean intensity profile plot for a 1.55 *μm* FSO

communications link with a UAV altitude of 4 *km*. The simulation results show an

effective spot size of 3.03 *m* for this FSO link configuration. As was the case for the

0.85 *μm* link, the effective spot size is approximately an order of magnitude larger

than the gimbal induced alignment error.
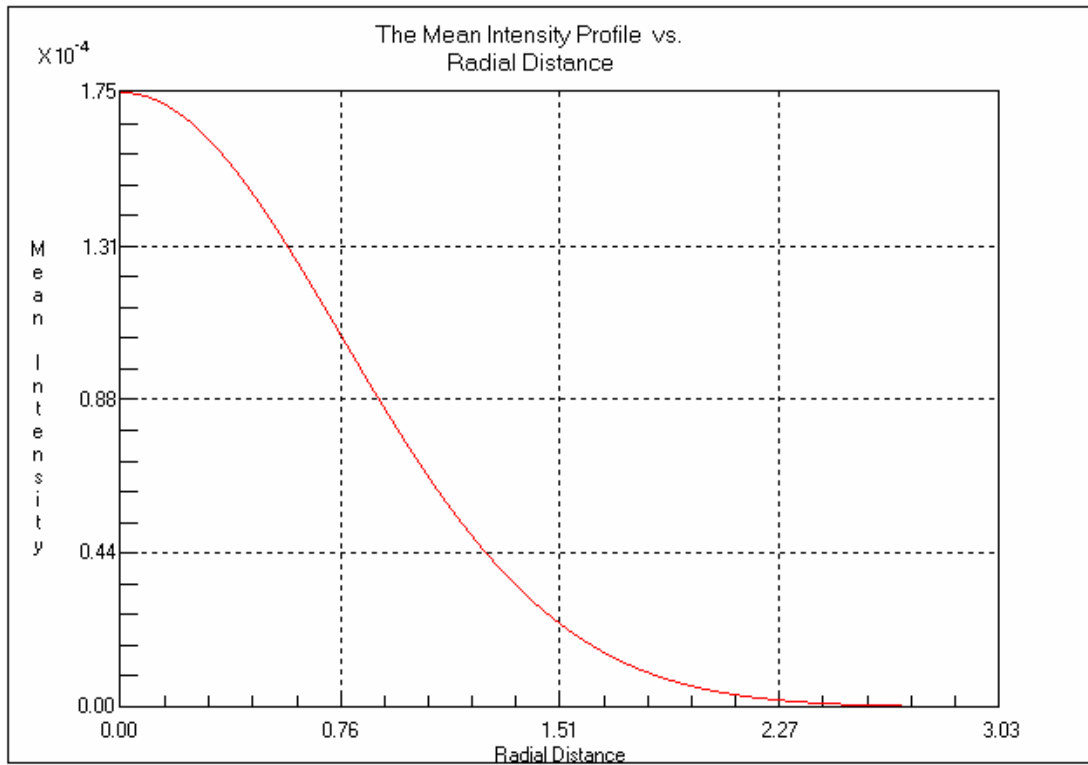
Figure 5.5 Plot of mean intensity profile versus radial distance for a 4 *km* UAV altitude with a 1.55 *μm* FSO wavelength.

Figure 5.6 shows the mean intensity profile plot for the 8 *km* UAV altitude with a 1.55 *μm* FSO wavelength. The simulation results show that the expected beam profile in the receiver plane is a Gaussian profile with an effective spot size of 4.79 *m*. This effective beam profile spot size is also slightly more than an order of magnitude larger than the gimbal alignment error of the FSO system.
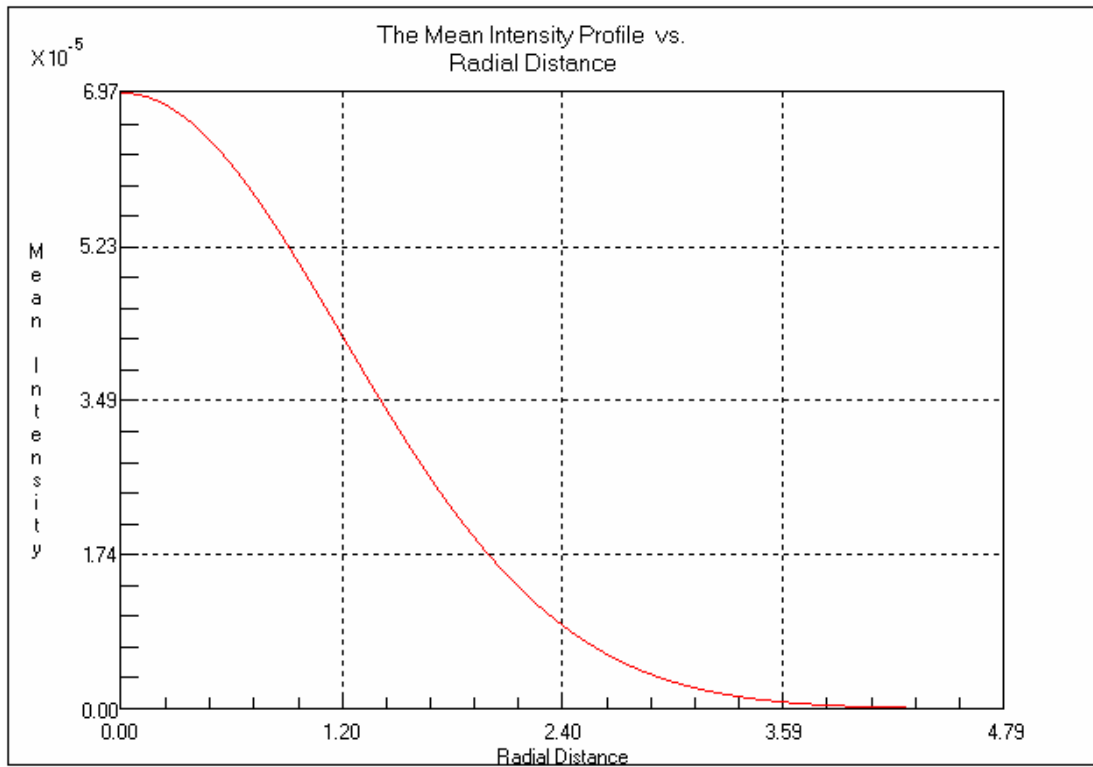
Figure 5.6 Plot of mean intensity profile versus radial distance for an 8 *km* UAV altitude with a 1.55 *µm* FSO wavelength.

The final simulated data for the mean intensity profile of a 10 *µm* FSO link with a 4 *km* UAV altitude is shown in Figure 5.7. An FSO communications link operating at 10 *µm* has been shown to be useful for offsetting the effects of fog on a horizontal terrestrial FSO communications links [11], which will discussed in more detail in Chapter 6. The simulation data shows an effective spot size of 4.67 *m* for a 4 *km* UAV altitude. This effective spot size is over 15 times larger than the gimbal induced error present in the FSO communications link.
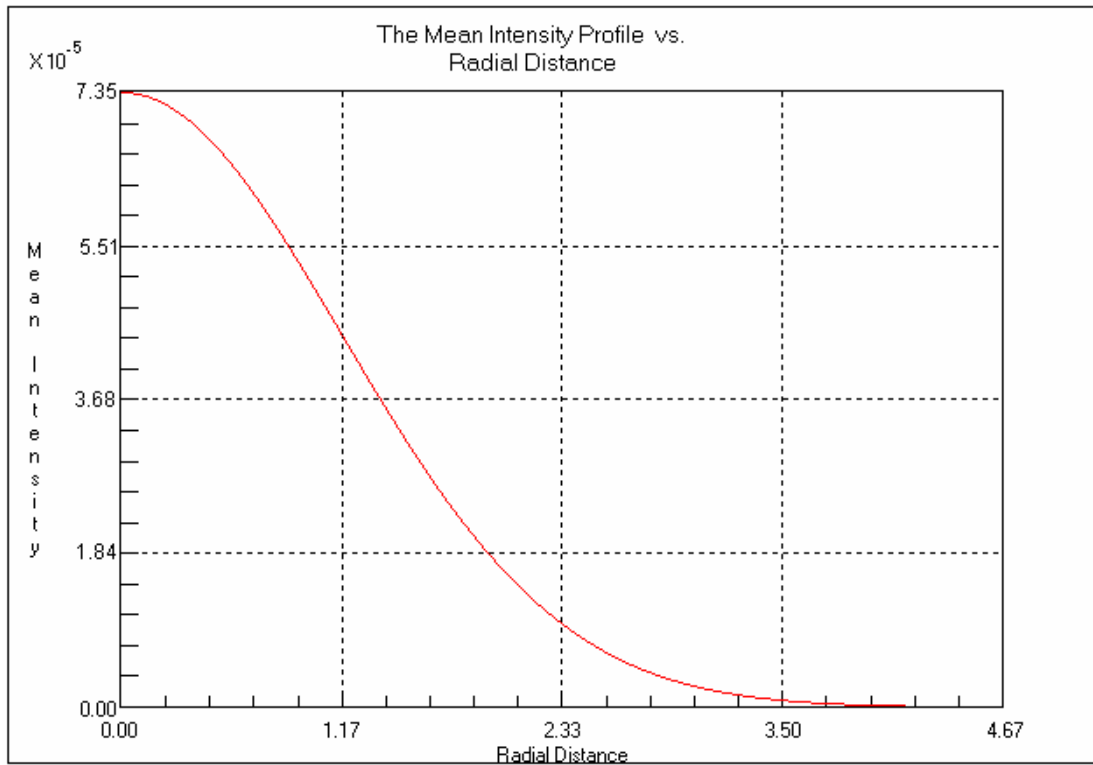
Figure 5.7 Plot of mean intensity profile versus radial distance for a 4 *km* UAV altitude with a 10 *μm* FSO wavelength.

Figure 5.8 shows the receiver plane beam profile for an 8 *km* UAV altitude operating at a 10 *μm* wavelength. The effective beam spot size of this link is calculated to be 7.38 *m*, which is over 16 times larger than the gimbal alignment error. It can be observed that for longer wavelengths, the beam spot size in the receiver plane is larger than for the same length link with a shorter wavelength.
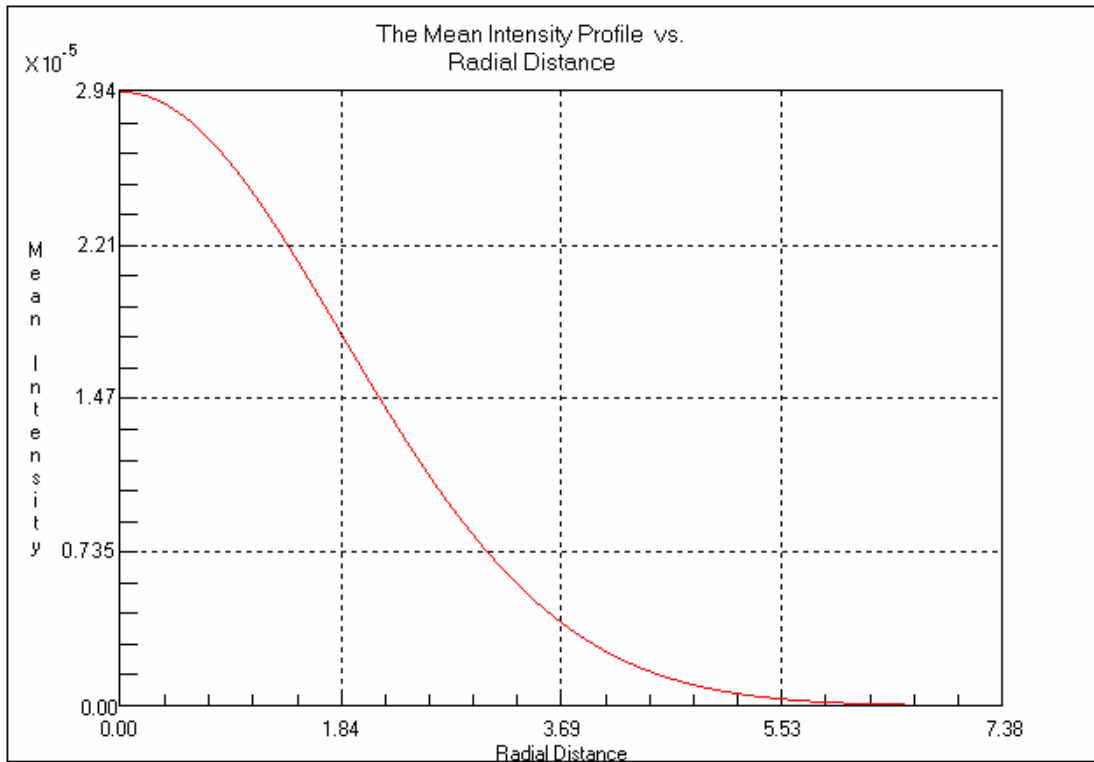
Figure 5.8 Plot of mean intensity profile versus radial distance for an 8 *km* UAV altitude

with a 10 *μm* FSO wavelength.

While all three of these beam profiles fall within an acceptable range for gimbal-error offset to occur, it is observed that the use of multiple wavelengths may prove to be highly beneficial for the process of link acquisition and tracking in ground-to-UAV FSO communications links. The use of wavelengths that diverge at a faster rate in the presence of turbulence would allow for a larger beam profile area to perform initial course alignment algorithms. A link acquisition protocol based on this premise will be introduced in Section 5.4.

5.3.2 Off-axis scintillation index

The simulation calculates information relating the total scintillation index at the receiver plane to the radial distance from the optical axis of the FSO communications link. The results obtained using the input parameters described in Section 5.2 will be discussed in this section.

Figure 5.9 shows a plot of the off-axis scintillation index compared the radial distance from the optical axis for the 0.85 *μm* FSO link with a 4 *km* UAV altitude. It is observed that the scintillation index varies from 1.896 at the optical axis to 1.961 at the diffractive beam edge at the receiver plane of the FSO communications link. The scintillation index is calculated by the following expression:

$$\sigma_I^2(\vec{r},L) = 4.42\sigma_1^2\Lambda_e^{5/6}\left[1-1.15\left(\frac{\Lambda_e}{kL_0^2}\right)^{1/6}\right]\frac{r^2}{W_e^2} + \exp\left[\sigma_{\ln x}^2(l_0) - \sigma_{\ln x}^2(L_0) + \frac{0.51\sigma_G^2}{\left(1+0.69\sigma_G^{12/5}\right)^{5/6}}\right] - 1. \quad (5.5)$$

Scintillation indices in this range result in a probability of a fade of 1.22×10^{-7}, which is calculated using [30]:

$$\Pr(u \le u_T) = \int_0^{u_T}\int_0^\infty \delta(u-s)p_I(s)dsdu \quad , \quad\quad\quad (5.6)$$

where $p_I(s)$ is the PDF associated with the irradiance power fluctuations, and $\delta(u$-$s)$ is the Dirac delta function. The corresponding number of fades expected is 4.63×10^{-2}. The mean fade time, which is defined as the average time the signal will stay below the prescribed threshold value given that a fade has occurred is calculated to be 0.0026 *ms*. The scintillation index (or flux variance) on the photodetector is calculated to be 0.496 using [30]:

$$\sigma_I^2(D,l_0,L_0) = \exp\left[\sigma_{\ln x}^2(D,l_0) - \sigma_{\ln x}^2(D,l_0) + \sigma_{\ln y}^2(D,l_0)\right] - 1, \qquad (5.7)$$

where $\sigma_{\ln x}^2(D,l_0) - \sigma_{\ln x}^2(D,l_0)$ is the large scale log irradiance, and $\sigma_{\ln y}^2(D,l_0)$ is the small scale log irradiance. The aperture averaging factor or the ratio of the flux variance at the photodetector to the scintillation index in the receiver pupil plane is 0.262.
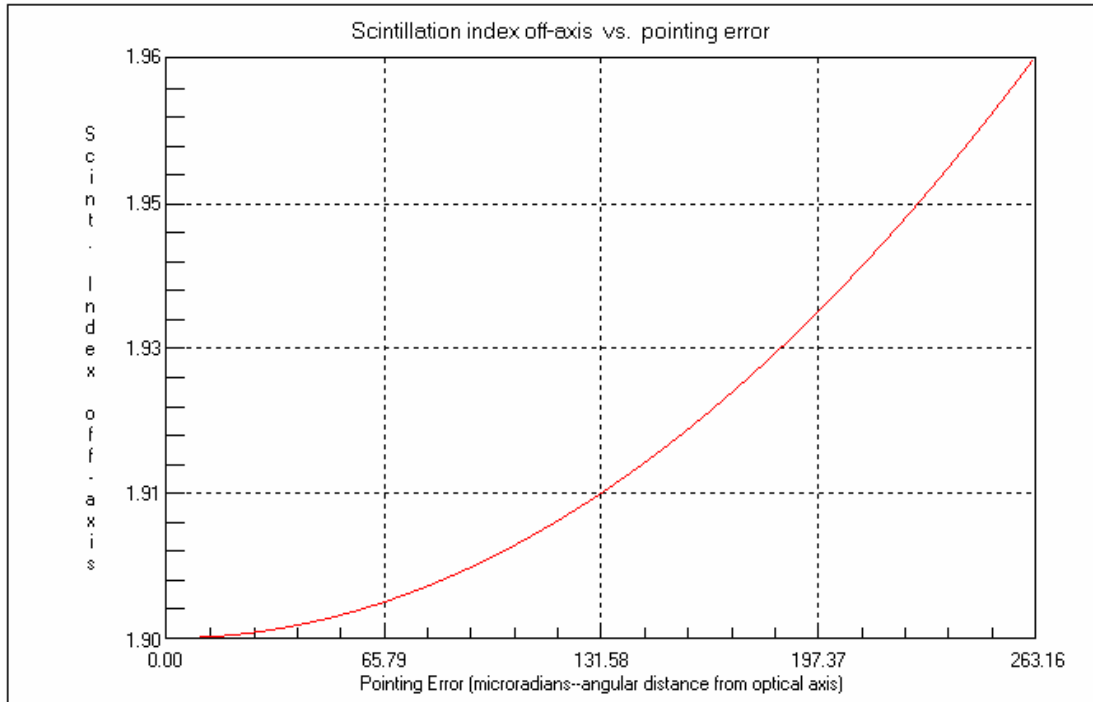
Figure 5.9 Off-axis scintillation index versus pointing error for a 4 *km* UAV altitude

with a 0.85 *μm* wavelength.

Figure 5.10 shows the corresponding plot for the 8 *km* UAV altitude. The scintillation index varies from 1.922 at the optical axis to 2.023 at the diffractive beam edge, with a corresponding probability of fade of 3.63×10^{-8} and an expected number of fades of 2.30×10^{-2}. The mean fade time is calculated to be 0.0016 *ms*. The scintillation index on the photodetector is 0.455 and the aperture averaging factor is 0.236.
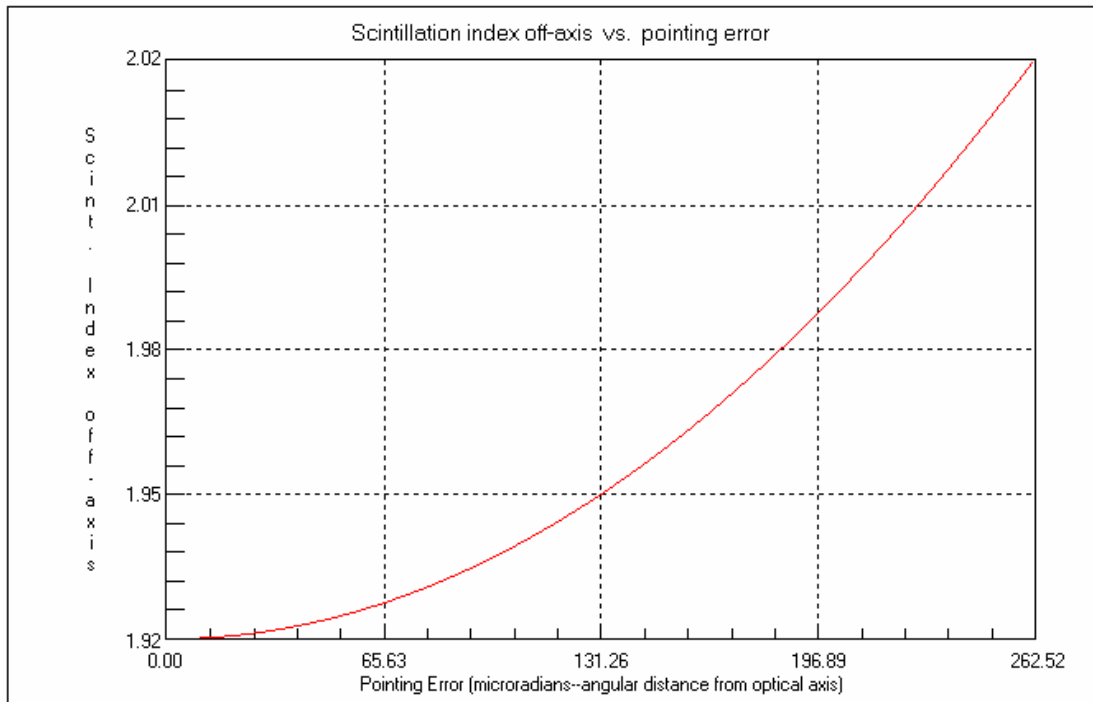
Figure 5.10 Off-axis scintillation index versus pointing error for an 8 *km* UAV altitude with a 0.85 *μm* wavelength.

The off-axis scintillation index versus pointing error for the 1.55 *μm* FSO link is shown in Figure 5.11. For a 4 *km* UAV altitude, the scintillation index was calculated to be 1.189 on the optical axis and 1.24 at the diffractive beam edge. The probability of a fade occurring is 6.21×10^{-9} and the expected number of fades is 8.75×10^{-4}. The mean fade time is calculated to be 0.0071 *ms*. The scintillation index on the photodetector is 0.474 and the aperture averaging factor is 0.399.
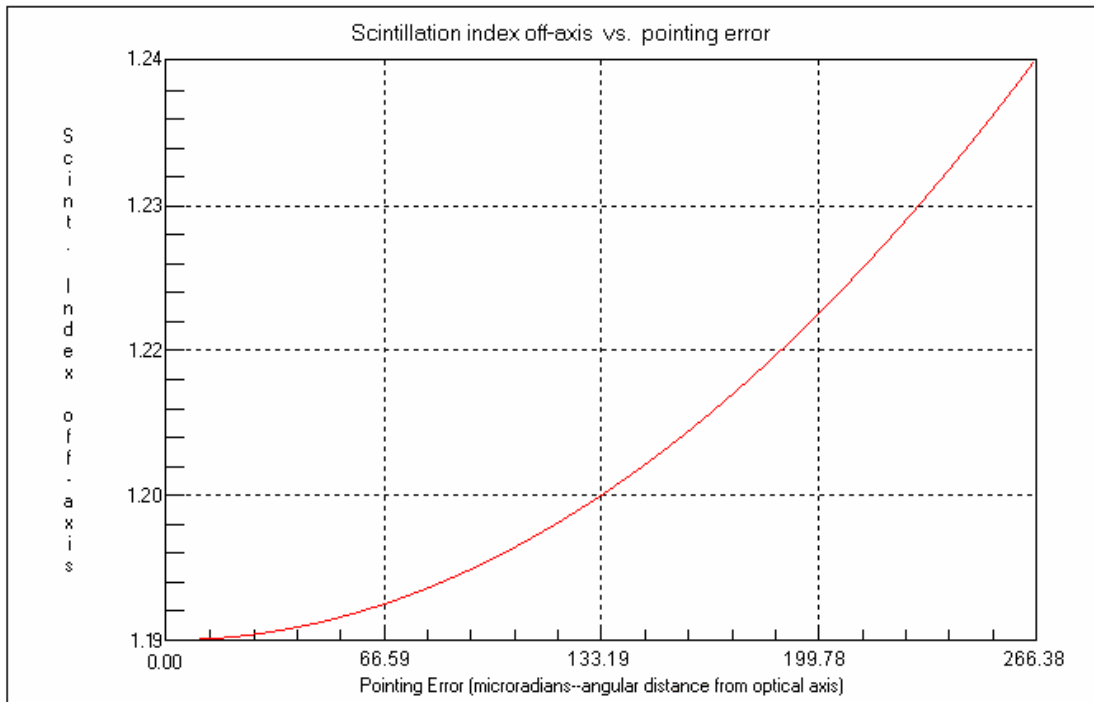
Figure 5.11 Off-axis scintillation index versus pointing error for a 4 *km* UAV altitude with a 1.55 *μm* wavelength.

The corresponding plot for the 8 *km* altitude is shown in Figure 5.12. For the 8 *km* UAV altitude, the scintillation index is 1.486 on the optical axis and 1.566 at the diffractive beam edge, with a probability of a fade occurring of 1.86×10^{-8} and an expected number of fades of 2.44×10^{-3}. For the increased altitude of this simulation run, the mean fade time is calculated to be 0.0076 *ms* with a scintillation index on the photodetector of 0.511 and an aperture averaging factor is 0.344.
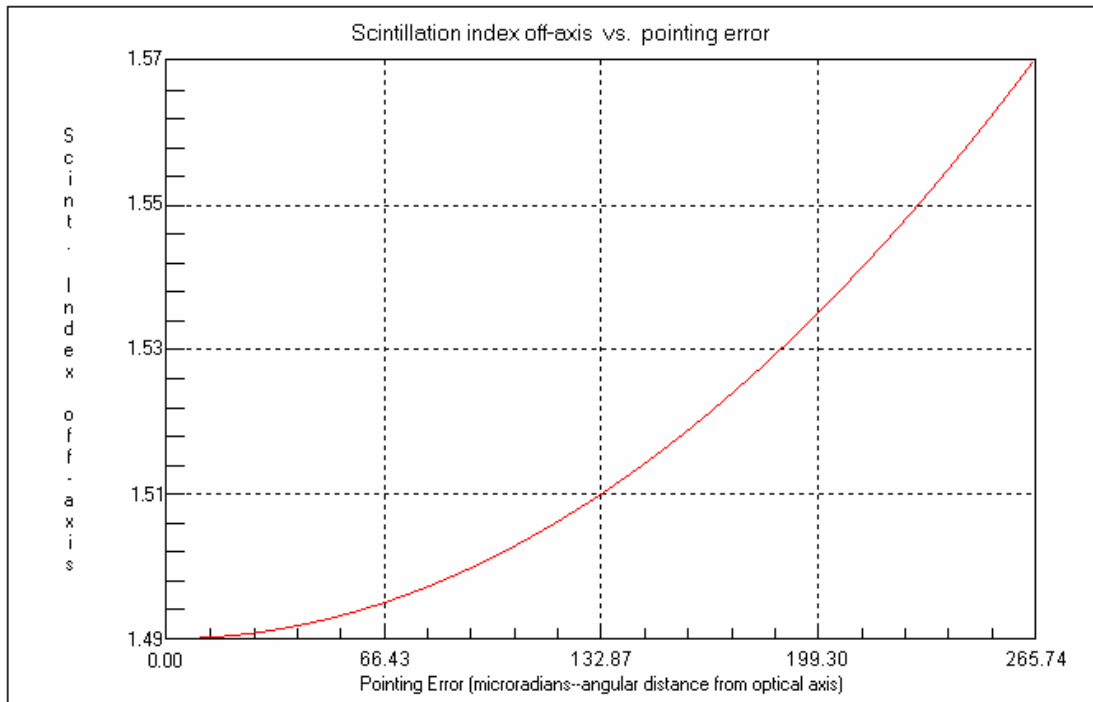
Figure 5.12 Off-axis scintillation index versus pointing error for an 8 *km* UAV altitude

with a 1.55 *μm* wavelength.

The corresponding plot for the 10 *μm*, 4 *km* FSO communications link is shown in Figure 5.13. For a 4 *km* UAV altitude, the scintillation index was calculated to be 0.139 on the optical axis and 0.151 at the diffractive beam edge, with a probability of a fade occurring of 3.21×10^{-35} and an expected number of fades of 1.12×10^{-29}. The mean fade time for this simulation configuration is 0.0029 *ms*. The photodetector based scintillation index is 0.118 with an aperture averaging factor of 0.848.
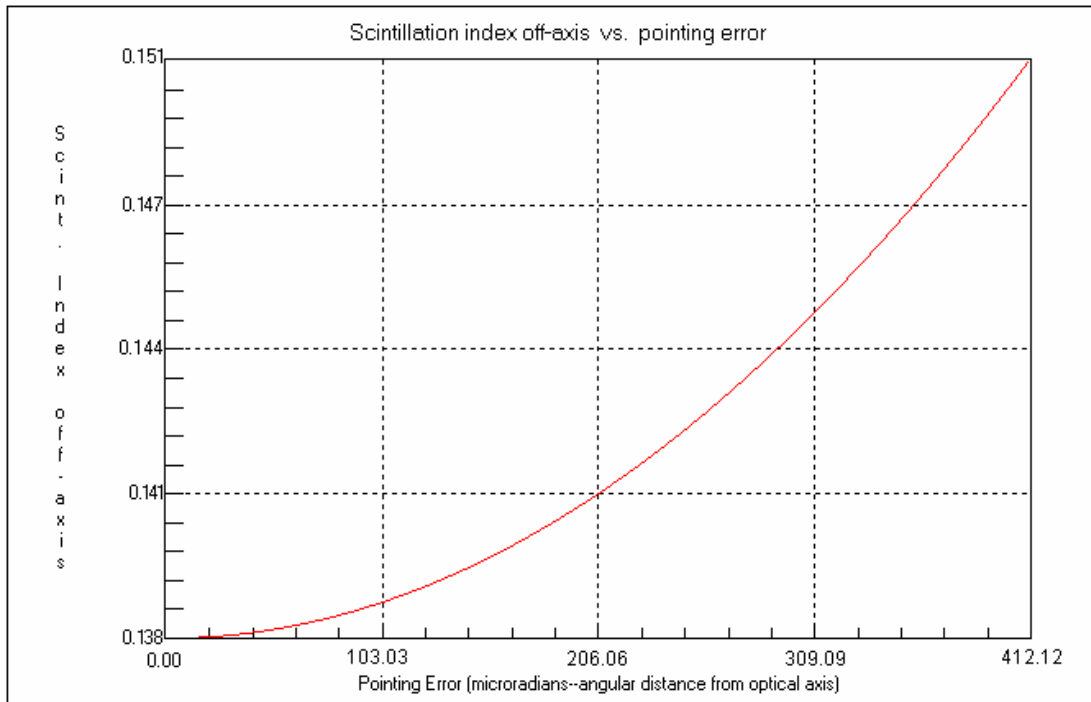
Figure 5.13 Off-axis scintillation index versus pointing error for a 4 *km* UAV altitude with a 10 *μm* wavelength.

For the 8 *km* UAV altitude, the scintillation index is 0.268 on the optical axis and 0.288 at the diffractive beam edge. This data is depicted in Figure 5.14. The probability of a fade was found to be 5.18×10^{-16} with an expected number of fades of 1.99×10^{-10}. A mean fade time of 0.0026 *ms* is expected to occur in this FSO communications link configuration. The scintillation index on the photodetector plane is calculated to be 0.233 with an aperture averaging factor of 0.868.
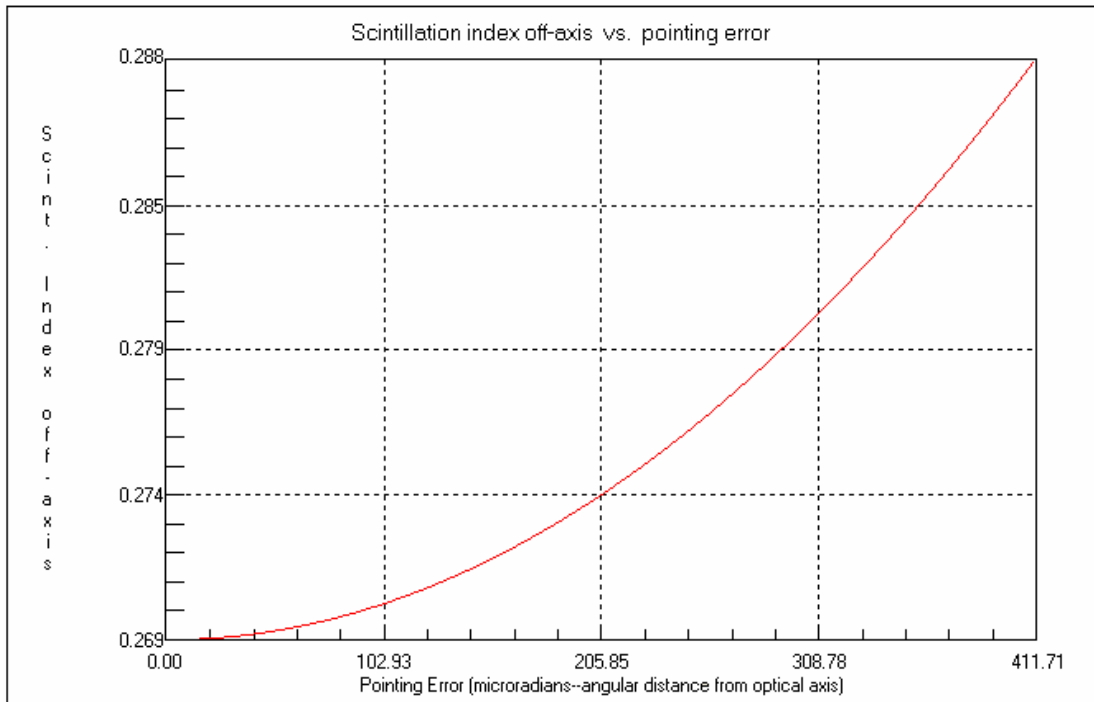
Figure 5.14 Off-axis scintillation index versus pointing error for an 8 *km* UAV altitude with a 10 *μm* wavelength.

The scintillation simulation data corresponds to the expected theoretical model, in which the scintillation index decreases for longer wavelengths. The simulation software used is unable to take altitude into account, so measured values for scintillation would be expected to be lower than those calculated in the simulation. Based on the values, all three of the wavelengths used for a wavelength diversified FSO ground-to-UAV communications link would not be sufficiently affected by scintillation in order to introduce a large enough probability of fade to affect the performance of the link.

5.3.3 Intensity Variance

In this section, the total variance of laser beam intensity is analyzed as a function of radial distance from the optical axis. The total variance of intensity is defined as the product of the scintillation index and the square of the mean intensity of the laser beam.

The total variance of intensity versus pointing error for the 0.85 μm simulation run with a UAV altitude of 4 km is shown in Figure 5.15.
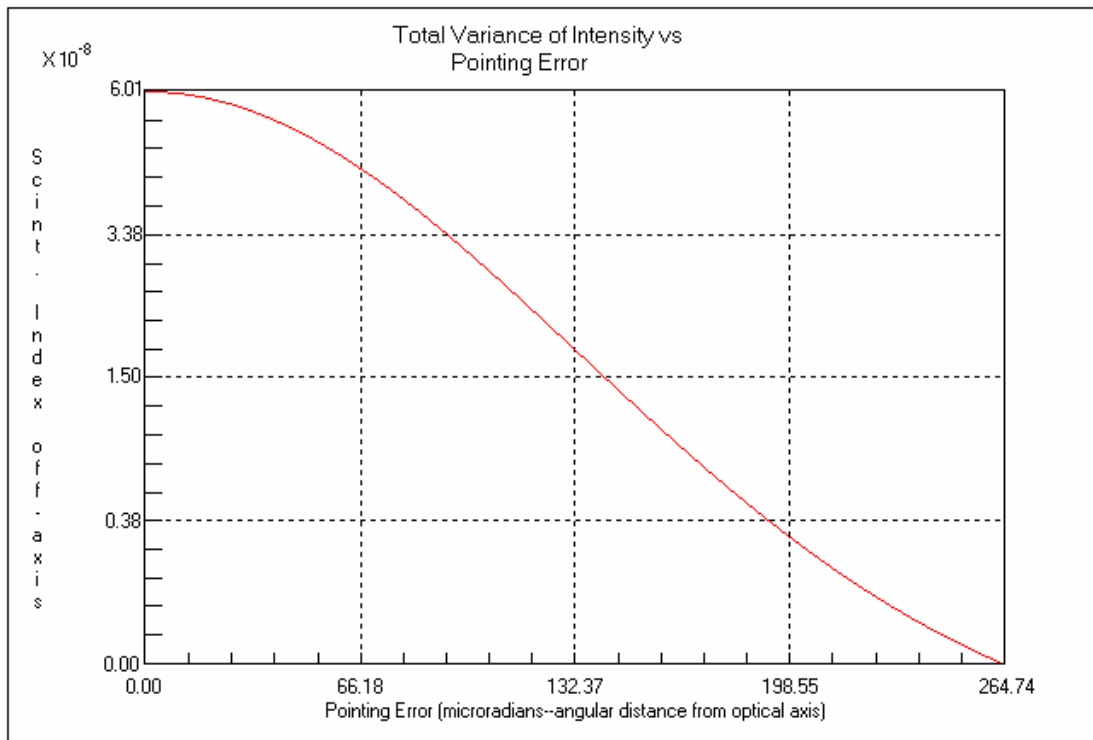
Figure 5.15 Total variance of intensity versus pointing error for a 4 km UAV altitude with a 0.85 μm FSO wavelength.

It can be observed in the plot that for this simulation configuration, the variance of intensity is 6.01×10^{-8} on the optical axis at the receiver plane of the FSO communications link. The corresponding plot of the 8 *km* UAV altitude is shown in Figure 5.16. The variance of intensity was calculated to be 9.71×10^{-9} on the optical axis.
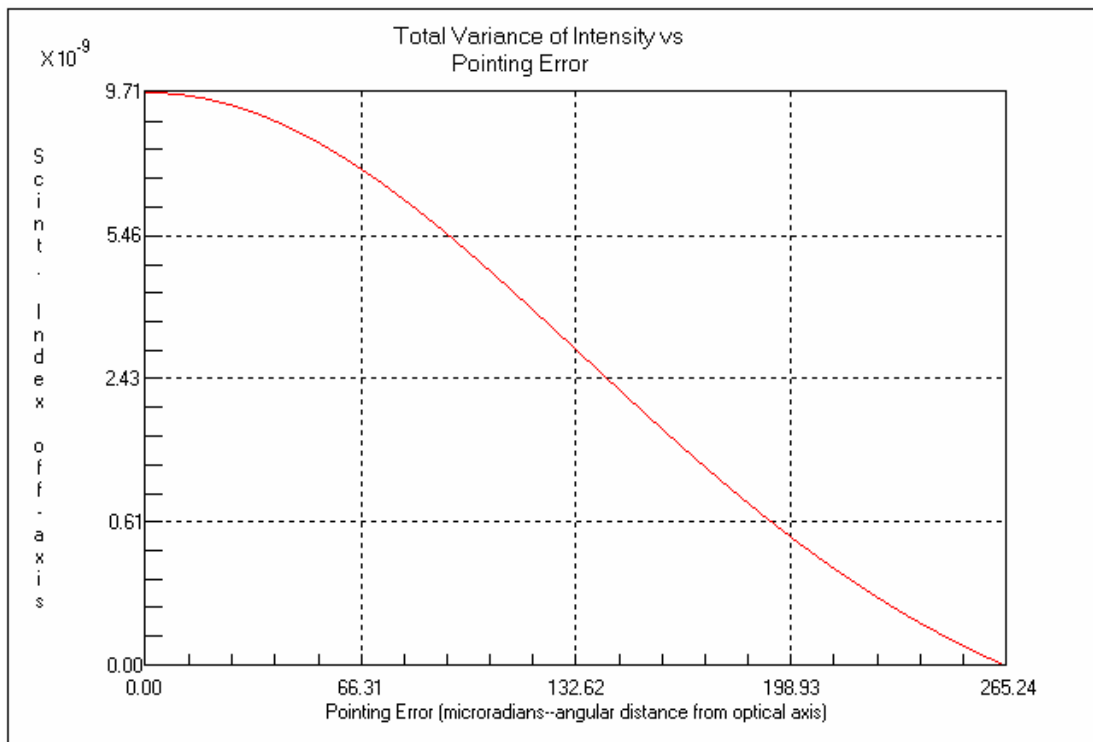
Figure 5.16 Total variance of intensity versus pointing error for an 8 *km* UAV altitude with a 0.85 *μm* FSO wavelength.

Figure 5.17 shows the total variance of intensity versus pointing error for the 1.55 *µm* FSO communications link with a 4 *km* UAV altitude, the variance of intensity was found to be 3.64×10^{-8} on the optical axis.
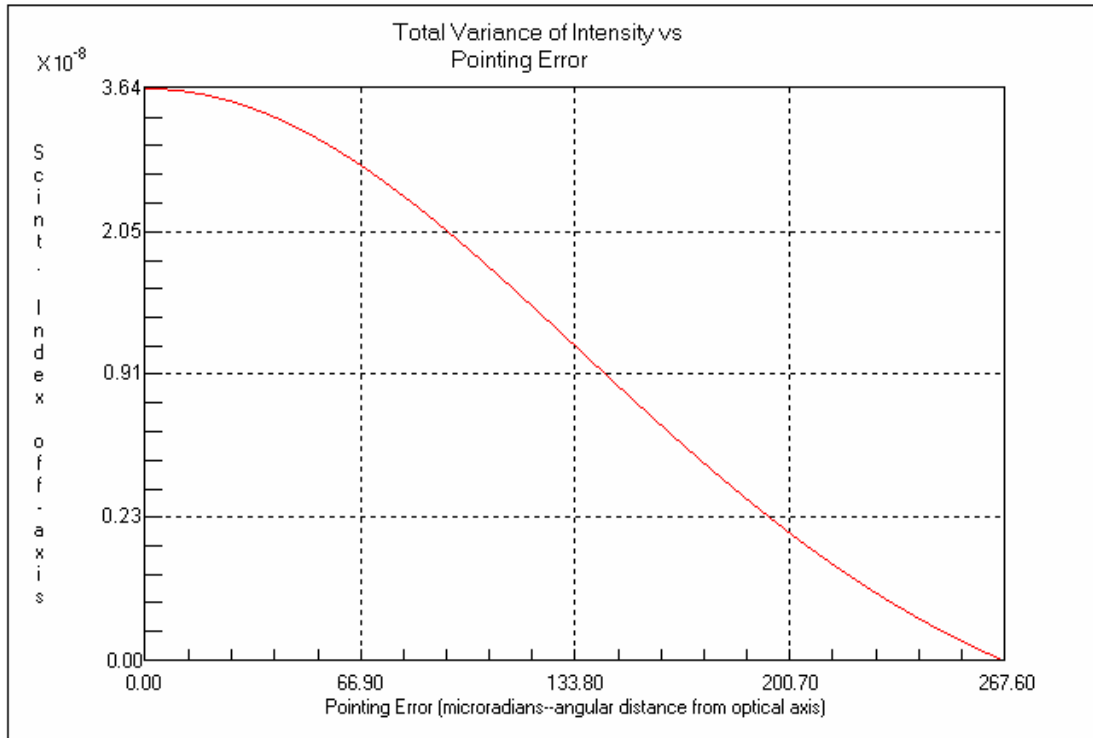
Figure 5.17 Total variance of intensity versus pointing error for a 4 *km* UAV altitude with a 1.55 *µm* FSO wavelength.

Figure 5.18 shows the corresponding 1.55 *µm* wavelength plot for the 8 *km* UAV altitude. The on-axis total intensity variance for this simulation run was found to be 7.22×10^{-9}.
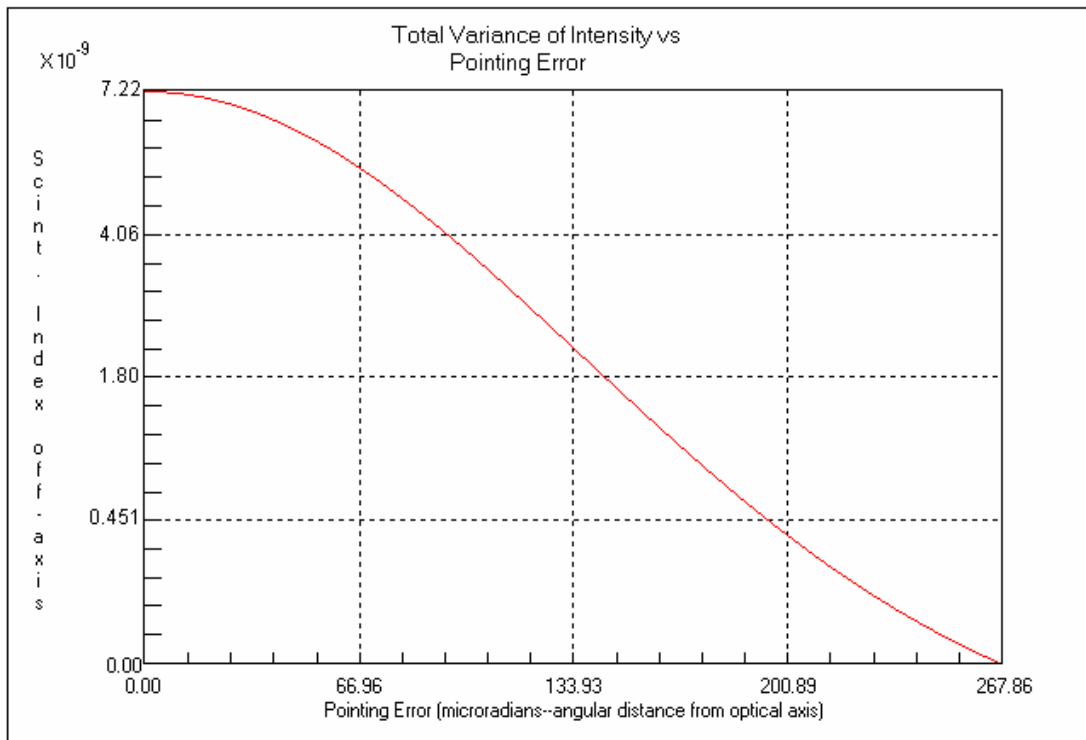
Figure 5.18 Total variance of intensity versus pointing error for an 8 *km* UAV altitude with a 1.55 *μm* FSO wavelength.

The 10 *μm*, 4 *km* UAV altitude FSO link data for total variance of intensity versus pointing error is shown in Figure 5.19. A variance of intensity of 7.51×10^{-10} is predicted to occur along the optical axis of the FSO communications link.
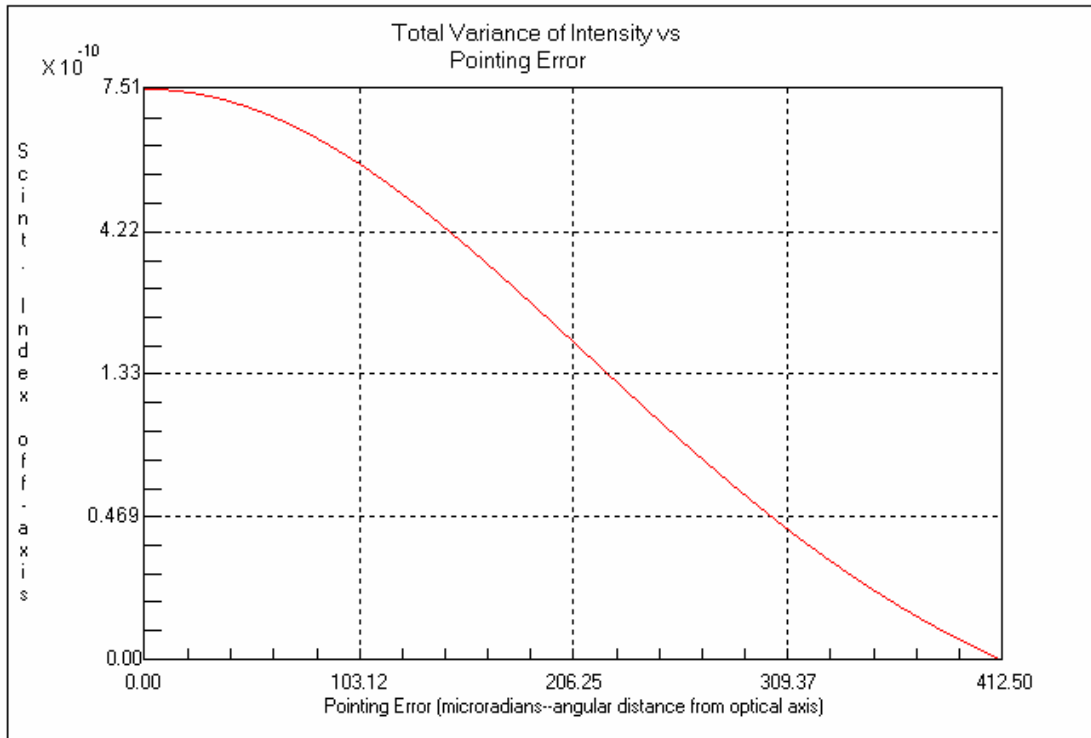
Figure 5.19 Total variance of intensity versus pointing error for a 4 *km* UAV altitude with a 10 *μm* FSO wavelength.

The final plot for this simulated data run showing the total variance of intensity versus pointing error for the 8 *km* UAV altitude with the optical elements operating at 10 μm is shown in Figure 5.20. For this FSO link configuration, the on-axis total variance of intensity is calculated to be 2.32×10^{-10}.
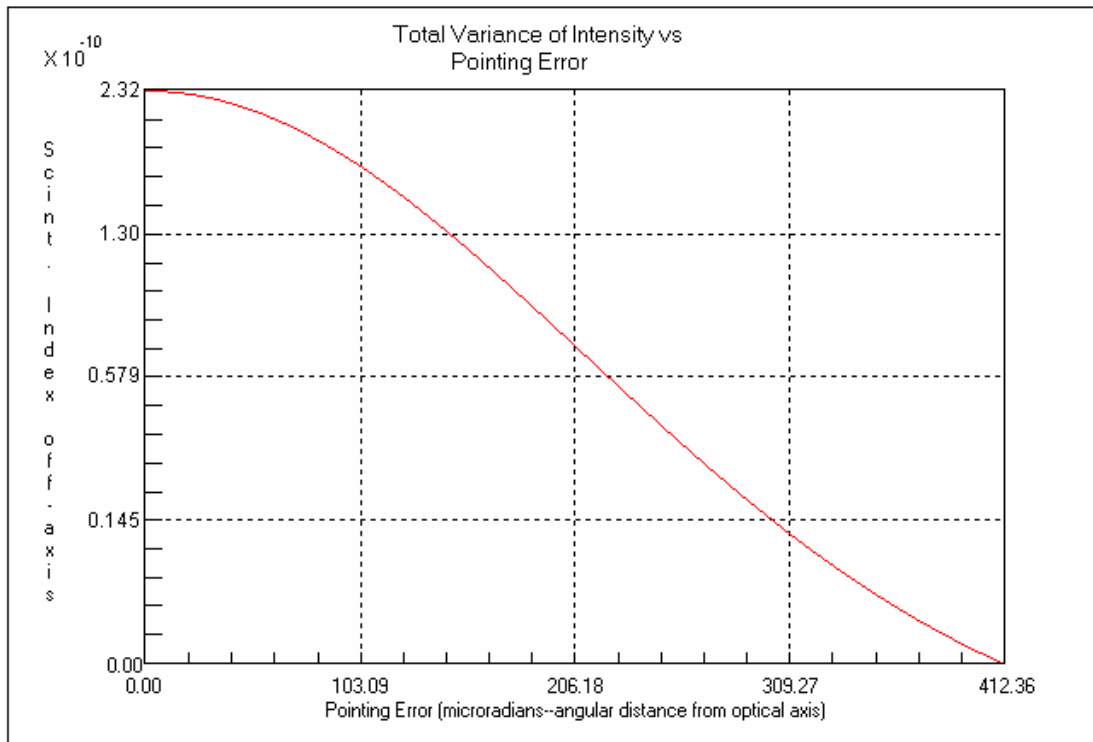
Figure 5.20 Total variance of intensity versus pointing error for a 4 *km* UAV altitude with a 10 *μm* FSO wavelength.

5.3.4 Scintillation index versus square root of Rytov variance

The scintillation index versus square root of Rytov variance data shows the scintillation index as a function of the strength of turbulence parameter $\sigma_1 = \sqrt{1.23 C_n^2 k^{7/6} L^{11/6}}$, where L is the propagation path length.

Figure 5.21 shows a plot of the scintillation index as a function of turbulence for a 4 *km* UAV altitude with a 0.85 *μm* FSO wavelength. The portion of the plot labeled,

"Scintillation index on-axis before aperture averaging" is the scintillation index versus the strength of the turbulence parameter, σ_1 (also known as the square root of the Rytov variance). It should be noted that the Rytov variance represents the normalized irradiance variance, or scintillation index, of an unbounded plane wave in weak fluctuations, but is otherwise considered a measure of optical turbulence strength when extended to strong fluctuations [30]. The horizontal line represents the path length of the FSO link used in the input parameters, and the vertical line indicates the strength of turbulence for this range.
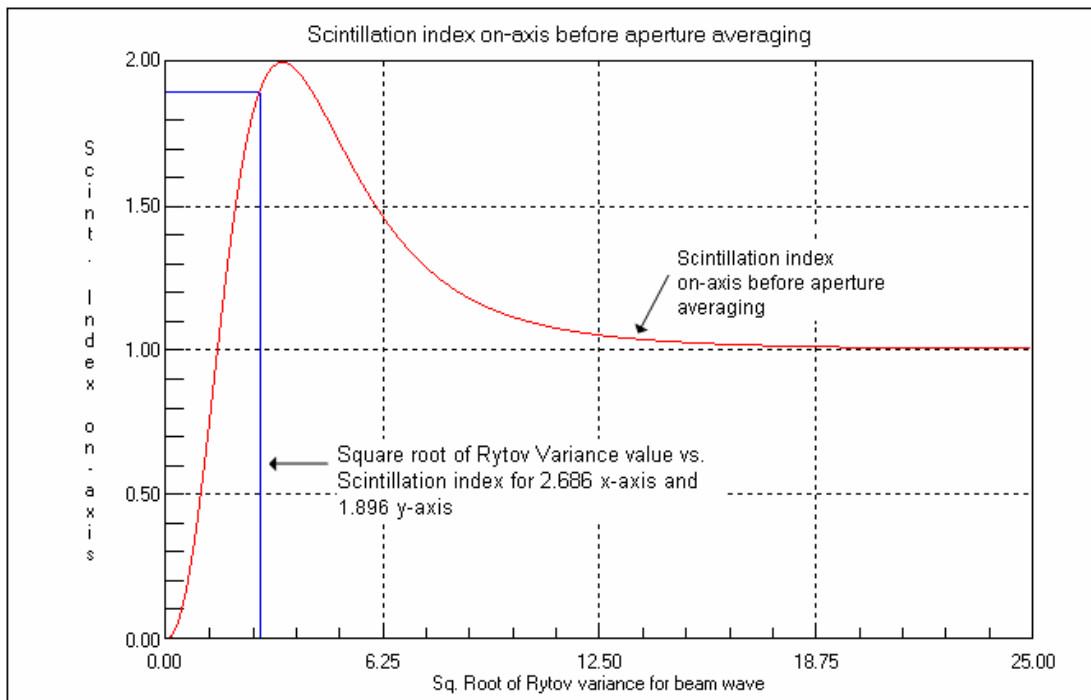
Figure 5.21 Scintillation index as a function of turbulence for a 4 *km* UAV altitude with a 0.85 *μm* FSO wavelength.

Figure 5.22 shows the corresponding plot at 0.85 *µm* but with an increased path length due to the higher UAV altitude of 8 *km*. A comparison between this data and that of Figure 5.21 shows that the increased path length has caused only a minimal increase in the strength of turbulence for this range (the vertical line). The strength of turbulence increased from 1.896 for the 4 *km* altitude to 1.922 for the 8 *km* altitude.
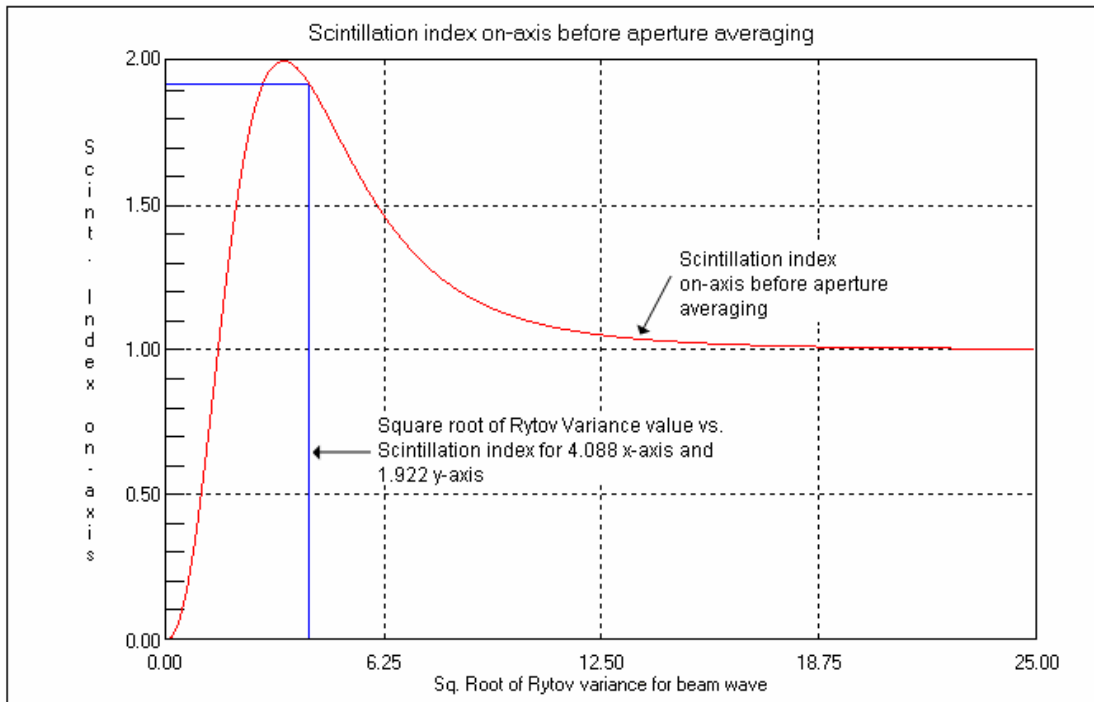
Figure 5.22 Scintillation index as a function of turbulence for an 8 *km* UAV altitude with a 0.85 *µm* FSO wavelength.

Figure 5.23 shows a plot of the scintillation index as a function of turbulence for the 4 *km* altitude UAV with the wavelength increase to 1.55 *µm*. As is expected due to

operation now occurring at a longer wavelength, the on-axis scintillation index has decreased. A comparison to Figure 5.21 shows that for the same UAV altitude, the strength of turbulence for the specified range has decreased from 1.896 to 1.189.
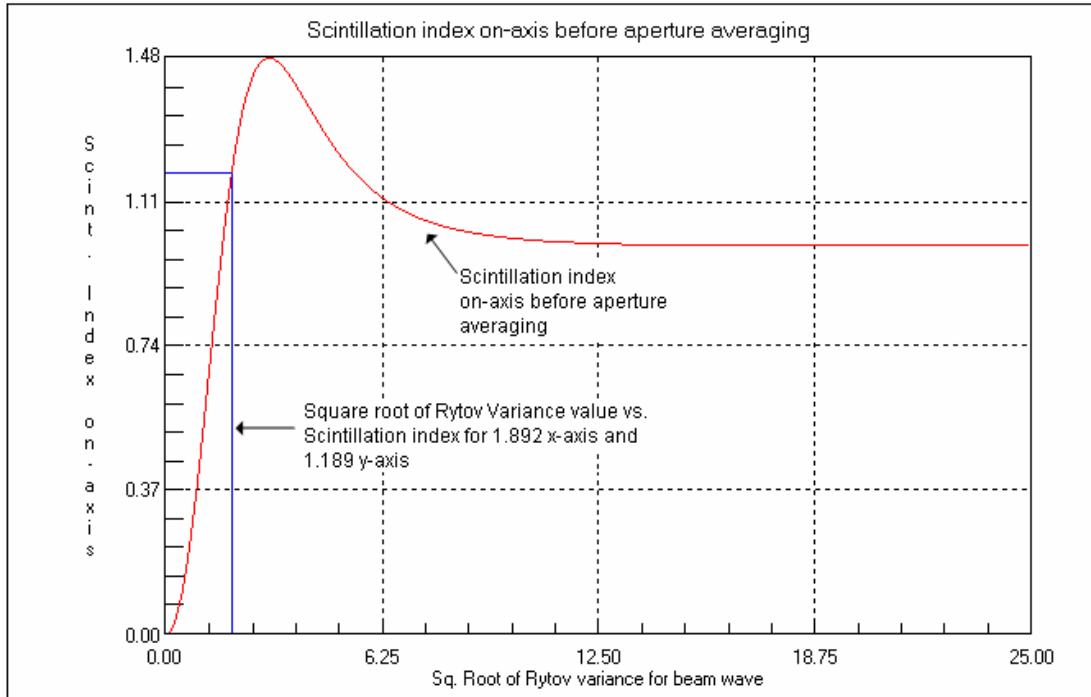
Figure 5.23 Scintillation index as a function of turbulence for a 4 *km* UAV altitude with a 1.55 *μm* FSO wavelength.

Figure 5.24 shows the corresponding 1.55 *μm* plot for the 8 *km* UAV altitude. As is expected, the increased path length causes and increase in the on-axis scintillation, as well as an increase in the strength of turbulence for the specified range from 1.189 for the 4 *km* UAV altitude to 1.486 for this data set. Compared to the data in Figure 5.22,

there is, however, the same expected decrease in both scintillation and strength of turbulence for the longer wavelength.
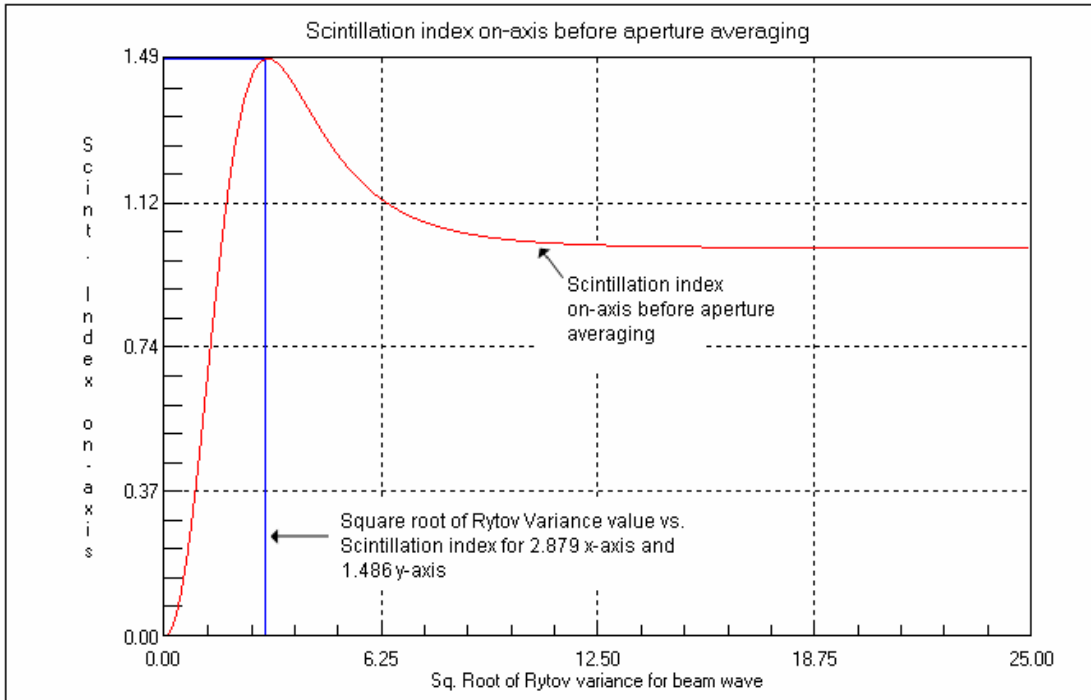
Figure 5.24 Scintillation index as a function of turbulence for an 8 *km* UAV altitude with a 1.55 *μm* FSO wavelength.

The scintillation index as a function of turbulence for the 10 *μm*, 4 *km* FSO communications link is shown in Figure 5.25. With the increase to this far longer wavelength, a large decrease in the on axis scintillation and strength of turbulence parameter is experienced. The strength of turbulence parameter for this link configuration has decreased from a high of 1.896 for the 0.85 *μm* FSO communications link to only 0.139 for the 10 *μm* data set.

136
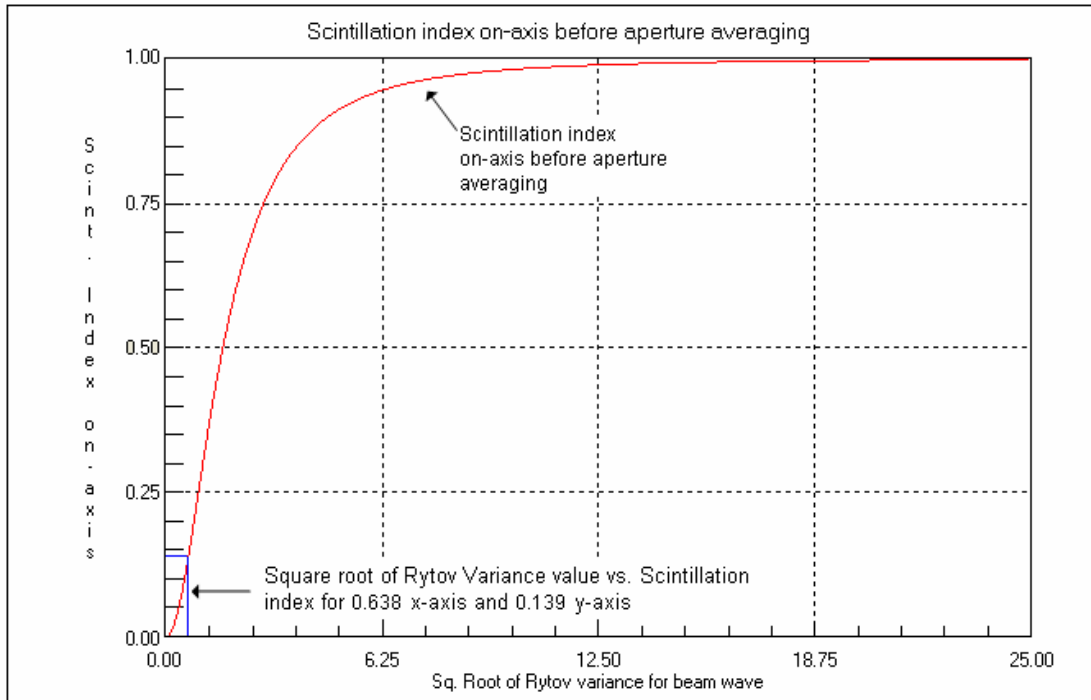
Figure 5.25 Scintillation index as a function of turbulence for a 4 *km* UAV altitude with a 10 *μm* FSO wavelength.

The final plot in this section is of the corresponding data for the 8 *km* UAV altitude and is shown in Figure 5.26. As was the case for the shorter wavelengths discussed in this section, an increase in the strength of turbulence parameter has occurred compared to the shorter FSO link. Also, as was expected, a decrease in the strength of turbulence parameter and scintillation index when compared to the same path length FSO links for shorter wavelengths has occurred.
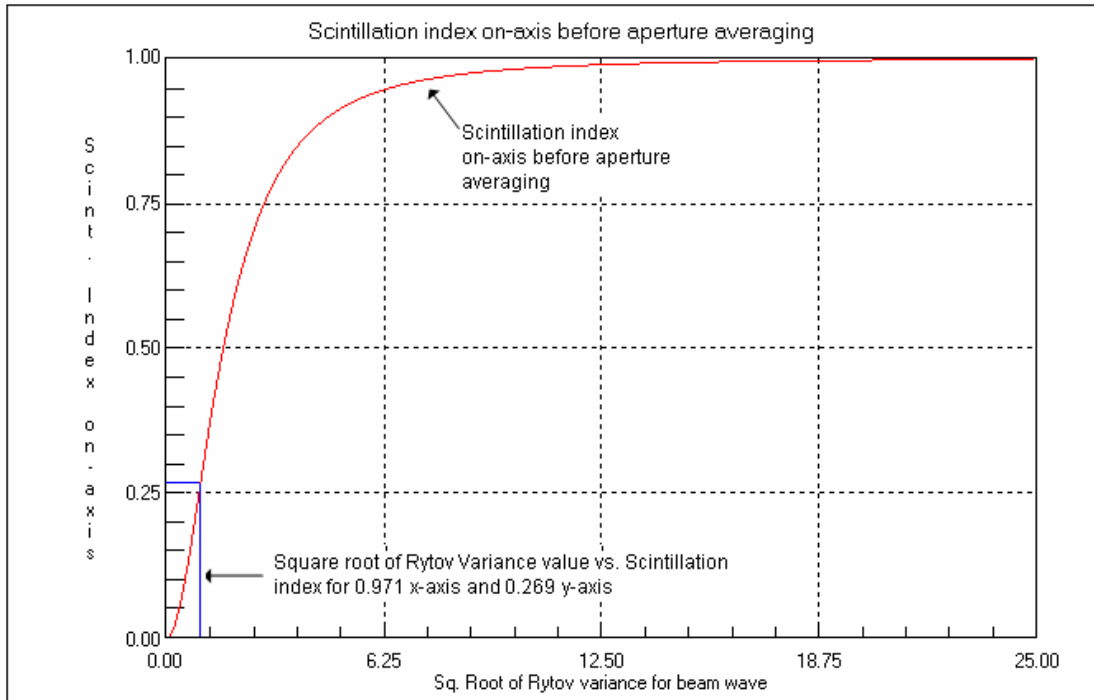
Figure 5.26 Scintillation index as a function of turbulence for an 8 *km* UAV altitude with a 10 *μm* FSO wavelength.

5.4   Proposed Wavelength Diversity Alignment Scheme

In this section, a link acquisition protocol will be described that makes use of multiple wavelengths in order to improve the link acquisition capabilities of the ground-to-UAV FSO communications link. The use of multiple wavelengths simultaneously for link acquisition should increase the efficiency of the link acquisition protocol by allowing for different beam profile spot sizes to simultaneously search for either the

UAV or the ground station. Figure 5.27 shows a view of the proposed link acquisition protocol which will be discussed in detail following the figure.

Phase 1: UAV initiates acquisition sequence

UAV gimbaled transmitter initiates raster scan of 15 m x 15 m square around GPS coordinate of ground station at 0.85 μm, 1.55 μm and 10 μm wavelengths. Transmitter continually sends flight information including altitude, turning radius and flight speed. Each point in the raster scan has a unique identifying code.

Ground station receiver is in stare mode to identify location of UAV

Phase 2: Ground station initiates acquisition sequence

UAV transmitter enters stare mode, while continuously raster scanning the 15 m × 15 m ground station grid.

Ground station initiates raster scan based on flight information obtained from UAV in phase 1. Ground station continually transmits identifying code at which it received flight information from UAV.

Phase 3: UAV locks onto ground station

Based on identifying code received from the ground station in phase 2, UAV locks onto ground station. UAV continues to transmit flight information to ground station. At the same time, the receiver stays in stare mode, waiting for acquisition acknowledgement from the ground station, at which point a receipt signal is issued.

Ground station continues raster scan based on UAV flight path information it is continually receiving. A "position located" signal is continually transmitted. When UAV receives "position located" signal, an acknowledgement is sent. Both transceivers then locked.

Figure 5.27 Overview of link acquisition protocol.

The proposed link acquisition protocol has been divided up into three different phases. In phase 1, the UAV initiates the link acquisition protocol. Because the initial overview of a ground-to-UAV FSO communications link is one in which a stationary ground station is assumed, the UAV's would have prior knowledge of the ground station locations, so link acquisition initiation would be the responsibility of the UAV. During phase 1, the UAV would position itself above the ground station and begin its circular flight path. This flight path information would be converted into data which is continuously transmitted from the UAV's FSO transmitter. In the proposed wavelength diversity scheme, this information will be simultaneously transmitted using three wavelengths. This simultaneous transmission is known as equal gain diversity. The ground station that is expecting a communications from the UAV would be set to enter into a receiver "stare mode" in which the ground station receiver is set to receive data at any of the three wavelengths. Once the UAV is following a circular flight path, the mechanical gimbal will align itself to the GPS coordinates of the ground station and the gimbal will continuously rotate to stay fixed on this position. Because of the error associated with the GPS coordinates for both the UAV and the ground station, a search algorithm is necessary. For this proposed protocol, a raster scan of a 15 m × 15 m area surrounding the ground station is proposed. The FSM embedded in the FSO transmitter is used to rapidly perform the raster scan. Each time the FSM moves the laser beam to the next scanning position, a unique identifying code is sent along with the flight data information. A view of the

proposed raster scan showing each of the three overlapping beam profiles is shown in

Figure 5.28.
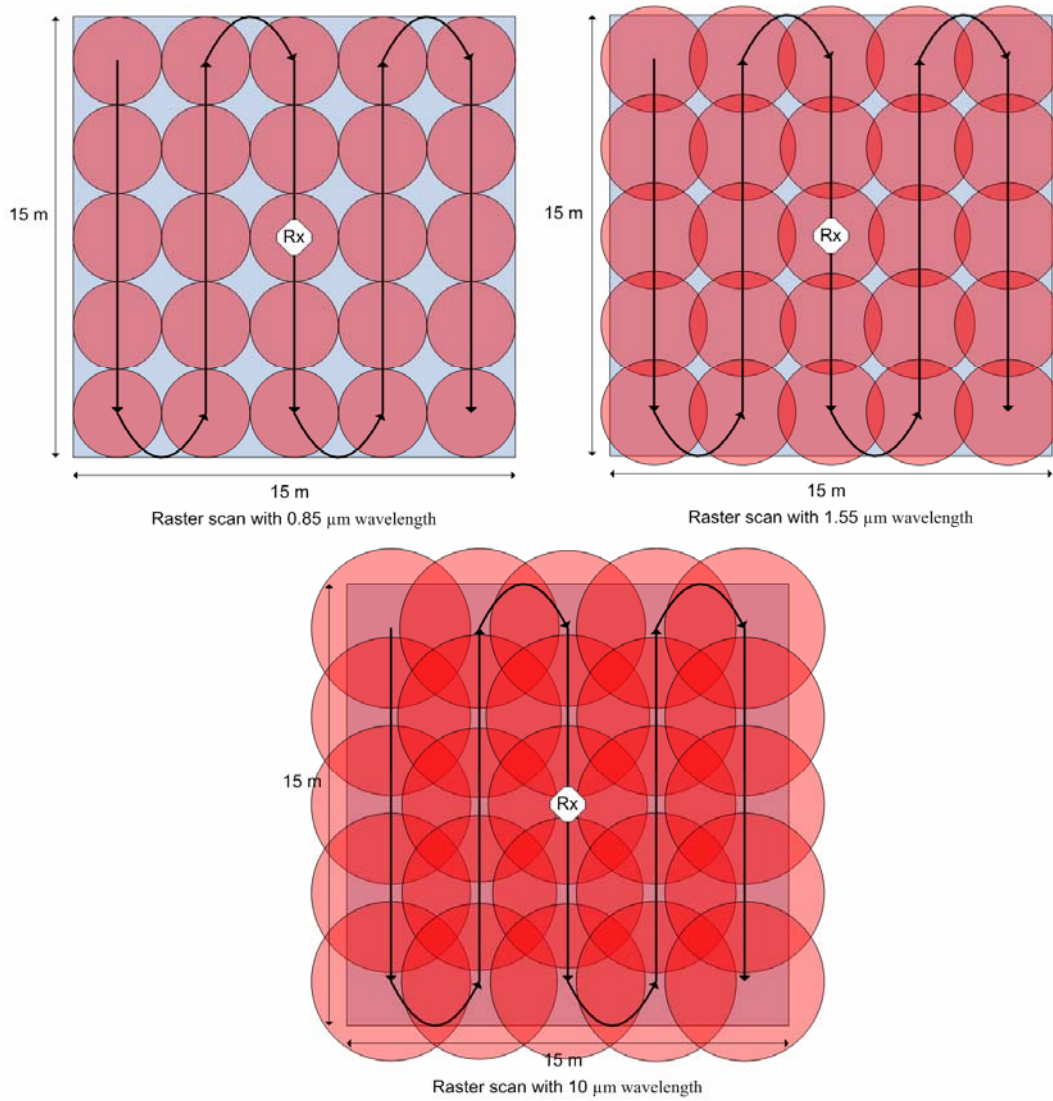
Figure 5.28 Raster scan for the proposed alignment protocol.

In Figure 5.28, the raster scan for each of the three wavelengths has been shown on a separate image, but for the alignment protocol, these wavelengths will be overlapping each other. While the ground station is in stare mode, when the FSO link is in a position in which it receives the data, the ground station will record the UAV flight information as well as the unique identifying code for the position in which it received the flight information.

In phase 2, the UAV continues to raster scan the 15 m × 15 m area surrounding the ground station, but after phase 1 in which the flight information was sent to the ground station, the UAV now switches into stare mode. During phase 2, the ground station will begin to use the mechanical gimbal to track the received flight information. At the same time, the ground station FSM will begin to perform a raster scan as the gimbal tracks the flight plan. The ground station will be continuously transmitting the identifying code received from the UAV during phase 1.

In phase 3, after the UAV has received the identifying code from the ground station in phase 2, the UAV will lock and track its FSO unit onto the position received from the ground station. The UAV will continue to transmit its flight information to the ground station on which it should now be locked while simultaneously holding its receiver in stare mode. The ground station will continue to raster scan around the flight path while holding its receiver in stare mode. When the ground station begins to receive the flight information, it will transmit a "position locked" signal to the

UAV, which returns an acknowledgement. At this point, the two FSO units can begin to transmit data.

Based on this proposed alignment protocol, the inclusion of a wavelength diversity scheme can improve the link acquisition sequence. As was depicted in Figure 5.28, the different wavelengths each have a unique beam profile, so a simultaneous use of all three wavelengths will increase the coverage area of the raster scan. A 0.85 μm FSO link covers only 78.3% of the search area; a 1.55 μm FSO link increases the coverage area to 80.1%, and the 10 μm FSO link covers 100% of the search area. The use of three wavelengths will also cause an increased likelihood that at least one of the wavelengths will be able to pass unrestricted through the atmosphere. In Chapter 6, an analysis of the effects of atmospheric weather conditions on each of the wavelengths will be discussed, which will further show the advantages of this proposed wavelength diversity scheme.

5.5 Summary

In this chapter, a detailed analysis of the performance of three different optical wavelengths in the presence of atmospheric turbulence using simulation tools has been performed. It was seen that each of the three wavelengths would perform sufficiently well in the presence of atmospheric turbulence to establish and maintain a connection between the ground station and the UAV. Based on the different

performance parameters of the different wavelengths, a wavelength diversified alignment protocol for the ground-to-UAV FSO communications link was proposed and described. The use of a wavelength diversified FSO transceiver configuration would increase the coverage area that is scanned in the acquisition protocol while simultaneously adding an inherent redundancy to the system by providing three channels for both communications and link acquisition.

Chapter 6

Wavelength Diversity in the Presence of

Atmospheric Weather Conditions

6.1 Introduction

A wavelength diversity scheme to improve the performance of a ground-to-UAV FSO communications link in the presence of different atmospheric weather conditions is presented in this chapter. The wavelength diversity scheme uses the same three wavelengths as the scheme presented in Chapter 5. The scheme is modified to include an equal gain wavelength diversity scheme and a selective wavelength diversity scheme. Different optical wavelengths undergo different amounts of atmospheric loss depending on the prevalent weather conditions present in the troposphere of the atmosphere. Under some weather conditions, such as fog, transmission of FSO signals is virtually impossible in horizontal terrestrial links. The use of a slant path to a UAV also introduces cloud formations into the path between the transmitter and the receiver.

The remainder of this chapter is organized as follows: In Section 6.2, a description of the different weather conditions used in this simulation is discussed. The simulation

configuration is described in Section 6.3. Section 6.4 contains the results obtained from the simulation software, and concluding remarks are presented in Section 6.5.

6.2 Description of Weather Conditions

In this section, the various weather conditions used in this simulation will be described. Three different atmospheric weather environments were simulated in order to obtain the data that will be presented in Section 6.4. These three weather environments are a clear atmosphere, the atmosphere with the presence of cloud formations and finally the atmosphere in the presence of fog.

The model atmosphere used for all the weather conditions was the 1976 U.S. Standard Atmosphere. The 1976 U.S. Standard Atmosphere model is the result of the formation of the United States committee on Extension to the Standard Atmosphere (COESA) which was formed to assemble information on atmospheric parameters at altitudes traversed by suborbital rockets. This effort resulted in a mid-latitude (45ºN) mean atmospheric profile that was published in the U.S. Standard Atmosphere, 1962. The 1976 U.S. Standard Atmosphere is identical to the 1962 model for altitudes lower than 50 *km*, but different for higher altitudes [58]. For the clear atmosphere, the aerosol model used is a rural extinction with a default visibility of 23 *km*. The clear atmosphere simulation run was performed in order to provide a baseline data set for comparison to the other weather conditions simulated.

The simulations of FSO transmission to a UAV with the presence of cloud formations consisted of two different cloud formations. The first simulation was for cumulus clouds with a base at an altitude of 660 *m* and the top of the cloud and an altitude of 3.0 *km*. Cumulus clouds are low-level, flat-bottomed puffy clouds that usually display a noticeable vertical development. Cumulus cells can either be isolated, or can form a group of clouds [59]. The second simulation was run for altostratus cloud formations. Altostratus clouds are mid-level clouds. Both cumulus and altostratus clouds may contain ice crystals and/or water droplets. Altostratus clouds tend to form with a more uniform and diffuse coverage where it is difficult to detect individual elements of features of the clouds [59]. The simulated altostratus clouds are set to have a base height of 2.4 *km* and a top height of 3.0 *km*. The detailed cloud properties of both cloud formations used in the simulation are defaulted to follow the 1976 U.S. Standard Atmosphere model. These detailed cloud properties are the cloud thickness, base altitudes, extinction coefficients, boundary altitudes, spectral data points, liquid water droplet densities, ice particle densities, relative humidity, liquid water Henyey-Greenstein Phase functions and ice particle Henyey Greenstein phase functions. The two cloud formations were selected because the formations cover both a low-level cloud formation and a mid-level formation which are two configurations where the UAV flight altitude would be at a higher level than the cloud formation.

The fog configuration for the simulation also consisted of two different types of fog, namely advection and radiation fog. As was explained in Chapter 2, fog is by far the

most detrimental weather phenomenon for FSO transmission. Both advection and radiation fog form over land. Radiation fog forms when temperatures drop to near the dew point temperature of the atmosphere. This causes water vapor present in the atmosphere to condense. A standard setting for radiation fog is a visibility of 500 m. Advection fog forms when air pockets with different temperatures in the atmosphere mix. This often occurs when warm, moist winds enter into a cooler air pocket. The water vapor present in the warm air pocket condenses and forms a very thick fog. Advection fog has a commonly used visibility of only 200 m.

6.3   Simulation Configuration

The simulation for the data presented in this chapter was obtained using PcModWin atmospheric software. PcModWin is a graphical environment that allows for the configuration, manipulation and running of model calculations that are performed by the MODTRAN atmospheric code. MODTRAN is a DOS-based atmospheric simulation code that was developed by the Air Force Research Laboratories [60].

PcModWin allows a user to calculate transmittance data for a user-defined range of wavelengths in one of three configurations. The configurations allowed are a horizontal path, a slant path and a slant path to space. The link is simulated as an omni-directional link. For the data calculated in this simulation, a slant path was used. The slant path allows an observer height (defined as the height of the laser

transmitter), a final height (the height at which the transmittance is measured) and a zenith angle between the two heights to be defined. This configuration is shown in Figure 6.1.
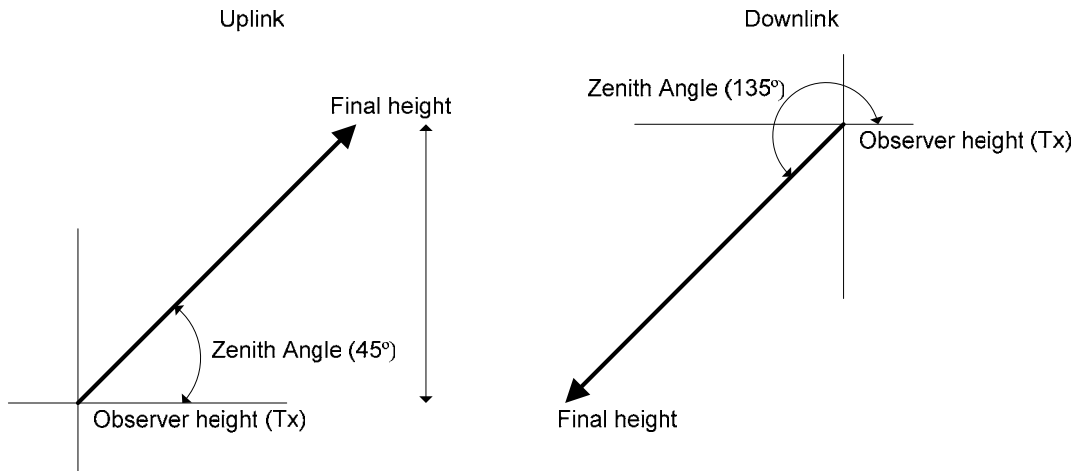
Figure 6.1 Configuration of uplink and downlink for PcModWin simulation.

The software was configured to calculate the transmittance for a range of wavelengths extending from 0.8 μm to 10.2 μm. This range was selected to include the three wavelengths that are considered for the wavelength diversity scheme, 0.85 μm, 1.55 μm and 10 μm. In order to obtain data using PcModWin, multiple executions of each simulation configuration are required. Each execution is run with a different value for the final height of the FSO communications link. Through this process, a detailed analysis of each wavelength's transmittance properties can be obtained.

For the analysis of the received power for each different FSO communications link configuration, the transmitter was configured to have an output power of 20 *mW* for each wavelength. The optical loss present in the link is assumed to be -3 *dB*, the pointing loss is assumed to be -10 *dB* and the geometric loss is assumed to be -18.7 *dB*. The geometric loss is calculated using the data presented in Chapter 4. The loss taken is the largest loss present in any of the three wavelength configurations used in Chapter 4. The receiver threshold, which is the minimum detectable signal by the FSO receiver, was set at -43 *dBm*. From these loss values, it is calculated that in order for a usable signal to arrive at the receiving end of a ground-to-UAV FSO link, the received power must be greater than -11.3 *dBm*.

6.4 Results

The results obtained from the PcModWin simulation will be discussed in three different sections, corresponding to the three different weather phenomena described in Section 6.2.

6.4.1 23 km Visibility in the Absence of Weather Phenomena

The first data set presented in this chapter is that of the FSO communications link in clear weather for the 1976 U.S Standard Atmosphere Model. The first data discussed

will be for a ground-to-UAV uplink, and then two separate discussions for the corresponding ground-to-UAV downlink.

Figure 6.2 shows the transmittance profile for the ground-to-UAV FSO communications uplink for a UAV altitude of 4 *km*.
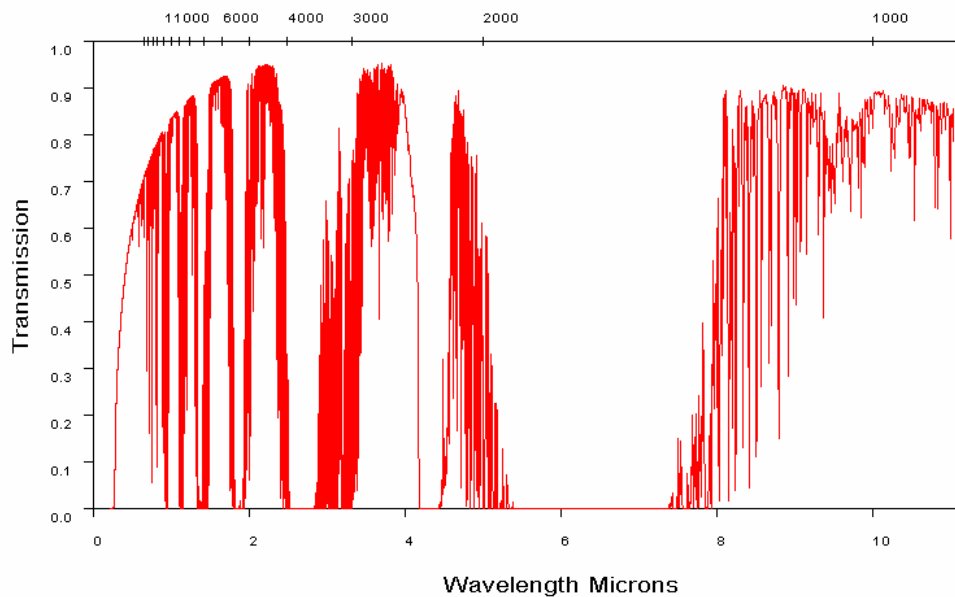
Figure 6.2 Transmittance as a function of wavelength for a 4 *km* UAV altitude.

The corresponding plot for an 8 *km* UAV altitude is shown in Figure 6.3. A comparison of the two transmittance plots shows that under clear weather conditions, there is little noticeable difference in the amount of transmittance achievable at the two UAV altitudes.
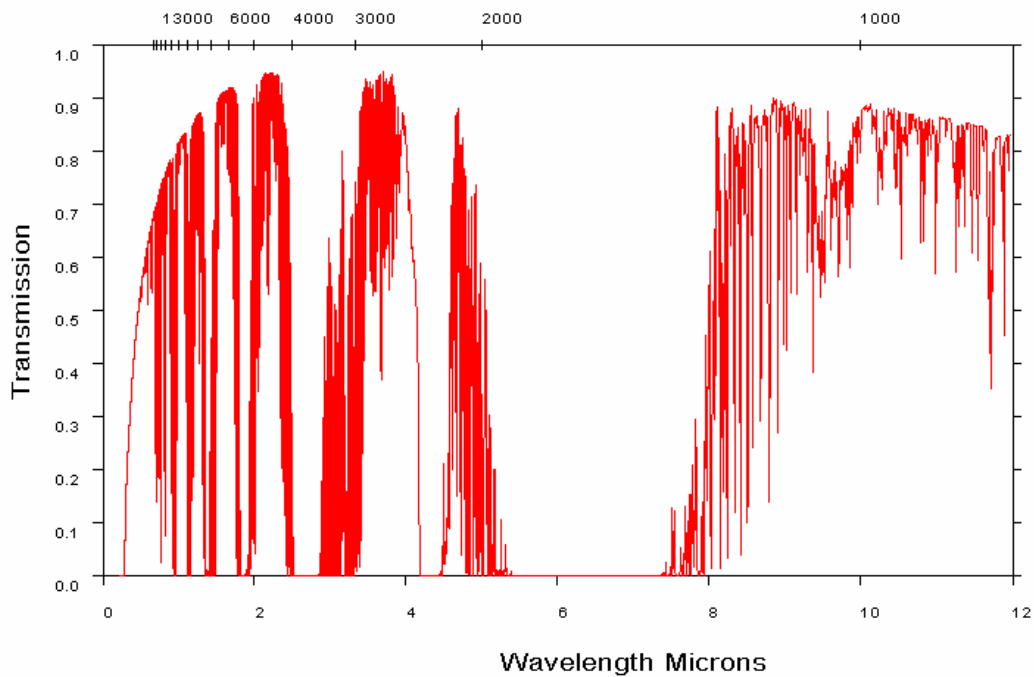
Figure 6.3 Transmittance as a function of wavelength for an 8 *km* UAV altitude.

The transmission windows surrounding the three wavelengths of the diversity scheme proposed in this chapter can be seen in Figures 6.2 and 6.3. From the data used to generate these transmittance plots, a detailed view of the three wavelengths performance under these clear atmospheric weather conditions was created. Figure 6.4 shows a plot of transmittance as a function of UAV altitude for an FSO communications uplink.
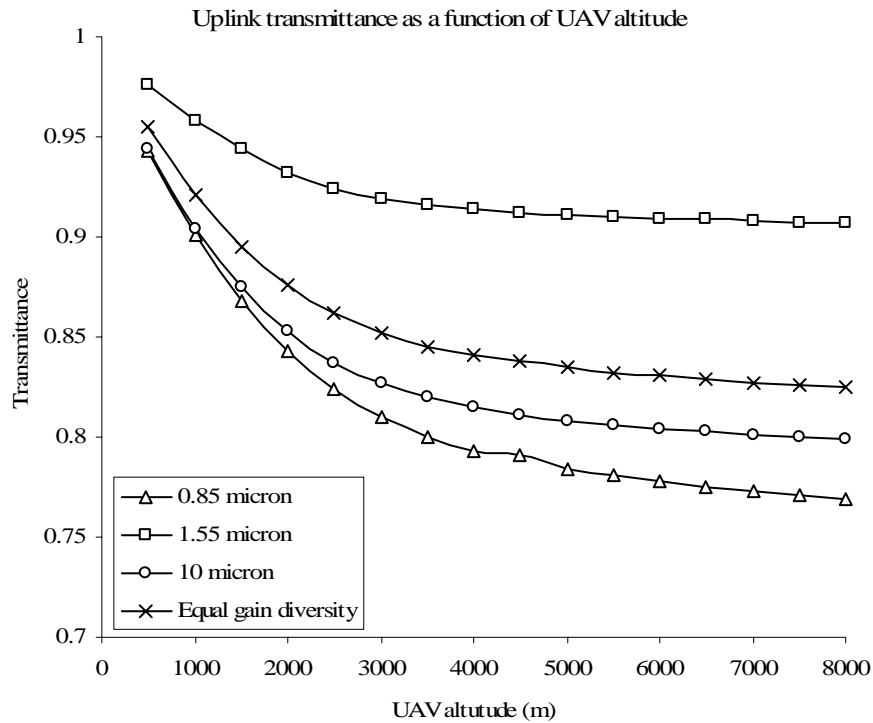
Figure 6.4 Uplink transmittance as a function of UAV altitude.

The data used to generate this plot and all of the other plots showing the wavelength diversity data is recorded in Appendix B. An analysis of Figure 6.4 shows that under clear atmospheric weather conditions, the 0.85 μm wavelength undergoes the most significant loss, while the 1.55 μm wavelength experiences the least amount of loss. The data obtained for the ground-to-UAV uplink shows that for the 0.85 μm wavelength, the transmittance with an 8 km UAV altitude was 76.95%. The plot also contains data for an equal gain diversity scheme. In equal gain diversity, the signal powers received by the detectors are summed after demodulation. The transmitter output power is therefore divided equally into three and each part is transmitted on a

single wavelength. An alternative approach for a diversity scheme is to use selective diversity, in which the strongest of the three signals is selected by the transmitter. It can be seen in this plot that the use of a selective diversity scheme would be the best in clear weather, because the 1.55 *μm* wavelength shows a transmission of 90.69% with a UAV altitude of 8 *km* compared to only 82.5% for an equal gain diversity scheme.

For a more useful interpretation of the transmittance data, it is necessary to view the received power of each individual wavelength as well as that of the equal gain diversity scheme. Figure 6.5 shows a plot of the received power at the UAV receiver as a function of UAV altitude for the FSO uplink. The plot does not show the receiver threshold due to the difficulty associated with displaying both the received powers and the receiver threshold clearly on the same plot. The receiver threshold of -11.32 *dBm* takes into account both optical geometric losses, so the threshold is set at a level that allows for the determination of link connectivity based solely on atmospheric losses. It is clearly visible in the plot that in the absence of any prevailing atmospheric weather conditions, all three wavelengths as well as the equal gain diversity scheme are able to overcome any atmospheric loss present in the FSO link.

Received Power as a function of UAV Altitude for uplink
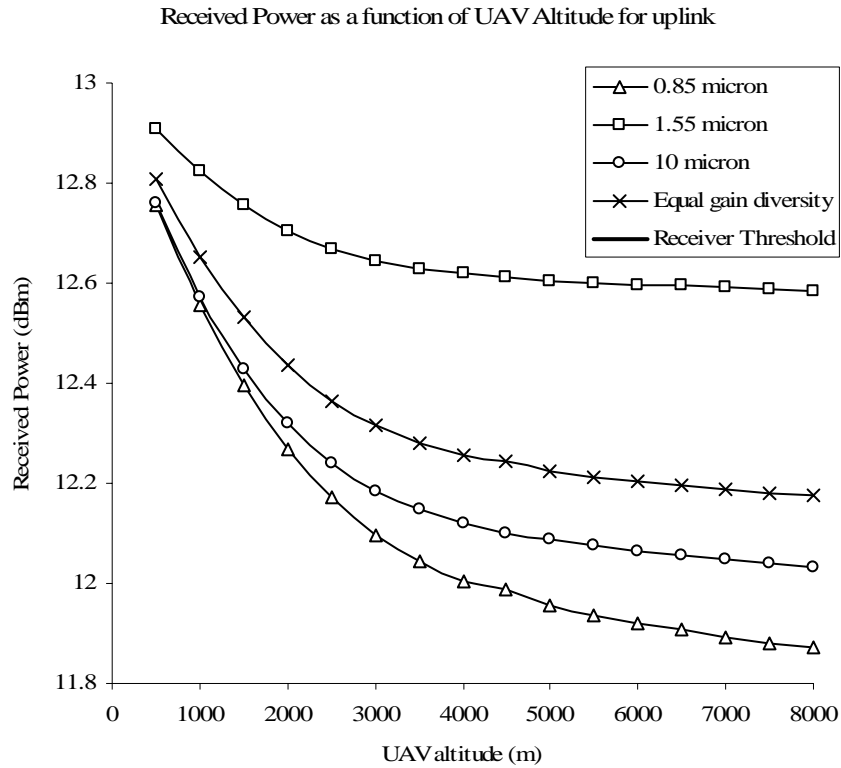
Figure 6.5 Received power as a function of UAV altitude for a ground-to-air uplink.

Because the atmosphere is best modeled as a series of layers, for an FSO communications link that follows a slant-path through the atmosphere, a separate analysis of the FSO uplink and downlink is required. Due to the similarity of the entire transmittance profile for the uplink and downlink, only a detailed view of the performance of the three wavelength diversity scheme will be presented for the downlink data. To remain consistent with the data presented in Chapter 4, downlink data presented will be analyzed for both a UAV altitude of 4 *km* and a UAV altitude of 8 *km* above the ground station. Figure 6.6 shows a plot of the downlink

155

transmittance as a function of altitude above the ground station for a 4 *km* UAV altitude.

Figure 6.6 Downlink transmittance as a function of altitude above ground station with a UAV at 4km altitude
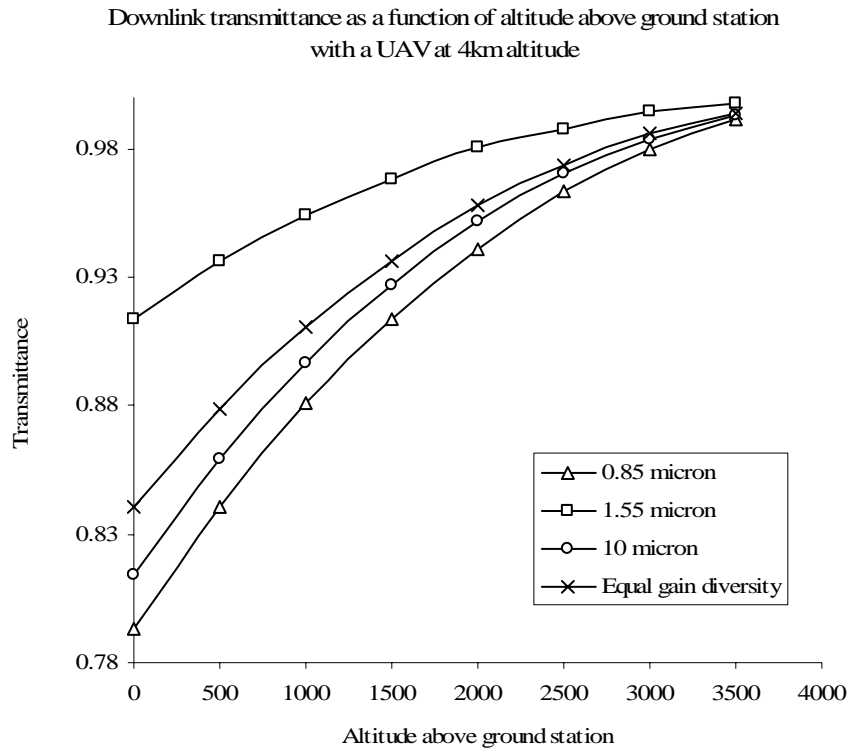
Figure 6.6 Downlink transmittance as a function of altitude above the ground station for

a 4 *km* UAV altitude.

As is expected from the uplink data, the downlink transmittance for each of the three wavelengths as well as the equal gain diversity scheme are all greater than 78%. The 0.85 *μm* wavelength shows the largest amount of atmospheric loss on both the uplink and downlink. Figure 6.7 shows the corresponding plot for an 8 *km* UAV altitude.

Downlink transmittance as a function of altitude above ground station
with UAV at 8km altitude
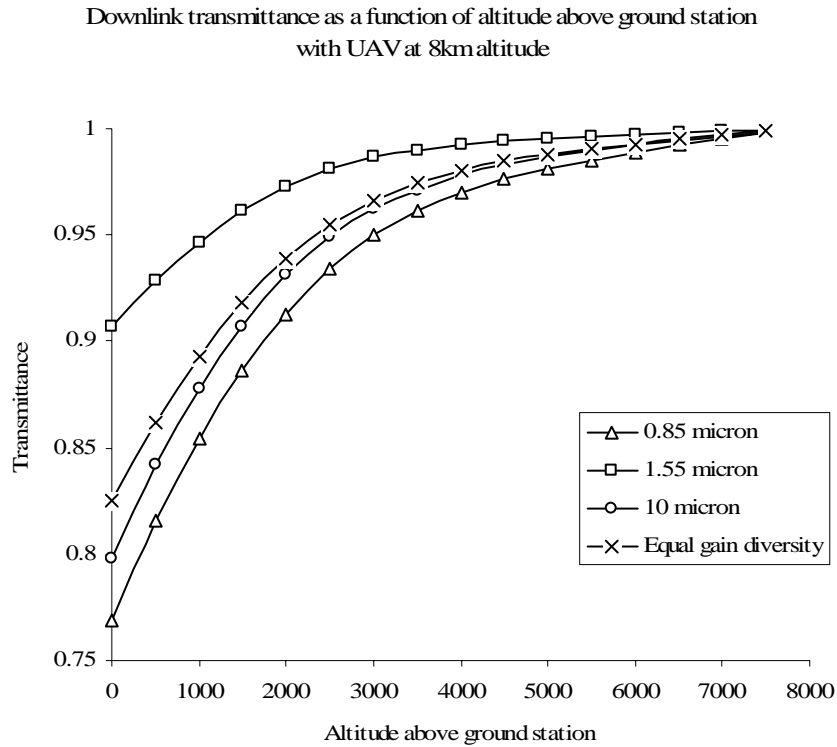
Figure 6.7 Downlink transmittance as a function of altitude above the ground station for

an 8 *km* UAV altitude.

For the 8 *km* UAV altitude, the largest atmospheric loss occurs for the 0.85 *μm* wavelength, where the transmittance at the ground station was measured to be 76.92%. Comparing this value to the FSO uplink shows that there is a slight increase in the amount of atmospheric loss present in the downlink than the uplink. This additional loss in the downlink can be accounted for because the thickness of the atmosphere is greatest closest to the earth's surface, so on the downlink portion of the FSO link, a weaker signal is present when propagating through the thickest portion of the atmosphere.

Figure 6.8 shows a plot of the received power as a function of altitude above the ground station for a UAV altitude of 8 *km*. It is not necessary to show a detailed received power plot of the a 4 *km* UAV altitude because from the transmittance data it can be observed that if the link maintains connectivity for an 8 *km* altitude, the link will maintain connectivity for a 4 *km* altitude.
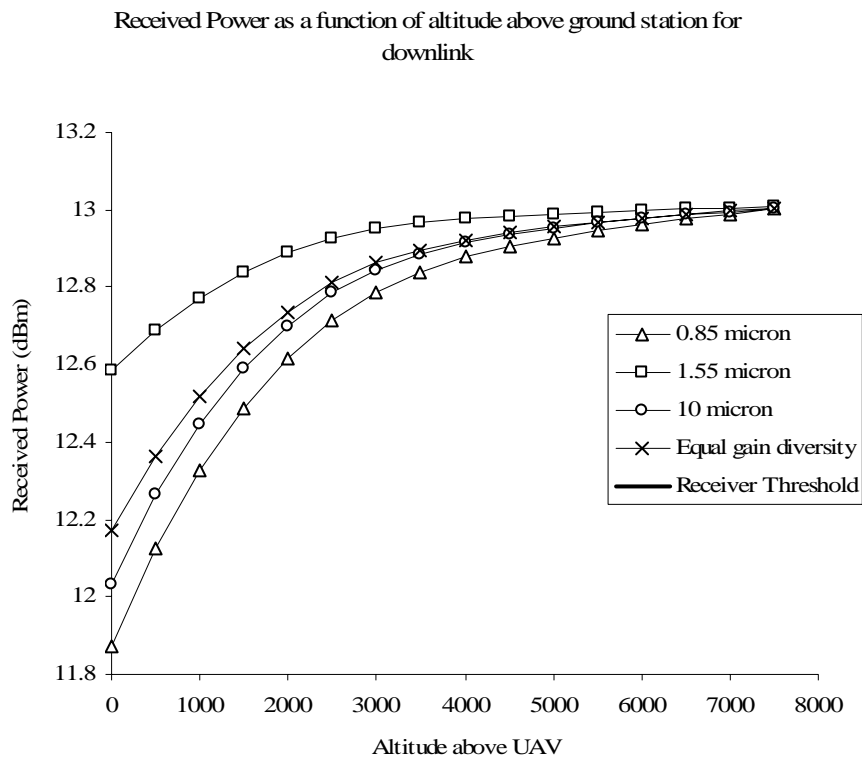
Figure 6.8 Received power as a function of altitude above the ground station for an air-to-ground downlink with an 8 *km* UAV altitude.

As was the case for the ground-to-air FSO uplink, all three wavelengths, as well as the equal gain diversity scheme, do not experience a large enough magnitude of atmospheric loss to prevent a connection between the ground station and the UAV.

6.4.2 FSO Links in the Presence of Cloud Formations

Most research work on terrestrial FSO communications systems focuses on the effects of weather phenomena that are present near to the earth's surface. Because a ground-to-UAV FSO link follows a slant path towards higher altitudes of the earth's atmosphere, weather phenomena such as clouds need to be analyzed in order to verify the links viability.

Figure 6.9 shows a plot of the uplink transmittance for the three wavelengths and the equal gain diversity scheme in the presence of low altitude cumulus clouds. It is observed that transmission of any of the three wavelengths through the cloud is virtually impossible. From the simulation input, the base of the clouds form at an altitude of 660 *m*, but the transmittance data shows that even at an altitude of only 200 *m*, less than 20% transmittance is achievable for any of the wavelengths. At a UAV altitude of 750 *m,* the signal from all three wavelengths will reach a zero transmittance level.

Uplink transmittance as a function of UAV altitude in the presence of
cumulus clouds
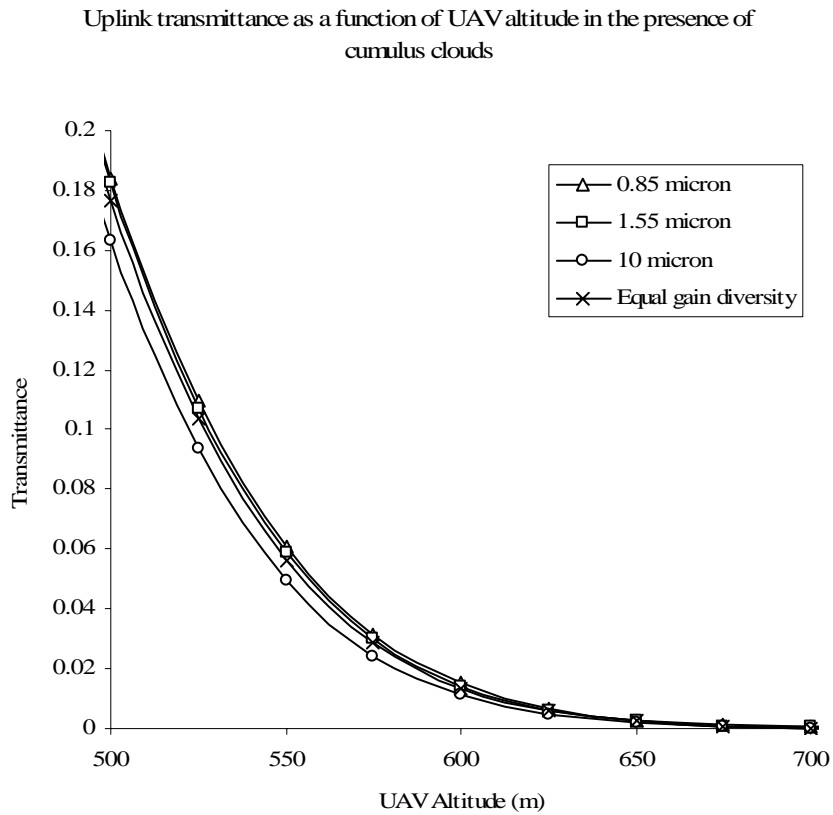
Figure 6.9 Uplink transmittance as a function of UAV altitude in the presence of

cumulus clouds.

The transmittance plot with low-level cumulus clouds shows that FSO transmission
through this type of cloud is impossible to achieve using the three wavelengths of this
diversity scheme.

Figure 6.10 shows the corresponding plot of the received power expected for the
ground-to-UAV uplink in the presence of cumulus clouds. The data presented shows
that the 10 μm wavelength has the poorest performance and the receiver threshold is

exceeded at a UAV altitude of approximately 630 *m*.   The 0.85 *μm* wavelength

exhibits the best performance through the cumulus clouds, but this wavelength can

only penetrate about 10 *m* further into the cumulus clouds.
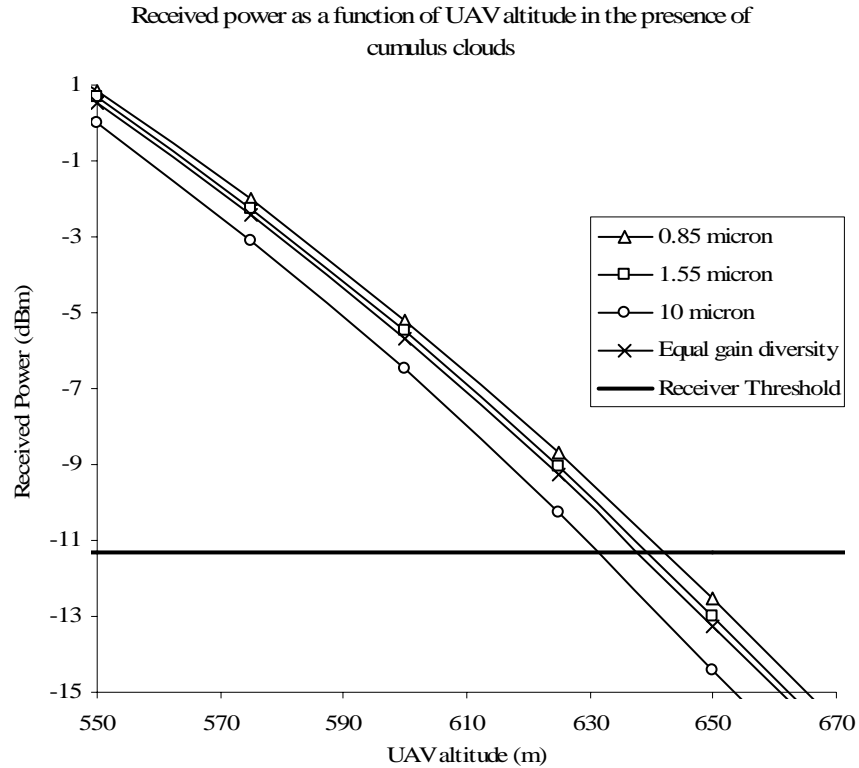
Figure 6.10 Received power as a function of UAV altitude in the presence of cumulus

clouds.

Based on the limited transmission range achievable by a three wavelength diversity

scheme through cumulus clouds, a detailed analysis of the downlink for this

configuration is not necessary because to successfully align and track the link, both

the up and downlink need to be active.

Since it has been shown that FSO transmission using the proposed three wavelength diversity scheme cannot be achieved through low-level clouds, the next weather phenomenon investigated is that of mid-level altostratus clouds. Figure 6.11 shows a plot of the achievable transmittance on a ground-to-UAV uplink with altostratus clouds present in the atmosphere.

Uplink transmittance as a function of UAV altitude in the presence of altostratus clouds
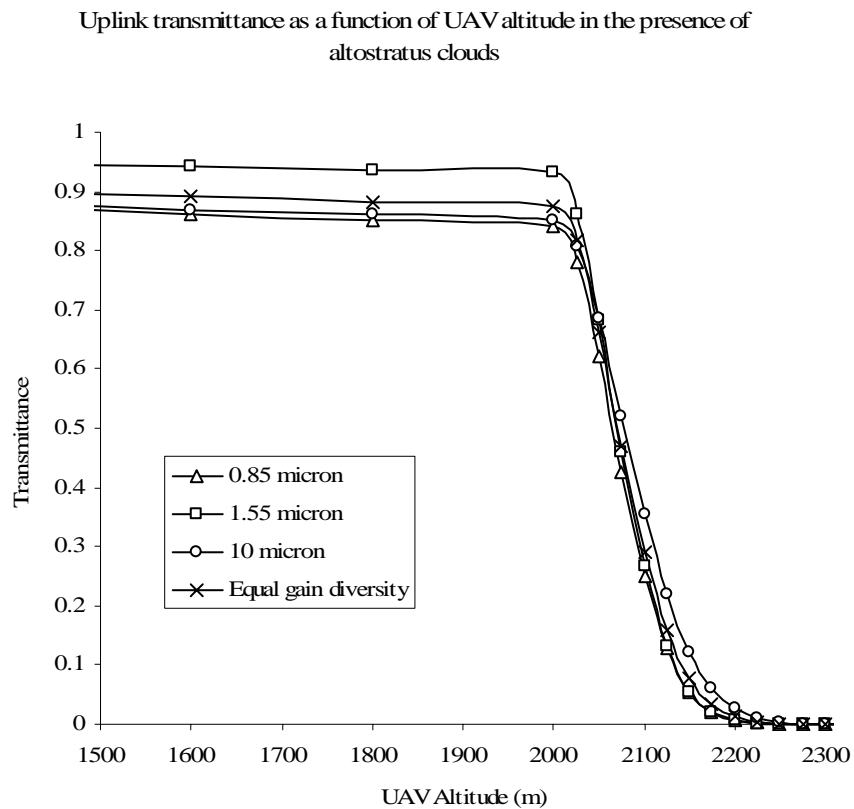
Figure 6.11 Uplink transmittance as a function of UAV altitude in the presence of altostratus clouds.

As was the case for the cumulus clouds, the FSO transmission in the presence of altostratus clouds shows a large decrease in transmittance. For the altostratus clouds, this large decrease in transmittance begins at an altitude of approximately 2000 *m*, which is approximately 400 *m* below the base of the altostratus clouds. By an altitude of 2350 *m,* no detectable light from any of the wavelengths is observed.

Figure 6.12 shows the corresponding plot of the received power expected for the ground-to-UAV uplink in the presence of altostratus clouds. From the plot it can be seen that the 1.55 *μm* wavelength has the worst performance with the altostratus clouds, with the power falling below the receiver threshold at an altitude of approximately 2212 *m*. The 10 *μm* wavelength shows the best performance, but the receiver threshold is exceeded at an altitude slightly above 2250 *m*.

Received power as a function of UAV altitude for FSO uplink in the presence of altostratus clouds
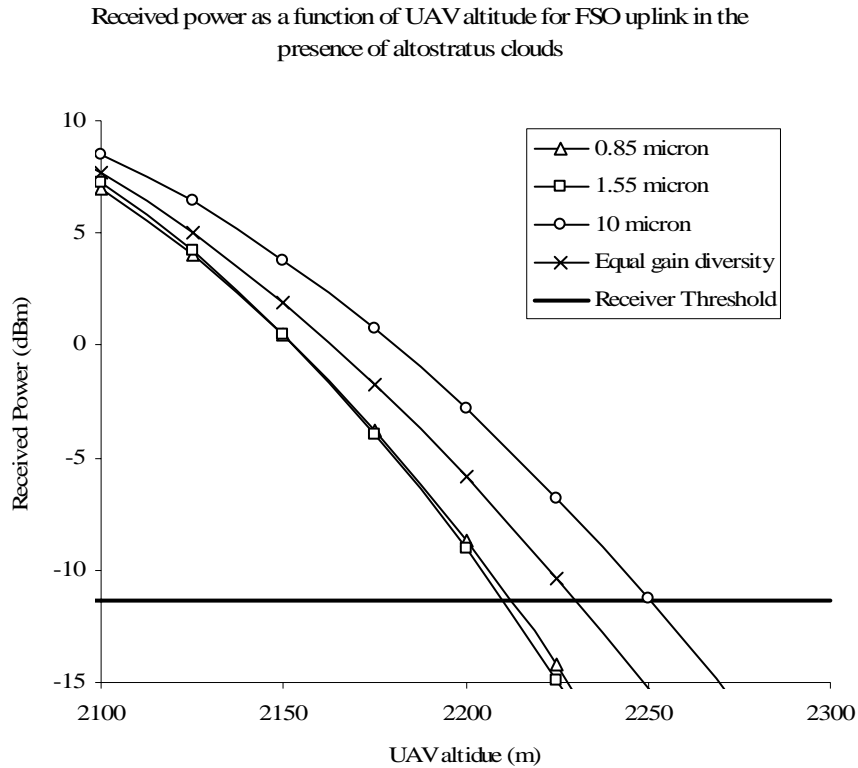
Figure 6.12 Received power as a function of UAV altitude for the FSO uplink in the presence of altostratus clouds.

The analysis performed on FSO transmission in the presence of clouds for a ground-to-UAV link has shown that for a three wavelength diversity scheme, transmission through clouds in not possible. This result implies that if clouds are present in the atmosphere, the UAV will have to maintain a flight altitude that is lower than the cloud level. While this is possible for mid-level or higher cloud formations, the reduction of UAV flight altitude would increase the chances of an actual physical attack on the UAV.

6.4.3 FSO Links in the Presence of Fog

In this section, the performance of the wavelength diversity scheme will be analyzed with the presence of both advection and radiation fog in the atmosphere. For terrestrial FSO deployment in the infrared spectral range, transmission through fog is virtually impossible. Figure 6.13 shows the transmittance as a function of UAV altitude for a ground-to-UAV FSO uplink in the presence of advection fog, with a visibility of 0.2 *km*.

In the presence of advection fog, the 0.85 *µm* and 1.55 *µm* wavelengths demonstrated the best performance of the diversity scheme, but were only able to show transmittance up to an altitude of 320 *m* in the fog. Based on this data, a further analysis of the performance of a wavelength diversified FSO link in advection fog is not necessary, because the UAV altitude to achieve transmission would be lower than 300 *m*.

Uplink transmittance as a function of UAV altitude in the presence of advection fog
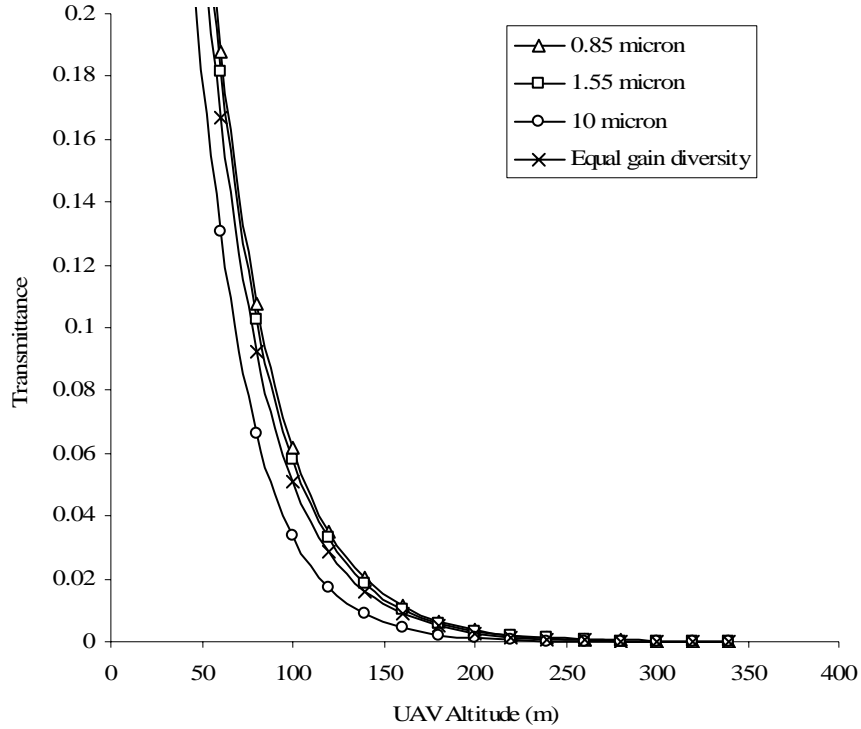
Figure 6.13 Uplink transmittance as a function of UAV altitude in the presence of advection fog.

Figure 6.14 shows the transmittance profile for a ground-to-UAV uplink with a UAV altitude of 4 *km* in the presence of radiation fog, with a visibility level of 0.5 *km*.
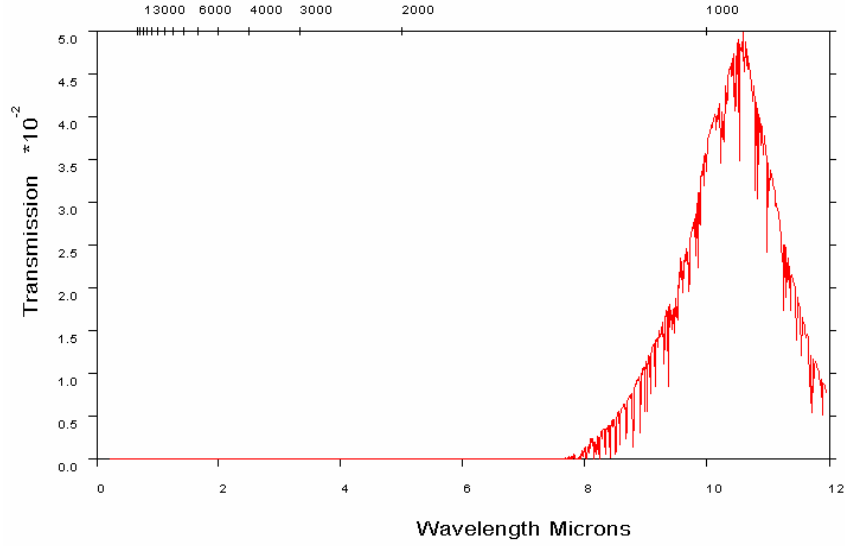
Figure 6.14 Transmittance as a function of wavelength for a 4 *km* UAV altitude with

radiation fog.

The corresponding plot for an 8 *km* UAV altitude is shown in Figure 6.15.
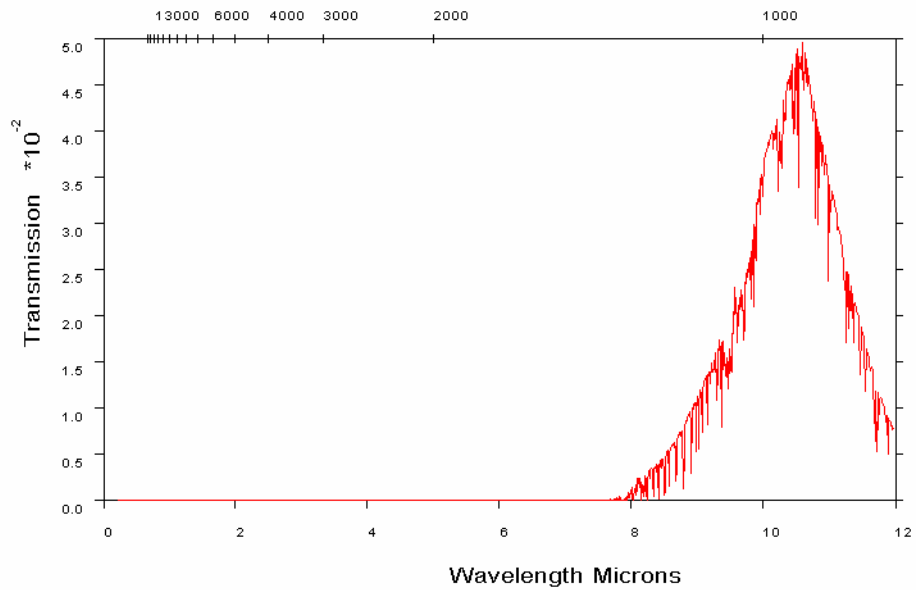
Figure 6.15 Transmittance as a function of wavelength for an 8 *km* UAV altitude with

radiation fog.

From Figures 6.14 and 6.15, it can be seen that while wavelengths shorter than 8 μm show no transmittance at the altitudes of interest, a window surrounding the 10 μm wavelength is still showing signal transmission. This window shows that the use of the proposed wavelength diversity scheme may in fact allow for the use of FSO technology in the presence of radiation fog.

Figure 6.16 shows a plot of the uplink transmittance as a function of UAV altitude in the presence of radiation fog. From the plot it is observed that by an altitude of only 800 m, both the 0.85 μm and 1.55 μm wavelengths are showing zero transmission. The 10 μm wavelength has a transmission of 3.37% at a 4 km altitude and 3.30% at an 8 km altitude.

It is also observed that the equal gain diversity scheme does show transmission at both altitudes of interest. The equal gain diversity transmission at 4 km is 1.12% and at 8 km it is 1.10%.
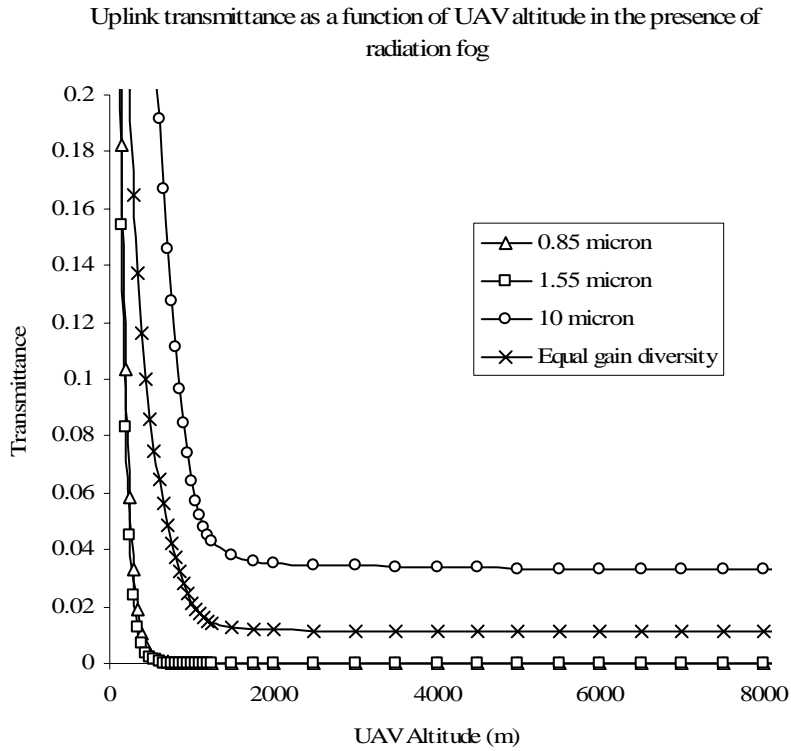
Figure 6.16 Uplink transmittance as a function of UAV altitude in the presence of

radiation fog.

A plot showing the performance of each of the wavelengths' received power as a
function of UAV altitude is shown in Figure 6.17. From the plot it can be seen that
both the 0.85 μm and 1.55 μm wavelengths drop below the receiver threshold at a
UAV altitude of between 500 and 550 m, while both the equal gain diversity scheme
and the 10 μm wavelength show the ability to maintain an FSO connection beyond an
altitude of 8 km.

Received power as a function of UAV altitude in the presence of
radiation fog
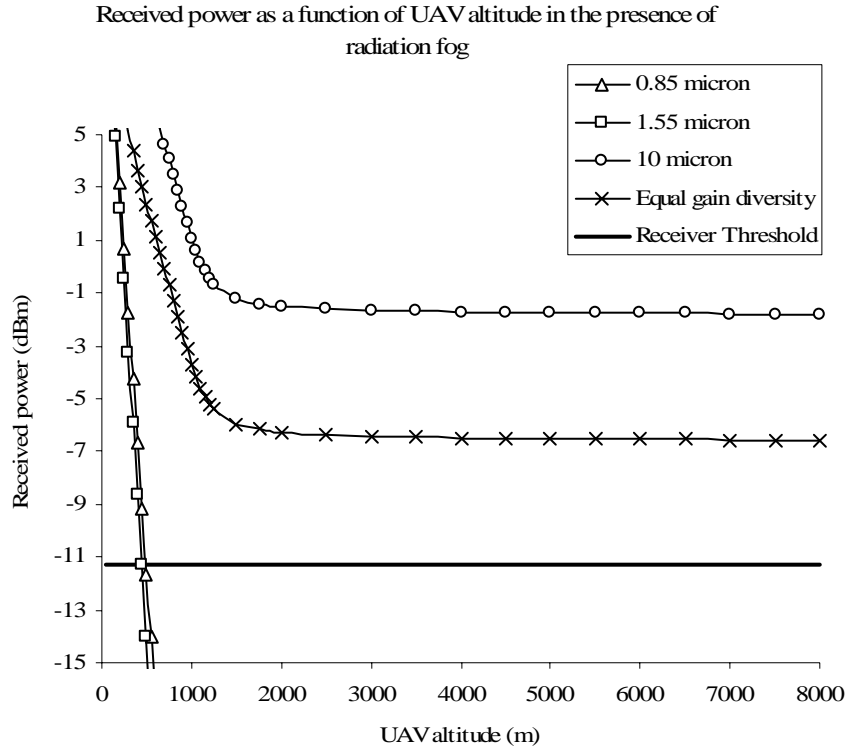
Figure 6.17 Received power as a function of UAV altitude for an FSO uplink in the

presence of radiation fog.

Even though the equal gain diversity scheme is able to maintain a connection through

radiation fog, the implementation of a selective diversity scheme which would select

the 10 μm wavelength shows a received power level that is 379% higher than the

equal gain diversity scheme for a 4 km UAV altitude and 366% higher for the 8 km

UAV altitude. This data has shown that the use of a wavelength diversity scheme

will allow uplink transmission from a ground station to a UAV, but to implement an

actual link, downlink transmission must also be possible.

Figure 6.18 shows a plot of the downlink transmittance as a function of altitude above the ground station for a UAV altitude of 4 *km*. From the figure, it is evident that for the 0.85 *μm* and 1.55 *μm* wavelengths, zero transmittance occurs between 200 *m* and 400 *m* above the ground station. For the equal gain diversity scheme, 1.12% transmittance is viewed at the ground station and for the 10 *μm* wavelength 3.37% transmittance is observed at the ground station.
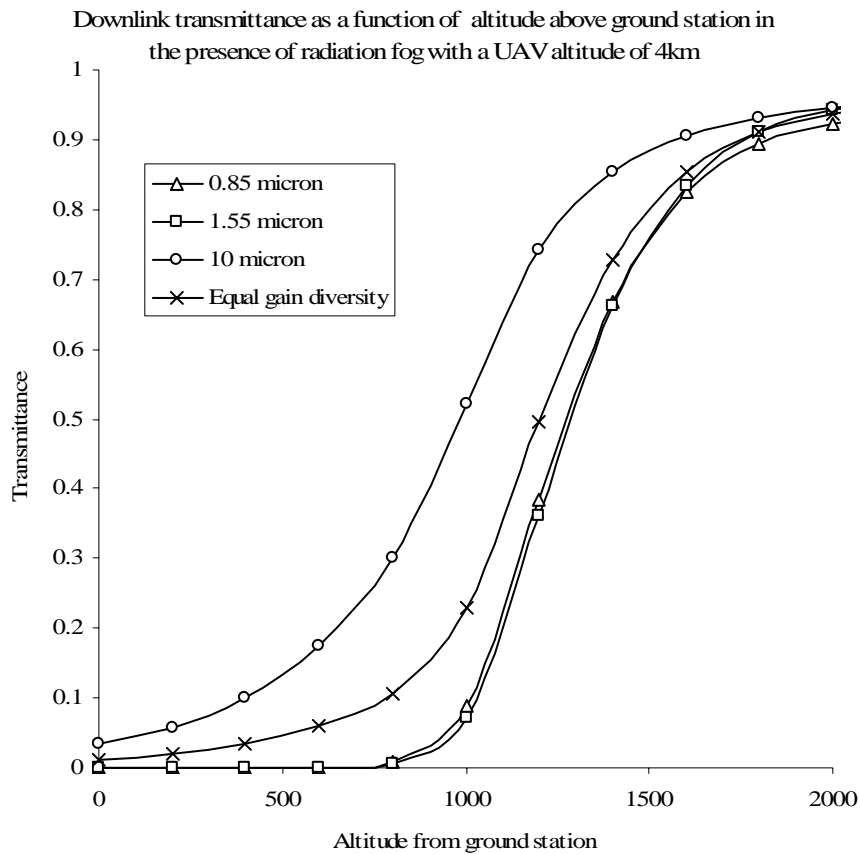
Figure 6.18 Downlink transmittance as a function of altitude above the ground station in the presence of radiation fog with a UAV altitude of 4 *km*.

Figure 6.19 shows the corresponding downlink plot for an 8 *km* UAV altitude. From the higher altitude, zero transmittance is observed for the 0.85 *μm* and 1.55 *μm* wavelengths at an altitude of between 400 *m* and 500 *m*. At the ground station, the equal gain diversity scheme shows a transmittance of 1.1% and the 10 *μm* wavelength shows a transmittance of 3.29%.

Downlink transmittance as a function of altitude above ground station in
the presence of radiation fog with a UAV altitude of 8km
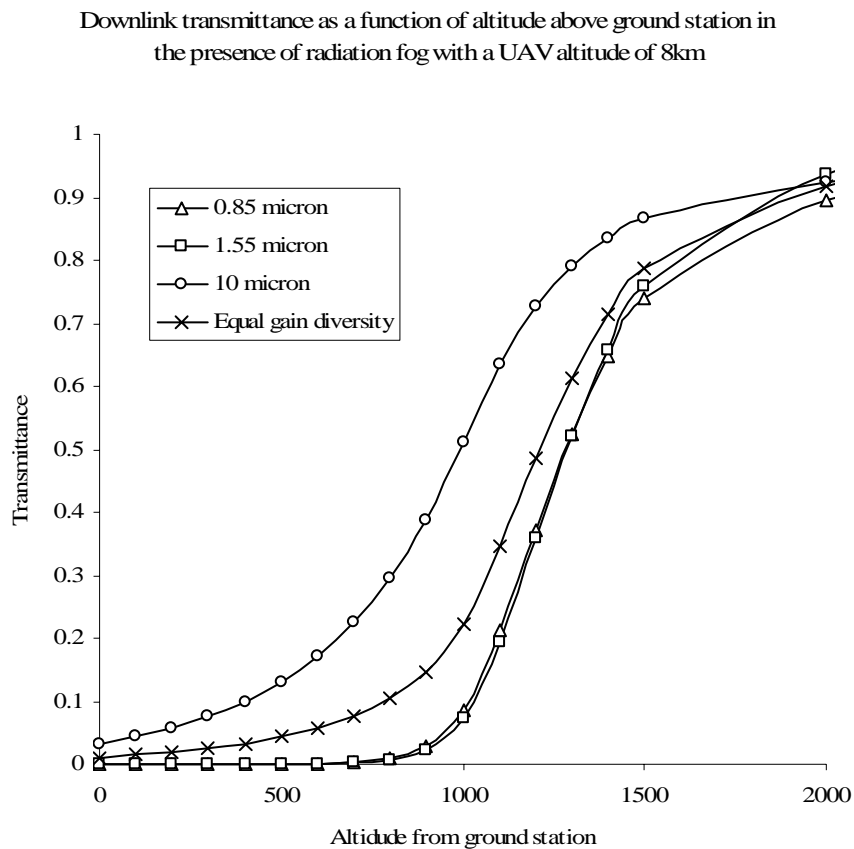
Figure 6.19 Downlink transmittance as a function of altitude above the ground station

in the presence of radiation fog with a UAV altitude of 8 *km*.

The final step is to verify that the transmittance achievable using the diversity scheme on the downlink results in a received power that is greater than the receiver threshold. Figure 6.20 shows a plot of the received power as a function of altitude above the ground station for a 4 *km* UAV altitude.

Received power as a function of altitude above ground station in the presence of radiation fog with a 4 km UAV altitude (downlink)
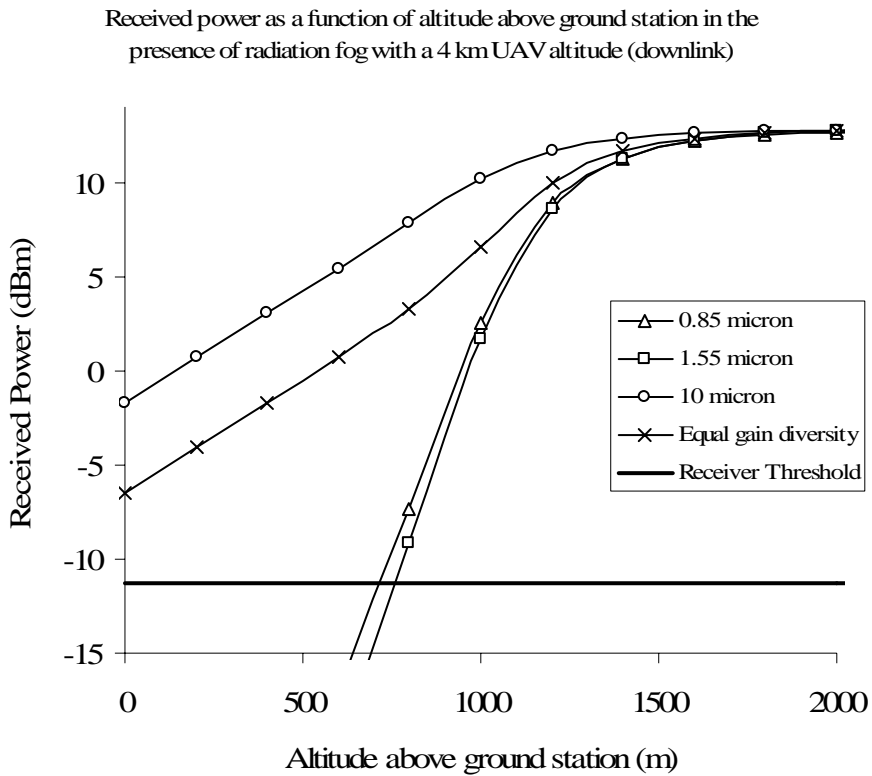
Figure 6.20 Downlink received power as a function of altitude above the ground station in the presence of radiation fog with a 4 *km* UAV altitude.

From this received power plot, it is verified that the 0.85 *μm* and the 1.55 *μm* wavelengths drop below the receiver threshold at an altitude of between 600 *m* and 800 *m* above the ground station. Both the equal gain diversity scheme and the 10 *μm*

173

wavelength are suitable for downlink transmission in the presence of radiation fog. Again, however, because of the complete absence of a signal from either the 0.85 *μm* or the 1.55 *μm* wavelengths, a selective diversity scheme would show a 305% performance improvement over the equal gain diversity scheme. Figure 6.21 shows the corresponding plot for an 8 *km* UAV altitude downlink in the presence of radiation fog. For the 8 *km* UAV altitude, the 0.85 *μm* and the 1.55 *μm* wavelengths drop below the receiver sensitivity threshold at an altitude between 700 *m* and 800 *m*. The wavelength diversity scheme results in a received signal strength of -6.59 *dBm* and the 10 *μm* wavelength has a received signal strength of -1.82 *dBm*.

Received power as a function of altitude above ground station in the presence fo radiation fog with an 8 km UAV altitude (downlink)
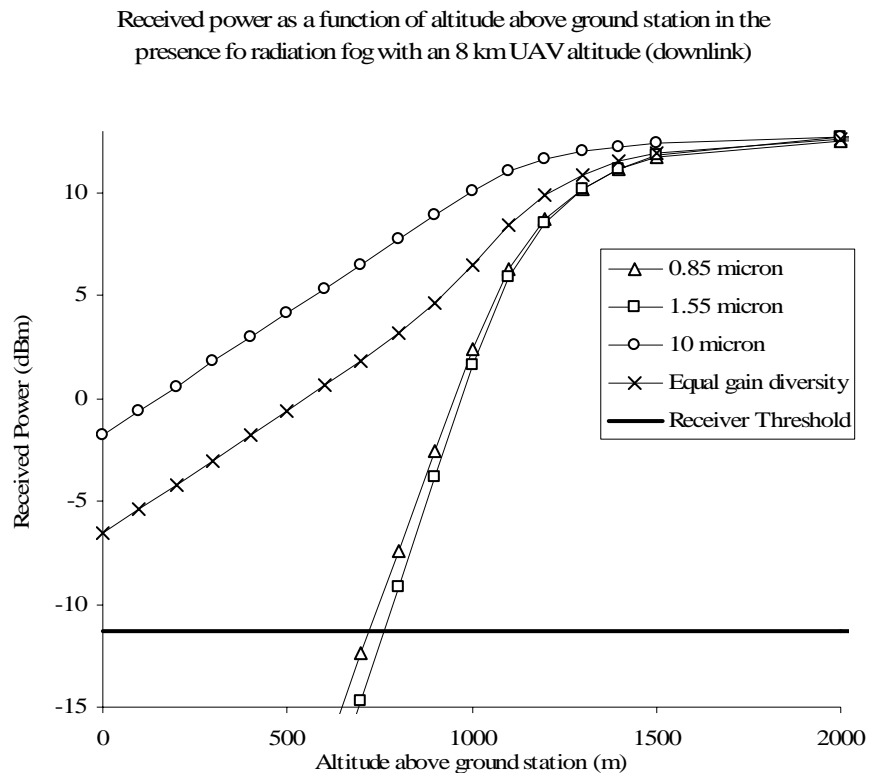
Figure 6.21 Downlink received power as a function of altitude above the ground station in the presence of radiation fog with an 8 *km* UAV altitude.

6.5 Summary

In this chapter, a detailed analysis of the effects of different atmospheric weather conditions on three different wavelengths of a wavelength diversity scheme has been discussed. Under clear weather conditions, no advantage was found in the implementation of either an equal gain or selective wavelength diversity scheme since all three wavelengths are easily transmitted. In the presence of either low-level cumulus clouds or mid-level altostratus clouds, none of the three wavelengths were able to achieve transmission through the cloud barrier. It was further shown that for an FSO link operating in advection fog, transmission beyond and altitude of 300 m was not possible. The wavelength diversity scheme did, however, enable the transmission of FSO signals through radiation fog. While an equal gain diversity scheme was shown to perform successfully in the presence of radiation fog, a selective diversity scheme provides the best performance. It should also be noted that due to the loss associated with the transmission of a 10 μm wavelength through glass, an alternate lens material such as ZnSe would need to be used.

Chapter 7

Conclusions and Future Work

7.1 Conclusions

The research presented in this dissertation has focused on the use of FSO technology to establish and maintain a communications link between a ground station and a UAV. The results obtained through a theoretical analysis, experimentation and simulation techniques have shown that FSO is a viable technology for deployment in high bandwidth ground-to-UAV communications links.

FSO technology is advantageous for the provision of a high bandwidth communications link between a ground station and a UAV for the following reasons:

- FSO technology does not require Federal Communications Commission (FCC) licensing.

- FSO equipment has been demonstrated to be a viable transport medium for transmitting existing RF signals in analog format.

- Communications links employing FSO technology are highly immune to electromagnetic interference.

- FSO transmitters and receivers are highly invulnerable to interference from other optical radiation sources.

- Once established, FSO links are extremely immune to interference and interception.

- Optical transmission of data requires far smaller transmitter and receiver aperture sizes than corresponding millimeter wave technology.

- FSO equipment is highly portable – for a ground-to-UAV application, FSO ground units can easily be mobilized to setup the required ground station.

- Gimbal equipment is currently available with the accuracy to align and track ground-to-UAV FSO links.

- Wavelength diversity schemes can be incorporated into FSO communications in order to improve link acquisition and performance in the presence of atmospheric turbulence.

- Wavelength diversity schemes can reduce the impact of atmospheric weather conditions, particularly radiation fog, on FSO communications links.

The contributions of this dissertation work and conclusions that follow indicate that FSO technology could be used to communicate between a ground station and a UAV.

First, a study on analytical calculations of a gimbal's beam steering tolerances and an FSO communications link's beam divergence was performed. This initial study was motivated by the desire to verify the effectiveness of FSO technology as a communications method for several different length communications lengths. This first part of the study resulted in the following observations:

177

- For FSO communications links longer than and Earth-to-Satellite range, standard FSO equipment will be unable to overcome geometric losses present in the link.

- Divergence limited FSO links become limited by geometric losses at distances exceeding Earth-to-Mars links.

- By limiting divergence and employing large scale (i.e., telescopic or array-based receivers) FSO is a suitable communications method for deep-space communications systems.

- For FSO links in which a divergence limited system is required (i.e., links exceeding Earth-to-Satellite distances) beam steering tolerances are a limiting factor. For these links, an active optical beam steering system would be required to augment a mechanical gimbal-based alignment system, as well as a method to offset platform vibrations present in the communications system.

The second part of the first study was a comparison of active beam steering elements for FSO links between moving platforms along with a simulation of the effects of platform vibrations on beam steering tolerances. This portion was performed in order to verify that technology is available to offset platform vibrations in these types of FSO communications links. This study found that both FSMs and Bragg cell deflectors could be used to effectively offset platform vibrations present in FSO links. The final part of the first study used analytical techniques to model a ground-to-UAV FSO communications link. This study resulted in a series of equations relating the

relative positions of the ground station and the UAV as well as a mathematical description of the expected Gaussian laser beam profile at the UAV receiver of the FSO communications link. The results from the first contribution of this dissertation verify that FSO technology is a viable communications method for ground-to-air communications.

Second, through experimental methods, a mechanical gimbal was analyzed in order to determine the gimbal's repeatability and error. Along with the experimental analysis, a simulation was run in order to calculate the FSO beam profile at the UAV end of the FSO link. This study showed that the gimbal repeatability and error are of a small enough magnitude that beam divergence in the presence of atmospheric turbulence can be successfully used as a method to assist with the alignment and tracking of FSO communications links.

Third, the use of a wavelength diversity scheme to improve alignment and tracking of a ground-to-UAV FSO communications link was proposed. This proposal included a detailed analysis of the effects of atmospheric turbulence on each of the three wavelengths of the wavelength diversity scheme. The results of this study showed that the use of a wavelength diversity scheme will increase the coverage area of an alignment protocol as well as help to mitigate the effects of atmospheric turbulence on a ground-to-UAV FSO communications link.

Fourth, the use of the proposed wavelength diversity scheme as a method to improve FSO performance under different weather conditions was introduced. The use of the proposed wavelength diversity scheme showed that FSO transmission through cloud formations, as well as advection fog, is not possible using the three wavelengths of the scheme. The wavelength diversity scheme did, however, prove that transmission on a slant path is possible through radiation fog. The use of a selective diversity scheme provides improved performance over an equal gain diversity scheme.

7.2 Future Work

This investigation has led to several ideas for future research. First, an experimental analysis needs to be performed on an active optical component, such as a fast steering mirror, in order to effectively analyze the components suitability for vibration offset and beam steering in a ground-to-UAV FSO communications link. This investigation would also require the study of vibration dampening devices.

Furthermore, this investigation showed that the use of a wavelength diversity scheme is advantageous for both alignment purposes and the transmission of FSO signals through radiation fog. It was, however, discovered that transmission through clouds and advection fog using this scheme is not possible. The investigation of a technique for transmission through cloud formations and advection fog was left as a topic for future investigation.

References

[1] Heinz Willebrand, Ghuman Baksheesh, *Free-Space Optics: Enabling Optical Connectivity in Today's Networks*, Sams Publishing Indianapolis, Indiana, 2002.

[2] E. Gubbins, "News – Air Fiber CEO loses faith in FSO – After demise of free-space optics vendor, Air Fiber, former CEO Brett Helm says the technology won't support a stand-alone business plan", *Telephony*, Vol. 244, no. 5, 2003, pp. 14-15.

[3] Predator unmanned aerial vehicle (UAV), USA, Air Force Technology, http://www.airforce-technology.com/project_printable.asp?ProjectID=1137, 2004.

[4] H. H. Refai, J. J. Sluss, Jr., and H. H. Refai, "The transmission of multiple RF signals in free-space optics using wavelength division multiplexing", *Proceedings of the SPIE*, Vol. 5793, 2005, pp. 136-143.

[5] H. H. Refai, J. J. Sluss, Jr., and H. H. Refai, "Optical interference on free-space optical transceivers", *Frontiers in Optics – 87th Optical Society of America Annual Meeting*, Tuscon, AZ, October, 2003, WJJ6.

[6] H. H. Refai, J. J. Sluss, Jr., and H. H. Refai, "Free-space optical communication performance in the presence of interfering laser signals", *Proceedings of the SPIE Defense and Security Symposium*, Vol 5793, 2005, pp.

[7]   J. Wang, and J. M. Kahn, "Acquisition in short-range free-space optical communication", *Proceedings of the SPIE Optical Wireless Communications*, Vol. 4873, pp. 121-132.

[8]   D. Begley, "Laser Cross-Link Systems and Tecnology", *IEEE Communicaitons Magazine*, August 2000, pp. 126-132

[9]   A. Harris, J. J. Sluss, Jr., H. H. Refai, and P. G. LoPresti, "Alignment and tracking of a free-space optical communications link to a UAV", *24th Annual IEEE Digital Avionics Conference*, Washington, DC, October-November, 2005.

[10] A. Harris, J. J. Sluss, Jr., H. H. Refai, and P. G. LoPresti, "Atmospheric turbulence effects on a wavelength diversified ground-to-UAV FSO link", *Proceedings of SPIE Photonics West*, San Jose, January 2006.

[11] E. Wainright, H. H. Refai, J. J. Sluss, Jr., "Wavelength diversity in free-space optics to alleviate fog effects", Proceedings of the SPIE, Vol. 5712, 2005, pp. 110-118.

[12] Alan Harris, James J. Sluss, Jr. and Hazem H. Refai, "Wavelength diversity scheme for a ground-to-UAV free-space optical communication link," To be submitted to SPIE Optical Engineering.

[13] A. Harris, J. J. Sluss, Jr., H. H. Refai, and P. G. LoPresti, "Analysis of beam steering tolerances and divergence for various long range FSO communication links", *Proceedings of the SPIE Defense and Security Symposium*, Vol. 5189, pp. 455-463.

[14] A. Harris, J. J. Sluss, Jr., H. H. Refai, and P. G. LoPresti, "Comparison of active beam steering elements and analysis of platform vibrations for various long-range FSO links", *Proceedings of the SPIE Defense and Security Symposium*, Vol. 5819, pp. 474-485.

[15] H. A. Willebrand and B. Ghuman, "Fiber optics without fiber", *IEEE Commuications Magazine*, August 2000, pp. 126-132.

[16] G. S. Mercherle, and K. L. Marrs, "Description and Results of a Satellite Laser Communication / Tracking Simulation", *IEEE Aerospace Applications Conference*, 1994, pp. 87-101.

[17] M. Scheinfeild, and N. S. Kopeika, "Acquisition System for Microsatellites Laser Communication in Space", *Proceedings of the SPIE Free-Space Laser Communication Technologies XII*, Vol. 3922, pp. 166-175.

[18] S. Arnon, "Use of satellite natural vibrations to improve performance of free-space satellite laser communication", *Applied Optics*, Vol. 37, No. 21, 1998, pp. 5031-5036.

[19] S. Arnon, N. S. Kopeika, "The Performance Limitations of Free Space Optical Communication Satellite Networks Due to Vibrations – Analog Case", *IEEE Nineteenth Convention of Electrical and Electronic Engineers in Israel*, 1996, pp. 287-290.

[20] M. Gebhart, P. Schrotter, U. Birnbacher and E. Leitgeb, "Satellite Communications, Free Space Optics and Wireless LAN combined: Worldwide

broadband wireless access independent of terrestrial infrastructure", *IEEE MELECON*, 2004, pp. 449-452.

[21] I. M. Teplyakov, "Acquisition and tracking of laser beams in space communications", *Acto Astronautics*, Vol. 7, 1980, pp. 341-355.

[22] J. M. Lapez, K. Yong, "Acquisition, tracking, and fine pointing control of space-based laser communication system", *Control and Communication Technology in Laser Systems, Proceedings of the SPIE*, Vol. 295, 1981, pp. 100-114.

[23] S. Lambert, and W. Casey, *Laser Communications in Space*, Artech House, Boston, MA, 1995.

[24] R. B. Deadrick, "Design and performance of a satellite laser communications pointing system", *Advances in Astronautical Sciences*, Vol. 57, 1985, pp. 155-166.

[25] K. Wilson, and M. Enoch, "Optical Communications for Deep Space Missions", *IEEE Communications Magazine*, August 2000, pp. 134-139.

[26] H. Hemmati, "Status of Free-Space Optical Communication Program at JPL", *IEEE Aerospace Conference Proceedings*, Vol 3, 2000, pp. 101-105.

[27] H. Hemmati, "Free-Space Optical Communications Program at JPL", *IEEE Lasers and Electro-Optics Society 12th Annual Meeting*, Vol. 1, 1999, pp. 106-107.

[28] S. S. Badesha, "SPARCL: a high-altitude tethered balloon-based optical space-to-ground communication system", *Proceedings of the SPIE Free-space Laser Communication and Laser Imaging II*, Vol. 4821, 2002, pp. 181-193.

[29] D. M. Boroson, A. Biswas, and B. L. Edwards, "MLCD: overview of NASA's Mars laser communications demonstration system", *Proceedings of the SPIE Free-Space Laser Communication Technologies XVI*, Vol. 5338, 2004, pp. 16-28.

[30] L. C. Andrews, R. L. Phillips, and C. Y. Hopen, *Laser Beam Scintillation with Applications*, SPIE Press, Bellingham, WA, 2001.

[31] R. D. Hudson, Jr., *Infrared System Engineering*, Wiley & Sons, 1969.

[32] H. Weichel, *Laser Beam Propagation in the Atmosphere*, SPIE Optical Engineering Press, Bellingham, WA, 1990.

[33] N. S. Kopeika, *A System Engineering Approach to Imaging*, SPIE Optical Engineering Press, Bellingham, WA, 1998.

[34] V. E. Zuev, *Laser Beams in the Atmosphere*, Consultants Bureau, New York, 1998.

[35] G. Keiser, *Optical Fiber Communications*, McGraw-Hill, 2000.

[36] J. Sofka, V. V. Nikulin, V. A. Skormin, D. J. Nicholson, M. Rosheim, "New generation of gimbal systems for laser pointing applications", *Proceedings of the SPIE Free-Space Laser Communication and Active Laser Illumination III*, Vol. 5160, 2003, pp. 182-191.

[37] V. V. Nikulin, J. Sofka, V. A. Skormin, "Decentralized control of an Omni Wrist laser beam tracking system", *Proceedings of the SPIE Free-Space Laser Communication Technologies XVI*, Vol. 5338, 2004, pp. 194-203.

[38] M. E. Rosheim and G. F. Sauter, "New High-Angulation Omni-Directional Sensor Mount", *Ross-Hime Desings Inc,* http://www.anthrobot.com/

[39] J. Sofka, V. V. Nikulin, V. A. Skormin, and D. J. Nicholson, "Hybrid laser beam steerer for laser communications applications", *Proceedings of the SPIE Free-Space Laser Communication and Active Laser Illumination III*, Vol. 5160, 2003, pp. 161-169.

[40] S. C. Wilks, J. R. Morris, J. M. Brase, S. S. Oliveier, J. R. Henderson, C. A. Thompson, M. W. Kartz, and A. J. Ruggerio, "Modeling of adaptive-optics-based free-space communications system", *Proceedings of the SPIE Free-space Laser Communication and Laser Imaging II*, Vol. 4821, 2002, pp. 121-128.

[41] C. A. Thompson, M. W. Kartz, L. M. Flath, S. C. Wilks, R. A. Young, G. W. Johnson, and A. J. Ruggiero, "Free-space optical communications utilizing MEMS adaptive optics correction", *Proceedings of the SPIE Free-space Laser Communication and Laser Imagin II,* Vol. 4821, 2002, pp. 129-138.

[42] C. H. Chalfant, F. J. Orlando, J. T. Gregory, C. Sulham, C. B. O'Neal, G. W. Taylor, D. M. Craig, J. J. Foshee, J. T. Lovett, "Novel laser communications transceiver with internal gimbal-less pointing and tracking", *Proceedings of the SPIE Free-space Laser Communication and Laser Imaging II*, Vol. 4821, 2002, pp. 194-201.

[43] J. E. Stockley, S. Serati, X. Xun, R. W. Cohn, "Liquid crystal spatial light modulator for multispot beam steering", *Proceedings of the SPIE Free-Space*

Laser Communication and Active Laser Illumination III, Vol. 5160, 2003, pp. 208-215.

[44] P. W. Fairchild, D. Lilly, W. B. Matkin, "Field test results of the three-dimensional acquisition and tracking (3DATA) sensor system", *Proceedings of the SPIE Free-Space Laser Communication and Active Laser Illumination III*, Vol. 5160, 2003, pp. 216-224.

[45] M. R. Suite, H. R. Burris, C. I. Moore, M. J. Vilcheck, R. Mahon, C. Jackson, M.F. Stell, M. A. Davis, W. S. Ravinovich, W. J Scharpf, A. E. Reed, G. C. Gilbreath, "Fast steering mirror implementation for recuction of focal-spot wander in a long-distance free-space communication link", *Proceedings of the SPIE Free-Space Laser Communication and Active Laser Illumination III*, Vol. 5160, 2003, pp. 439-446.

[46] K. Aoki, Y. Yanagita, H. Kuroda, K. Shiratama, "Wide-range fine pointing mechanism for free-space laser communications", *Proceedings of the SPIE Free-Space Laser Communication and Active Laser Illumination III*, Vol. 5160, 2003, pp. 495-506.

[47] Ball Aerospace and Technologies Incorporated, http://www.ballaerospace.com/

[48] G. Lu, Y. Lu, T. Deng and H. Liu, "Automatic alignment of optical-beam-based GPS for a free-space laser communication system", *Proceedings of the SPIE Free-Space Laser Communication and Active Laser Illumination III*, Vol. 5160, 2003, pp. 432-438.

[49] W. L. Saw, H. H. Refai and J. J. Sluss, Jr., "Free space optical alignment system using GPS", *Proceedings of the SPIE Free-Space Laser Communication Technologies XVII*, Vol. 5712, 2005, pp. 101-109.

[50] J. Wang, J. M. Kahn, "Acquisition in short-range free-space optical communication", *Proceedings of the SPIE Optical Wireless Communications V*, Vol. 4783, 2002, pp. 121-132.

[51] J. Burks, "Controller Pilot Data Link Communications over VHF Digital Link Mode 2", *ICNS Conference*, 2003.

[52] Sagebrush Technology, Inc., http://www.sagebrushtech.com

[53] Texas Instruments, "Discovery 1100 Controller Board & Starter Kit", http://www.ti.com

[54] Quanta-Tech, http://www.quanta-tech.com/Acousto_optic_products/

[55] A. Ishimaru, *Wave Propagation and Scattering in Random Media*, IEEE Press, New Jersey, 1997.

[56] L. C. Andrews and R. L. Phillips, *Laser Beam Propagation through Random Media*, SPIE Optical Engineering Press, Belingham, WA, 1998.

[57] L. C. Andrews and R. L. Phillips, Laser Beam Propagation through Atmospheric Turbulence User Manual.

[58] Properties Of the U.S. Standard Atmosphere 1976, 2005, http://www.pdas.com/atmos.htm

[59] Plymouth State University Meteorology Program Cloud Boutique, 2005, http://vortex.plymouth.edu/clouds.html

[60] PcModWin 4.0 User Manual, V1R1.V1.1, July 2002.

Appendix A

Gimbal Experimental Data

This appendix contains the experimental data for the gimbal repeatability and accuracy measurements. A sample set of 20 data points for each trial along with an explanation is provided. For a complete listing of all 14,000 data points, see that attached CD-ROM.

The gimbal repeatability data is shown in Table A.1. The data contains the four outputs from the DL-100-7PCBA X,Y duo-lateral position sensing photodiode (PSD). The outputs are the X-Voltage, the Y-Voltage, the X-Sum Voltage and the Y-Sum Voltage. These output voltages are used to calculate the position of the centroid of the laser beam on the PSD. The position is then shifted in order to normalize the data.

Vy(out)	Vx(out)	Y Sum	X Sum	X Position	Y Position	Shifted X	Shifted Y
-0.3038	-0.18204	1.728363	-1.70395	0.106833	-0.17577	0.773333	0.204225
-0.61005	0.301208	1.950989	-1.9281	-0.15622	-0.31269	0.51028	0.067314
-0.14084	-0.25879	1.704407	-1.68808	0.153304	-0.08263	0.819804	0.297368
-0.57205	0.313263	2.045288	-2.02301	-0.15485	-0.27969	0.51165	0.100307
-0.29617	0.181427	1.97937	-1.95496	-0.0928	-0.14963	0.573696	0.23037
-0.25528	-0.39703	1.654663	-1.61713	0.245518	-0.15428	0.912018	0.225721
-0.56854	0.452728	2.02652	-1.98914	-0.2276	-0.28055	0.4389	0.099449
-0.15579	0.090179	1.938629	-1.90109	-0.04744	-0.08036	0.619064	0.299638
-0.54764	0.125427	1.995087	-1.96106	-0.06396	-0.27449	0.602541	0.105507
-0.31021	0.137482	1.99295	-1.95267	-0.07041	-0.15565	0.596093	0.224346
-0.26154	-0.4776	1.665344	-1.64261	0.290757	-0.15705	0.957257	0.222954
-0.55908	0.499878	2.073364	-2.03735	-0.24536	-0.26965	0.421143	0.11035
-0.1796	0.551453	2.122345	-2.07855	-0.26531	-0.08462	0.401194	0.295379
-0.5014	0.075836	1.885834	-1.86264	-0.04071	-0.26588	0.625786	0.114121

-0.31342	0.127563	1.980743	-1.9487	-0.06546	-0.15823	0.601039	0.221769
-0.28229	-0.01328	1.864929	-1.84219	0.007206	-0.15137	0.673706	0.228634
-0.49438	0.097504	1.985168	-1.94168	-0.05022	-0.24904	0.616284	0.130961
-0.14252	0.224609	1.97403	-1.94977	-0.1152	-0.0722	0.551302	0.307804
-0.52307	0.260162	1.991272	-1.97281	-0.13187	-0.26268	0.534626	0.117318

Table A.1 Gimbal repeatability sample data.

The gimbal accuracy data is shown in Table A.2.

Vy(out)	Vx(out)	Accuracy
-0.29724	0.112152	0.012472
-0.25467	-0.32837	0.236035
-0.5011	0.29953	0.154102
-0.1738	0.663605	0.277252
-0.48325	-0.05676	0.131782
-0.28641	0.107117	0.010846
-0.2565	-0.14008	0.126018
-0.52292	0.230408	0.130283
-0.13229	0.272675	0.126409
-0.48859	-0.03403	0.125546
-0.26871	0.102539	0.016722
-0.22858	-0.29541	0.220563
-0.50751	0.431519	0.194464
-0.17197	0.731201	0.314569
-0.49301	0.126495	0.107037
-0.30014	0.122375	0.01713
-0.21011	-0.39871	0.297299
-0.54626	0.395508	0.191518
-0.10971	-0.25864	0.213796
-0.49866	0.256348	0.136822

Table A.2 Gimbal accuracy sample data.

Appendix B

Wavelength Diversity in the Presence of Weather Data

The tables in this appendix contain the data obtained from multitudes of PcModWin simulations. Table B.1 contains the data for the clear weather uplink.

Altitude	0.85 micron	1.55 micron	10 micron	Equal gain diversity
500	0.9434	0.9763	0.9443	0.9546
1000	0.9007	0.9579	0.904	0.9208
1500	0.868	0.9435	0.8747	0.8954
2000	0.8429	0.9323	0.8529	0.8760
2500	0.8242	0.9243	0.8373	0.8619
3000	0.8099	0.919	0.8269	0.8519
3500	0.8004	0.916	0.82	0.8454
4000	0.7933	0.9138	0.815	0.8407
4500	0.7905	0.9122	0.8112	0.8379
5000	0.7842	0.9111	0.8084	0.8345
5500	0.781	0.9102	0.8061	0.8324
6000	0.7781	0.9093	0.8043	0.8305
6500	0.7755	0.9086	0.8026	0.8289
7000	0.7731	0.9079	0.8012	0.8274
7500	0.771	0.9073	0.7998	0.8260
8000	0.7695	0.9069	0.7986	0.825

Table B.1 Transmittance values for ground-to-air uplink in clear weather.

Table B.2 contains the data for the air-to-ground downlink in clear weather with the UAV following a flight altitude of 4 *km*.

Altitude	0.85 micron	1.55 micron	10 micron	Equal gain diversity
3500	0.9911	0.9976	0.993	0.9939
3000	0.9795	0.9944	0.9837	0.9859
2500	0.9631	0.9875	0.9705	0.9737
2000	0.9411	0.9802	0.9516	0.9576
1500	0.9138	0.9685	0.927	0.9364
1000	0.8807	0.954	0.8968	0.9105
500	0.8408	0.936	0.8596	0.8788
0	0.7932	0.9138	0.814	0.8403

Table B.2 Transmittance values for air-to-ground downlink in clear weather with a 4

***km* UAV altitude.**

Table B.3 shows the corresponding data for the air-to-ground downlink in clear weather with an 8 *km* altitude.

Altitude	0.85 micron	1.55 micron	10 micron	Equal gain diversity
7500	0.9979	0.9995	0.9984	0.9986
7000	0.9953	0.9989	0.9966	0.9969
6500	0.9923	0.9981	0.9946	0.9950
6000	0.9889	0.9973	0.9925	0.9929
5500	0.9852	0.9964	0.99	0.9905
5000	0.9812	0.9954	0.9869	0.9878
4500	0.9764	0.9941	0.9831	0.9845
4000	0.97	0.9924	0.978	0.9801
3500	0.9614	0.99	0.9713	0.9742
3000	0.95	0.9868	0.9623	0.9664
2500	0.9342	0.9814	0.9495	0.9550
2000	0.9128	0.9727	0.9312	0.9389
1500	0.8863	0.9611	0.9074	0.9183
1000	0.8542	0.9467	0.878	0.8930
500	0.8154	0.9288	0.8419	0.8620
0	0.7692	0.9068	0.7984	0.8248

Table B.3 Transmittance values for air-to-ground downlink in clear weather with an 8

***km* UAV altitude.**

Table B.4 shows the transmittance data obtained for the ground-to-air FSO uplink with cumulus clouds present in the atmosphere.

Altitude	0.85 micron	1.55 micron	10 micron	Equal gain diversity
50	0.9936	0.9973	0.9935	0.9948
100	0.9873	0.9948	0.9872	0.9898
150	0.9813	0.9922	0.9812	0.9849
200	0.9754	0.9898	0.9753	0.9802
250	0.9696	0.9874	0.9698	0.9756
300	0.964	0.985	0.9644	0.9711
350	0.9373	0.9602	0.9361	0.9445
400	0.7227	0.7378	0.7085	0.7230
425	0.5708	0.58	0.5501	0.5670
450	0.4201	0.424	0.3959	0.4133
475	0.2881	0.2883	0.2641	0.2802
500	0.1841	0.1823	0.1633	0.1766
525	0.1096	0.1072	0.0935	0.1034
550	0.0608	0.0586	0.0497	0.0564
575	0.0314	0.0298	0.0244	0.0285
600	0.0151	0.0141	0.0112	0.0135
625	0.0068	0.0062	0.0047	0.0059
650	0.0028	0.0025	0.0018	0.0024
675	0.0011	0.001	0.0007	0.0009
700	0.0004	0.0004	0.0002	0.0003
725	0.0001	0.0001	0.0001	0.0001
750	0	0	0	0.0000

Table B.4 Ground-to-air uplink data with cumulus clouds.

Table B.5 shows the transmittance data obtained for the ground-to-air FSO uplink with altostratus clouds present in the atmosphere.

Altitude	0.85 micron	1.55 micron	10 micron	Equal gain diversity
200	0.9754	0.9898	0.9753	0.98017
400	0.9535	0.9805	0.954	0.96267
600	0.9339	0.9722	0.9352	0.94710
800	0.9164	0.9647	0.9186	0.93323
1000	0.9007	0.9579	0.904	0.92087
1200	0.8912	0.9517	0.8866	0.90983
1400	0.8739	0.9461	0.8799	0.89997
1600	0.8625	0.9411	0.8698	0.89113
1800	0.8522	0.9365	0.8609	0.88320
2000	0.8429	0.9323	0.8529	0.87603
2025	0.7807	0.8617	0.8069	0.81643
2050	0.6222	0.6812	0.6849	0.66277
2075	0.4265	0.4606	0.5214	0.46950
2100	0.2516	0.2663	0.3562	0.29137
2125	0.1276	0.1317	0.2182	0.15917
2150	0.0557	0.0557	0.12	0.07713
2175	0.0209	0.0201	0.0592	0.03340
2200	0.0068	0.0062	0.0262	0.01307
2225	0.0019	0.0016	0.0104	0.00463
2250	0.0004	0.0004	0.0037	0.00150
2275	0.0001	0.0001	0.0012	0.00047
2300	0	0	0.0003	0.00010
2325	0	0	0.0001	0.00003
2350	0	0	0	0.00000

Table B.5 Ground-to-air uplink data with altostratus clouds.

Table B.6 shows the transmittance data obtained for the ground-to-air uplink in the
presence of advection fog with a visibility of 0.2 *km*.

Altitude	0.85 micron	1.55 micron	10 micron	Equal gain diversity
20	0.5726	0.5661	0.5074	0.5487
40	0.3279	0.3205	0.2574	0.3019
60	0.1877	0.1814	0.1306	0.1666
80	0.1075	0.1027	0.0663	0.0922
100	0.0616	0.0581	0.0336	0.0511
120	0.0352	0.0329	0.0171	0.0284
140	0.0202	0.0186	0.0087	0.0158
160	0.0116	0.0105	0.0044	0.0088
180	0.0066	0.006	0.0022	0.0049
200	0.0038	0.0034	0.0011	0.0028
220	0.0022	0.0019	0.0006	0.0016
240	0.0012	0.0011	0.0003	0.0009
260	0.0007	0.0006	0.0001	0.0005
280	0.0004	0.0003	0.0001	0.0003
300	0.0002	0.0002	0	0.0001
320	0.0001	0.0001	0	0.0001
340	0	0	0	0.0000

Table B.6 Advection fog uplink data.

The data obtained for the radiation fog atmospheric weather is shown in Table B.7.

Altitude	0.85 micron	1.55 micron	10 micron	Equal gain diversity
50	0.5671	0.5364	0.8707	0.658066667
100	0.3216	0.2877	0.7582	0.455833333
150	0.1824	0.1544	0.6604	0.3324
200	0.1034	0.0828	0.5753	0.253833333
250	0.0587	0.045	0.5012	0.201633333
300	0.0333	0.0238	0.4368	0.164633333
350	0.0189	0.0128	0.3806	0.137433333
400	0.0107	0.0069	0.3318	0.116466667
450	0.0061	0.0037	0.2892	0.099666667
500	0.0034	0.002	0.2521	0.085833333
550	0.002	0.0011	0.2198	0.0743
600	0.0011	0.0006	0.1917	0.064466667
650	0.0006	0.0003	0.1672	0.056033333

700	0.0004	0.0002	0.1458	0.0488
750	0.0002	0.0001	0.1272	0.0425
800	0.0001	0	0.111	0.037033333
850	0	0	0.0968	0.032266667
900	0	0	0.0845	0.028166667
950	0	0	0.0737	0.024566667
1000	0	0	0.0643	0.021433333
1050	0	0	0.057	0.019
1100	0	0	0.0518	0.017266667
1150	0	0	0.048	0.016
1200	0	0	0.0452	0.015066667
1250	0	0	0.0431	0.014366667
1500	0	0	0.0379	0.012633333
1750	0	0	0.0362	0.012066667
2000	0	0	0.0355	0.011833333
2500	0	0	0.0347	0.011566667
3000	0	0	0.0342	0.0114
3500	0	0	0.0339	0.0113
4000	0	0	0.0337	0.011233333
4500	0	0	0.0336	0.0112
5000	0	0	0.0334	0.011133333
5500	0	0	0.0333	0.0111
6000	0	0	0.0333	0.0111
6500	0	0	0.0332	0.011066667
7000	0	0	0.0331	0.011033333
7500	0	0	0.0331	0.011033333
8000	0	0	0.033	0.011

Table B.7 Radiation fog uplink data.

Table B.8 shows the data obtained for the FSO downlink in the presence of radiation fog with a UAV altitude of 4 *km*.

Altitude	0.85 micron	1.55 micron	10 micron	Equal gain diversity
3800	0.9967	0.9991	0.9974	0.9977
3600	0.9931	0.9981	0.9946	0.9953
3400	0.9891	0.997	0.9914	0.9925
3200	0.9845	0.9958	0.9878	0.9894
3000	0.9795	0.9944	0.9837	0.9859
2800	0.9728	0.991	0.9788	0.9809
2600	0.9637	0.9841	0.9726	0.9735
2400	0.9522	0.9736	0.9649	0.9636
2200	0.9384	0.9597	0.9559	0.9513
2000	0.9223	0.9425	0.9453	0.9367
1800	0.8942	0.9114	0.9311	0.9122
1600	0.825	0.8346	0.9057	0.8551
1400	0.668	0.6622	0.8537	0.7280
1200	0.3839	0.3608	0.7418	0.4955
1000	0.0896	0.073	0.5212	0.2279
800	0.0093	0.006	0.3022	0.1058
600	0.001	0.0005	0.175	0.0588
400	0.0001	0	0.1012	0.0338
200	0	0	0.0584	0.0195
0	0	0	0.0337	0.0112

Table B.8 Radiation fog downlink data with a 4 *km* UAV altitude.

Table B.9 shows the corresponding data for an 8 *km* UAV altitude and an FSO downlink in the presence of radiation fog.

Altitude	0.85 micron	1.55 micron	10 micron	Equal gain diversity
7500	0.9979	0.9995	0.9984	0.9986
7000	0.9953	0.9989	0.9966	0.9969
6500	0.9923	0.9981	0.9946	0.9950
6000	0.9889	0.9973	0.9925	0.9929
5500	0.9852	0.9964	0.99	0.9905
5000	0.9812	0.9954	0.9869	0.9878
4500	0.9764	0.9941	0.9831	0.9845
4000	0.97	0.9924	0.978	0.9801

3500	0.9614	0.99	0.9713	0.9742
3000	0.95	0.9868	0.9623	0.9664
2500	0.9295	0.9718	0.948	0.9498
2000	0.8946	0.9353	0.9251	0.9183
1500	0.7381	0.7581	0.8658	0.7873
1400	0.6478	0.657	0.8356	0.7135
1300	0.5243	0.521	0.7911	0.6121
1200	0.3722	0.3576	0.7261	0.4853
1100	0.2135	0.1943	0.6338	0.3472
1000	0.0868	0.0723	0.5102	0.2231
900	0.0279	0.0208	0.3885	0.1457
800	0.009	0.006	0.2957	0.1036
700	0.0029	0.0017	0.225	0.0765
600	0.0009	0.0005	0.1712	0.0575
500	0.0003	0	0.1302	0.0435
400	0	0	0.099	0.0330
300	0	0	0.0752	0.0251
200	0	0	0.0571	0.0190
100	0	0	0.0434	0.0145
0	0	0	0.0329	0.0110

Table B.9 Radiation fog downlink data with an 8 *km* UAV altitude.

Table B.10 shows received power in dBm for the FSO uplink with no weather phenomena present in the atmosphere.

Altitude	0.85 micron	1.55 micron	10 micron	Equal gain diversity	Receiver Threshold
500	12.757	12.906	12.761	12.809	-11.32
1000	12.556	12.824	12.572	12.652	-11.32
1500	12.395	12.758	12.429	12.530	-11.32
2000	12.268	12.706	12.319	12.436	-11.32
2500	12.171	12.668	12.239	12.365	-11.32
3000	12.095	12.643	12.185	12.314	-11.32
3500	12.043	12.629	12.148	12.281	-11.32
4000	12.005	12.619	12.122	12.257	-11.32

4500	11.989	12.611	12.102	12.243	-11.32
5000	11.955	12.606	12.087	12.225	-11.32
5500	11.937	12.602	12.074	12.214	-11.32
6000	11.921	12.597	12.064	12.204	-11.32
6500	11.906	12.594	12.055	12.195	-11.32
7000	11.893	12.591	12.048	12.187	-11.32
7500	11.881	12.588	12.040	12.180	-11.32
8000	11.872	12.586	12.034	12.175	-11.32

Table B.10 Received power for ground-to-air uplink.

Table B.11 shows received power in dBm for the FSO downlink with no weather phenomena present in the atmosphere for a UAV altitude of 8 *km*.

Altitude	0.85 micron	1.55 micron	10 micron	Equal gain diversity	Receiver Threshold
7500	13.001	13.008	13.003	13.004	-11.32
7000	12.990	13.006	12.996	12.997	-11.32
6500	12.977	13.002	12.987	12.989	-11.32
6000	12.962	12.999	12.978	12.979	-11.32
5500	12.946	12.995	12.967	12.969	-11.32
5000	12.928	12.990	12.953	12.957	-11.32
4500	12.907	12.985	12.936	12.943	-11.32
4000	12.878	12.977	12.914	12.923	-11.32
3500	12.839	12.967	12.884	12.897	-11.32
3000	12.788	12.953	12.843	12.862	-11.32
2500	12.715	12.929	12.785	12.810	-11.32
2000	12.614	12.890	12.701	12.736	-11.32
1500	12.486	12.838	12.588	12.640	-11.32
1000	12.326	12.772	12.445	12.519	-11.32
500	12.124	12.690	12.263	12.366	-11.32
0	11.871	12.585	12.033	12.174	-11.32

Table B.11 Received power for air-to-ground downlink with 8 *km* UAV altitude.

Table B.12 shows received power in dBm for the FSO uplink with cumulus clouds present in the atmosphere.

Altitude	0.85 micron	1.55 micron	10 micron	Equal gain diversity	Receiver Threshold
50	12.982	12.999	12.982	12.988	-11.32
100	12.955	12.988	12.954	12.966	-11.32
150	12.928	12.976	12.928	12.944	-11.32
200	12.902	12.966	12.902	12.923	-11.32
250	12.876	12.955	12.877	12.903	-11.32
300	12.851	12.945	12.853	12.883	-11.32
350	12.729	12.834	12.724	12.762	-11.32
400	11.600	11.690	11.514	11.602	-11.32
425	10.575	10.645	10.415	10.546	-11.32
450	9.244	9.284	8.986	9.173	-11.32
475	7.606	7.609	7.228	7.484	-11.32
500	5.661	5.618	5.140	5.479	-11.32
525	3.408	3.312	2.718	3.157	-11.32
550	0.849	0.689	-0.026	0.521	-11.32
575	-2.020	-2.248	-3.116	-2.436	-11.32
600	-5.200	-5.498	-6.498	-5.697	-11.32
625	-8.665	-9.066	-10.269	-9.281	-11.32
650	-12.518	-13.010	-14.437	-13.248	-11.32
675	-16.576	-16.990	-18.539	-17.289	-11.32
700	-20.969	-20.969	-23.979	-21.761	-11.32
725	-26.990	-26.990	-26.990	-26.990	-11.32

Table B.12 Received power for ground-to-air uplink with cumulus clouds.

Table B.12 shows the received power for a ground-to-air uplink in the presence of altostratus clouds.

Altitude	0.85 micron	1.55 micron	10 micron	Equal gain diversity	Receiver Threshold
200	12.902	12.966	12.902	12.923	-11.32
400	12.804	12.925	12.806	12.845	-11.32
600	12.713	12.888	12.719	12.774	-11.32
800	12.631	12.854	12.642	12.710	-11.32
1000	12.556	12.824	12.572	12.652	-11.32
1200	12.510	12.795	12.488	12.600	-11.32
1400	12.425	12.770	12.455	12.553	-11.32
1600	12.368	12.747	12.404	12.510	-11.32
1800	12.316	12.725	12.360	12.471	-11.32
2000	12.268	12.706	12.319	12.436	-11.32
2025	11.935	12.364	12.078	12.130	-11.32
2050	10.950	11.343	11.367	11.224	-11.32
2075	9.309	9.644	10.182	9.727	-11.32
2100	7.017	7.264	8.527	7.655	-11.32
2125	4.069	4.206	6.399	5.029	-11.32
2150	0.469	0.469	3.802	1.883	-11.32
2175	-3.788	-3.958	0.734	-1.752	-11.32
2200	-8.665	-9.066	-2.807	-5.828	-11.32
2225	-14.202	-14.949	-6.819	-10.331	-11.32
2250	-20.969	-20.969	-11.308	-15.229	-11.32
2275	-26.990	-26.990	-16.198	-20.300	-11.32
2300	-35.229	-35.229	-22.218	-26.576	-11.32

Table B.13 Received power for ground-to-air uplink with altostratus clouds.

Table B.14 shows the received power data for the ground-to-air uplink with advection

fog present in the atmosphere.

Altitude	0.85 micron	1.55 micron	10 micron	Equal gain diversity	Receiver Threshold
20	10.589	10.539	10.064	10.404	-11.32
40	8.168	8.069	7.116	7.809	-11.32
60	5.745	5.597	4.170	5.226	-11.32
80	3.324	3.126	1.225	2.656	-11.32
100	0.906	0.652	-1.726	0.095	-11.32
120	-1.524	-1.818	-4.660	-2.457	-11.32
140	-3.936	-4.295	-7.595	-4.994	-11.32
160	-6.345	-6.778	-10.555	-7.528	-11.32
180	-8.794	-9.208	-13.565	-10.058	-11.32
200	-11.192	-11.675	-16.576	-12.570	-11.32
220	-13.565	-14.202	-19.208	-15.040	-11.32
240	-16.198	-16.576	-22.218	-17.611	-11.32
260	-18.539	-19.208	-26.990	-20.300	-11.32
280	-20.969	-22.218	-26.990	-22.730	-11.32

Table B.14 Received power for ground-to-air uplink with advection fog.

Table B.15 shows the received power data for the ground-to-air uplink with radiation fog present in the atmosphere.

Altitude	0.85 micron	1.55 micron	10 micron	Equal gain diversity	Receiver Threshold
50	10.547	10.305	12.409	11.193	-11.32
100	8.083	7.600	11.808	9.598	-11.32
150	5.621	4.897	11.208	8.227	-11.32
200	3.156	2.191	10.609	7.056	-11.32
250	0.697	-0.458	10.010	6.056	-11.32
300	-1.765	-3.224	9.413	5.175	-11.32
350	-4.225	-5.918	8.815	4.391	-11.32
400	-6.696	-8.601	8.219	3.672	-11.32
450	-9.136	-11.308	7.622	2.996	-11.32
500	-11.675	-13.979	7.026	2.347	-11.32
550	-13.979	-16.576	6.431	1.720	-11.32
600	-16.576	-19.208	5.837	1.104	-11.32
650	-19.208	-22.218	5.243	0.495	-11.32

700	-20.969	-23.979	4.648	-0.106	-11.32
750	-23.979	-26.990	4.055	-0.706	-11.32
800	-26.990	No Signal	3.464	-1.304	-11.32
850	No Signal	No Signal	2.869	-1.902	-11.32
900	No Signal	No Signal	2.279	-2.492	-11.32
950	No Signal	No Signal	1.685	-3.086	-11.32
1000	No Signal	No Signal	1.092	-3.679	-11.32
1050	No Signal	No Signal	0.569	-4.202	-11.32
1100	No Signal	No Signal	0.154	-4.618	-11.32
1150	No Signal	No Signal	-0.177	-4.949	-11.32
1200	No Signal	No Signal	-0.438	-5.210	-11.32
1250	No Signal	No Signal	-0.645	-5.416	-11.32
1500	No Signal	No Signal	-1.203	-5.975	-11.32
1750	No Signal	No Signal	-1.403	-6.174	-11.32
2000	No Signal	No Signal	-1.487	-6.259	-11.32
2500	No Signal	No Signal	-1.586	-6.358	-11.32
3000	No Signal	No Signal	-1.649	-6.421	-11.32
3500	No Signal	No Signal	-1.688	-6.459	-11.32
4000	No Signal	No Signal	-1.713	-6.485	-11.32
4500	No Signal	No Signal	-1.726	-6.498	-11.32
5000	No Signal	No Signal	-1.752	-6.523	-11.32
5500	No Signal	No Signal	-1.765	-6.536	-11.32
6000	No Signal	No Signal	-1.765	-6.536	-11.32
6500	No Signal	No Signal	-1.778	-6.550	-11.32
7000	No Signal	No Signal	-1.791	-6.563	-11.32
7500	No Signal	No Signal	-1.791	-6.563	-11.32
8000	No Signal	No Signal	-1.805	-6.576	-11.32

Table B.15 Received power for ground-to-air uplink with radiation fog.

Table B.16 shows the received power data for the air-to-ground downlink with radiation fog present in the atmosphere for a UAV altitude of 4 *km*.

Altitude	0.85 micron	1.55 micron	10 micron	Equal gain diversity	Receiver Threshold
3800	12.996	13.006	12.999	13.000	-11.32
3600	12.980	13.002	12.987	12.990	-11.32
3400	12.963	12.997	12.973	12.978	-11.32
3200	12.942	12.992	12.957	12.964	-11.32
3000	12.920	12.986	12.939	12.948	-11.32
2800	12.891	12.971	12.917	12.926	-11.32
2600	12.850	12.941	12.890	12.894	-11.32
2400	12.798	12.894	12.855	12.849	-11.32
2200	12.734	12.832	12.814	12.794	-11.32
2000	12.659	12.753	12.766	12.726	-11.32
1800	12.525	12.607	12.700	12.611	-11.32
1600	12.175	12.225	12.580	12.330	-11.32
1400	11.258	11.220	12.323	11.631	-11.32
1200	8.852	8.583	11.713	9.961	-11.32
1000	2.533	1.644	10.180	6.588	-11.32
800	-7.305	-9.208	7.813	3.257	-11.32
600	-16.990	-20.000	5.441	0.707	-11.32
400	-26.990	No Signal	3.062	-1.705	-11.32
200	No Signal	No Signal	0.674	-4.097	-11.32
0	No Signal	No Signal	-1.713	-6.485	-11.32

Table B.16 Received power for air-to-ground downlink with radiation fog and a UAV

altitude of 4 *km*.

Table B.17 shows shows the received power data for the air-to-ground downlink with radiation fog present in the atmosphere for a UAV altitude of 8 *km*.

Altitude	0.85 micron	1.55 micron	10 micron	Equal gain diversity	Receiver Threshold
7500	13.001	13.008	13.003	13.004216	-11.32
7000	12.990	13.006	12.996	12.996961	-11.32
6500	12.977	13.002	12.987	12.988531	-11.32
6000	12.962	12.999	12.978	12.979355	-11.32
5500	12.946	12.995	12.967	12.968991	-11.32
5000	12.928	12.990	12.953	12.957137	-11.32
4500	12.907	12.985	12.936	12.942604	-11.32
4000	12.878	12.977	12.914	12.923152	-11.32
3500	12.839	12.967	12.884	12.89693	-11.32
3000	12.788	12.953	12.843	12.861719	-11.32
2500	12.693	12.886	12.778	12.786469	-11.32
2000	12.527	12.720	12.672	12.640303	-11.32
1500	11.691	11.808	12.384	11.971886	-11.32
1400	11.125	11.186	12.230	11.544037	-11.32
1300	10.206	10.179	11.993	10.87876	-11.32
1200	8.718	8.544	11.620	9.8704029	-11.32
1100	6.304	5.895	11.030	8.4160971	-11.32
1000	2.395	1.602	10.088	6.4952957	-11.32
900	-2.534	-3.809	8.904	4.6458889	-11.32
800	-7.447	-9.208	7.719	3.1624999	-11.32
700	-12.366	-14.685	6.532	1.8488062	-11.32
600	-17.447	-20.000	5.345	0.6094953	-11.32
500	-22.218	No Signal	4.156	-0.604807	-11.32
400	No Signal	No Signal	2.967	-1.804561	-11.32
300	No Signal	No Signal	1.772	-2.998734	-11.32
200	No Signal	No Signal	0.577	-4.194552	-11.32
100	No Signal	No Signal	-0.615	-5.386015	-11.32
0	No Signal	No Signal	-1.818	-6.588954	-11.32

Table B.17 Received power for air-to-ground downlink with radiation fog and a UAV

altitude of 8 *km*.